Journal of Pharmaceutical Analysis

EDITORIAL BOARD

Xi'an Jiaotong University;
76 Yanta West Road, Xi'an, 710061, China;
Tel.: +86-29-82655433, +86-29-82655412;
E-mail: jpa2011@126.com; jpasubmit@126.com; jpa2011@xjtu.edu.cn

Journal of Pharmaceutical Analysis 8 (2018) 147–152

Contents lists available at ScienceDirect

Journal of Pharmaceutical Analysis

journal homepage: www.elsevier.com/locate/jpa
www.sciencedirect.com

Review Paper

Overview of the detection methods for equilibrium dissociation constant K_D of drug-receptor interaction

Weina Ma, Liu Yang, Langchong He *

School of Pharmacy, Xi'an Jiaotong University Health Science Center, No. 76, Yanta West Street, Xi'an, Shaanxi Province 710061, PR China

ARTICLE INFO

Article history:
Received 3 February 2018
Received in revised form
25 April 2018
Accepted 4 May 2018
Available online 5 May 2018

Keywords:
Equilibrium dissociation constant
Drug-receptor interaction
RBA
SPR
FRET
Affinity chromatography

ABSTRACT

Drug-receptor interaction plays an important role in a series of biological effects, such as cell proliferation, immune response, tumor metastasis, and drug delivery. Therefore, the research on drug-receptor interaction is growing rapidly. The equilibrium dissociation constant (K_D) is the basic parameter to evaluate the binding property of the drug-receptor. Thus, a variety of analytical methods have been established to determine the K_D values, including radioligand binding assay, surface plasmon resonance method, fluorescence energy resonance transfer method, affinity chromatography, and isothermal titration calorimetry. With the invention and innovation of new technology and analysis method, there is a deep exploration and comprehension about drug-receptor interaction. This review discusses the different methods of determining the K_D values, and analyzes the applicability and the characteristic of each analytical method. Conclusively, the aim is to provide the guidance for researchers to utilize the most appropriate analytical tool to determine the K_D values.

Contents

1. Introduction

The type of drug target is divided into receptor, enzyme, nucleic acid, and so on. There are about 40% drugs which interact with the corresponding receptors in order to exert their pharmacological effects. When the ligands (first messenger) combine with the corresponding receptor, a signal cascade reaction occurs through the second messenger in the cell, resulting in a series of biological effects, such as immune response and cell proliferation [1–3]. Therefore, it is very necessary to study the interaction between drugs and receptors, which contributes to understanding the mechanisms of drugs [4–8]. The equilibrium dissociation constant (K_D) is the basic parameter to evaluate the binding properties of the drug-receptor [9–11]. Thus, it is of great importance to determine the K_D values of the drugs.

A variety of analytical methods have been established to determine the K_D values since the 1960s, including radioligand binding assay (RBA) [12], surface plasmon resonance (SPR) [13], fluorescence energy resonance transfer method (FRET) [14], affinity chromatography [15], and isothermal titration calorimetry (ITC) [16].

Peer review under responsibility of Xi'an Jiaotong University.
* Corresponding author.
E-mail address: helc@mail.xjtu.edu.cn (L. He).

https://doi.org/10.1016/j.jpha.2018.05.001

The main purpose of this review is to analyze the applicability and characteristic of each analytical method in order to provide the guidance for researchers to choose an appropriate analytical tool to study the ligand-receptor interaction.

2. Radioligand binding assay

In the early 1960s, radiolabelled nuclide was used in the receptor pharmacology study. Based on occupation theory [17], RBA method was established. RBA is based on the interaction between radiolabeled ligand and receptor. RBA can be used to study the interaction between receptor and hormones, neurotransmitters, growth factors and drugs, as well as the interaction between the receptor and the second messenger [18].

As shown in Table 1, RBA can be used to determine the affinity constant, dissociation constant and the number of binding receptors [19–34]. The key condition of receptor binding experiments is to prepare an excellent radioligand. The basic requirements of radioligand are high radioactivity, high affinity, high specificity and stability [22,35,36]. The ability to prepare novel and selective radioligands facilitates the study of drug-receptor interaction, and RBA provides an effective tool for studying the mechanisms of drugs at molecular level [37,38]. A variety of receptor materials can be used in the RBA method, such as the cell membrane obtained from cell and tissue [19–28], intact cells [29,30], tissue slice [31–34], and engineered protein samples [38,39].

RBA method provides a sensitive detection method for determining K_D values and promotes the study of receptor pharmacology [37,38]. However, it is not very easy to synthesize the specific radioligands which are the essential elements for RBA method, and radioactive contamination should be prevented during the experiment. So the application of RBA method is greatly limited.

3. Surface plasmon resonance technique

SPR technique, which has been rapidly developed in recent years, is a sensitive and specific technique for the analysis of biomolecular interactions [40]. SPR is based on the principle that the incident light can resonate with the plasma on the metal surface during the total reflection. SPR is utilized to detect whether biological molecules interact with each other, and further explore the specificity of the interaction, kinetic parameters and affinity of the interaction [41–43]. SPR technique provides a powerful and nondestructive tool for cell sorting, cell surface characterization, protein-protein interaction, protein-small molecule interaction, and drug discovery [41,43–45].

SPR is a label-free and real-time detection method for monitoring biomolecular interactions [40]. In recent years, SPR has become a rapid developmental technology for studying the interaction between membrane protein receptors and ligands [44–56], which is shown in Table 2. Because of the high-throughput screening characteristic, SPR has been widely used in the identification of drug targets and the optimization of lead compounds [44–48].

4. Affinity chromatography

In the affinity chromatography, biological macromolecules bind in the carrier surface through chemical reaction. Affinity chromatography utilizes the liquid chromatography method to study the interaction between drugs and biological macromolecules [57–59]. As shown in Table 3, affinity chromatography is widely used in biochemistry, molecular biology, and genomics. It is becoming a commonly used method in the interaction of drug and biological macromolecules [60,61].

The frontal analysis and zonal elution method are utilized to determine the K_D values. Wainer and Hage group have done a lot of work to characterize the affinity of drugs with biomolecules [62–65]. The frontal analysis is mainly conducted by adding the analytes into the mobile phase without injection. Each drug solution with different concentrations is continuously applied to the column until a breakthrough curve with a level plateau is produced. The K_D values can be determined by analyzing the series of breakthrough curves [62,66–68]. Zonal elution method is performed by using a site-specific maker in the mobile phase and injecting the analytes. The K_D values of the analytes at a specific site are calculated by investigating the capacity factor of the analytes with the increasing concentration of the marker in the mobile phase [69,70].

Cell membrane chromatography (CMC) is a kind of bionic affinity chromatography, in which the membrane receptors are prepared as cell membrane stationary phase (CMSP), and is used in determining the interaction between drug and membrane receptors [71–74]. With the development of molecular biology, it is

Table 1
The RBA method and application examples.

No.	Receptor	Drug	Receptor material	K_D values	References
1	Glycine transporter-1	CHIBA-3007	Rat brain membranes	$1.61 (\pm 0.16) \times 10^{-9}$ M	[19]
2	α7 nicotinic acetylcholine receptors	CHIBA-1006	Rat brain membranes	$88.2 (\pm 21.4) \times 10^{-9}$ M	[20]
3	Opioid receptor	TICP[psi]	Rat brain membranes	0.35×10^{-9} M	[21]
4	5-HT(1A) receptors	WAY100635	Rat hippocampal membranes	$87 (\pm 4) \times 10^{-12}$ M	[22]
5	Dopamine D1 receptor	SCH23390	Sheep brain striatum membranes	$56 (\pm 8) \times 10^{-9}$ M	[23]
6	Histamine H3 receptor	Thioperamide	Rat cerebral cortex	$0.80 (\pm 0.06) \times 10^{-9}$ M	[24]
7	Adenosine A2A receptors	ZM241385	Rat striatum membranes Transfected CHO cell membranes	0.14×10^{-9} M 0.23×10^{-9} M	[25]
8	Platelet-activating factor (PAF) receptor	L-659,989	Rabbit platelet membranes	$1.60 (\pm 0.20) \times 10^{-9}$ M	[26]
9	Bradykinin B2 receptors	PIP HOE 140	Guinea pig ileal membranes	15×10^{-12} M	[27]
10	Thromboxane (TP-) receptor	GR32191	Human platelets membranes Human platelets	2.1×10^{-9} M 2.2×10^{-9} M	[28]
11	Human angiotensin II AT1 receptor	Olmesartan Telmisartan	CHO-hAT(1) cells	0.091×10^{-9} M 0.12×10^{-9} M	[29]
12	Glucocorticoid receptor	Dexamethasone	Peripheral blood mononuclear cells	66.194×10^{-9} M	[30]
13	Histamine H1-receptors	Mepyramine	Bovine retinal blood vessels	$2.78 (\pm 0.32) \times 10^{-9}$ M	[31]
14	Calcium channels	Nitrendipine	Rat brain synaptosomes	0.35×10^{-9} M	[32]
15	NK1 receptor	CP96,345	Guinea pig lung	$0.12 (\pm 0.03) \times 10^{-9}$ M	[33]
16	vasopressin V2-receptors	DDAVP	Rat kidney	0.76×10^{-9} M	[34]

Table 2
The SPR method and application examples.

No.	Receptor	Drug	Receptor material	K_D values	References
1	EGFR	EGF	EGFR protein	0.177×10^{-6} M	[44]
		GE11		0.459×10^{-3} M	
		mAb LA1		2.07×10^{-9} M	
2	Subendothelial collagens	vWf	Purified protein	$2.03(\pm 0.04) \times 10^{-9}$ M	[45]
3	Pr55(Gag)	1,4,5-IP3	Purified protein	2170×10^{-6} M	[46]
		di-C(8)-PI		186×10^{-6} M	
		di-C(8)-PI(4,5)P2		47.4×10^{-6} M	
4	VEGFR2 D3	Nanobody against NTV(1–4)	HUVEC cell	$49(\pm 1.8) \times 10^{-9}$ M	[47]
5	CD56	Monoclonal antibodies m900	Cancer cell	2.9×10^{-9} M	[48]
		Monoclonal antibodies m906		4.5×10^{-9} M	
6	Grp1 PH domain	Biotinylated Ins(1,3,4,5)P4	Rat brain membranes	0.14×10^{-6} M	[49]
7	Angiotensin converting enzyme	Lisinopril	Angiotensin converting enzyme	1.78×10^{-9} M	[50]
8	rKDR1–3	VEGF165	rKDR1–3 protein	57.4×10^{-9} M	[51]
9	Lipoprotein lipase	Bis-ANS	Purified protein	$(0.10 - 0.26) \times 10^{-6}$ M	[52]
10	CL-43	Yeast mannan	Purified protein	$(2.68 - 2.72) \times 10^{-8}$ M	[53]
11	Human glycophorin A	Nanobody IH4	Human glycophorin A	33×10^{-9} M	[54]
12	Cyclophilin A	Trp-Gly-Pro	Cyclophilin A	3.41×10^{-6} M	[55]
13	Collagen glycoprotein VI	GABA	Human platelets	41.4×10^{-9} M	[56]

Table 3
The affinity chromatography method and application examples.

No.	Receptor	Drug	Receptor material	K_D values	References
1	Estrogen receptor	Diethylstilbestrol	Purified protein	ERRγ, 237×10^{-9} M	[62]
				ERRα, 929×10^{-9} M	
2	α3β4nicotinic acetylcholine receptor	Dextromethorphan	α3β4-nAChR cell membrane	K_a:$23.40(\pm 0.36) \times 10^6$ M^{-1}	[63]
		Levomethorphan		K_a:$12.01(\pm 0.23) \times 10^6$ M^{-1}	
3	Cannabinoid receptor CB1	Win-55, MA, ACEA	KU-812 cell membrane	$(8.6 \pm 8.3) \times 10^{-9}$ M, $(19.8 \pm 10.9) \times 10^{-9}$ M, $(0.74 \pm 0.22) \times 10^{-9}$ M	[64]
	Cannabinoid receptor CB2			$(0.37 \pm 0.12) \times 10^{-9}$ M, $(653 \pm 182) \times 10^{-9}$ M, $(5200 \pm 2.5) \times 10^{-9}$ M	
4	PKCα	Chelerythrine	Purified protein	698×10^{-9} M	[66]
5	μ opioid receptors	Naloxone	CHO-μ opioid receptors cell membrane	110×10^{-9} M	[67]
	κ opioid receptors	U69593	CHO-κ opioid receptors cell membrane	84×10^{-9} M	
6	L-type calcium channel	Nifedipine	VSMC	$(3.36 \pm 0.28) \times 10^{-6}$ M	[72]
		Nimodipine		$(1.34 \pm 0.15) \times 10^{-6}$ M	
		Nitrendipine		$(6.83 \pm 0.48) \times 10^{-7}$ M	
		Nicardipine		$(1.23 \pm 0.16) \times 10^{-7}$ M	
		Amlodipine		$(1.09 \pm 0.09) \times 10^{-7}$ M	
		Verapamil		$(8.51 \pm 0.61) \times 10^{-8}$ M	
7	α_{1A} adrenoreceptor	Tamsulosin	α_{1A}/HEK293 cell membrane	$(1.87 \pm 0.13) \times 10^{-6}$ M	[74]
		5-methylurapidil		$(2.86 \pm 0.20) \times 10^{-6}$ M	
		Doxazosin		$(3.01 \pm 0.19) \times 10^{-6}$ M	
		Terazosin		$(3.44 \pm 0.19) \times 10^{-6}$ M	
		Alfuzosin		$(3.50 \pm 0.21) \times 10^{-6}$ M	
8	Histamine H_1 receptor	Azelastine	H_1R/HEK293 cell membrane	$(8.72 \pm 0.21) \times 10^{-7}$ M	[75]
		Cyproheptadine		$(9.12 \pm 0.26) \times 10^{-7}$ M	
		Doxipine		$(9.90 \pm 0.18) \times 10^{-7}$ M	
		Astemizole		$(1.42 \pm 0.13) \times 10^{-6}$ M	
		Chlorpheniramine		$(2.25 \pm 0.36) \times 10^{-6}$ M	
		Diphenhydramine		$(3.10 \pm 0.27) \times 10^{-6}$ M	

possible to construct cell lines with high expression of specific receptors, which makes the CMC method have stronger specificity and selectivity. Based on the development of CMC, a variety of CMC models such as L-type calcium channel, α_{1A} adrenergic receptor, histamine H_1 receptor and vascular endothelial growth factor receptor models are established in order to determine the K_D values [75–78].

Affinity chromatography plays a very important role in the study of drug-receptor interaction. The methods of binding receptor to the carrier surface are divided into chemical bonding and physical adsorption. However, after the immobilization of biological macromolecules via chemical bonding, their original configurations and even functions are largely "lost". While physical adsorption can largely retain the three-dimensional configurations and biological activities of membrane receptors and can accurately reveal the drug-membrane receptor interaction process in vivo.

5. Fluorescence energy resonance transfer method

Fluorescence spectroscopy is the most popular technique in the field of biology and medicine, which leads people to the microcosmic world of bio-medicine. The theoretical basis for FRET is a nonradiative energy transfer between two fluorescent molecules (D and A, whose excitation spectra are partially overlapped) that are located close to each other (less than 10 nm) [79–81]. FRET can

be used to study receptor-ligand interactions, affinity constants, receptor dimerization, and so on [82–84].

FRET has been widely used in drug-receptor affinity studies under equilibrium condition with no need to separate the free and combinative ligands [85–87]. Piehler group studied the interaction of IFNR2 with Ifnar1-H10 and measured its K_D value to be 5 μM by FRET technique [88]. Domanov et al. [89] also used the FRET technique to study the interaction between cytochrome c and bilayer phospholipid membranes and found a K_D value of 0.2–0.4 μM.

FRET has the following advantages compared with other methods. The first is high sensitivity, and it is now possible to study single receptor molecules in this way. Moreover, FRET can selectively study intermolecular interactions under physiological conditions (living cell states) [90,91]. Another advantage is that a variety of fluorescent probes can be obtained commercially. The fluorescent probes can be used to label molecules with no fluorescence properties, thus greatly broadening the research approach. Combined with its high spatial resolution, FRET becomes an excellent tool for studying receptor-ligand interactions [92,93].

6. Isothermal titration calorimetry

ITC is a technique based on the reaction heat to quantify the interactions of various biomolecules. As a kind of rapid and direct tool without markers, ITC can detect any heat changes of biochemical reaction process. ITC is widely used in molecular biology research, drug design and structure optimization, and drug mechanism studies [94,95].

Micro calorimeter with high sensitivity and high automation is used to monitor and record the calorimetric curve of the reaction process continuously and accurately. ITC, an in situ, on-line and non-destructive method, provides the thermodynamic and kinetic information (eg, binding constant (K_D), reaction stoichiometry (n), enthalpy (ΔH) and entropy (ΔS) [96,97]. ITC can be also used to study the properties of drug-receptor interaction by directly detecting the heat changes during the process of biochemical reaction [98,99].

By means of the ITC method, Li et al. [16] studied the interaction of neomycin and tobramycin with MLL protein, and found that the K_D values are18.8 for neomycin and 59.9 μM for tobramycin, respectively. Daddaoua group found that only 2-ketoglutarate could act on PtxS with an affinity constant K_D of 15 μM from glucose, ketoglucose and 2-ketoglucose by ITC technology [100].

Without any modification of receptors and ligands, ITC can directly determine the affinity of the drug-receptor under natural conditions [101]. ITC can not only determine the binding affinity, but also clarify the potential mechanism of molecular interactions. ITC is able to confirm the expected binding targets in the drug discovery process, deeply understand the structure-function relationship, and provide the guidance for candidate compounds selection and lead compounds optimization [102,103].

7. Conclusion

In all, the above five methods are all effective analytical tools to study the ligand-receptor interaction. RBA and FRET methods both provide high sensitivity, while both of them need the specific label (radiolabeled ligand for RBA, fluorescent label for FRET), which limits the application of the methods. Affinity chromatography is a nondestructive and dynamical method to study the ligand-receptor interaction, but the sensitivity is limited by the detector of HPLC. As SPR and ITC methods are highly sensitive and nondestructive, they provide powerful tools for studying drug-receptor interaction. Therefore, high sensitive and nondestructive analysis methods play a crucial role in the exploration of ligand-receptor interaction.

Conflicts of interest

The authors declare that there are no conflicts of interest.

References

[1] S. Schmidt, H. Wang, D. Pussak, et al., Probing multivalency in ligand-receptor-mediated adhesion of soft, biomimetic interfaces, Beilstein J. Org. Chem. 11 (2015) 720–729.
[2] X. Men, J. Zhou, J. Tang, et al., Ligand-induced receptor-like kinase complex regulates floral organ abscission in Arabidopsis, Cell Rep. 14 (2016) 1330–1338.
[3] Y. Namkung, C. Le Gouill, V. Lukashova, et al., Monitoring G protein-coupled receptor and β-arrestin trafficking in live cells using enhanced bystander BRET, Nat. Commun. 7 (2016) 12178.
[4] N. Ferruz, G. De Fabritiis, Binding kinetics in drug discovery, Mol. Inf. 35 (2016) 216–226.
[5] M. Vass, A.J. Kooistra, T. Ritschel, et al., Molecular interaction fingerprint approaches for GPCR drug discovery, Curr. Opin. Pharmacol. 30 (2016) 59–68.
[6] L.G. Ferreira, R.N. Dos Santos, G. Oliva, et al., Molecular docking and structure-based drug design strategies, Molecules 20 (2015) 13384–13421.
[7] Y. Fang, Ligand-receptor interaction platforms and their applications for drug discovery, Expert. Opin. Drug Discov. 7 (2012) 969–988.
[8] M.R. Duff Jr, E.E. Howell, Thermodynamics and solvent linkage of macromolecule-ligand interactions, Methods 76 (2015) 51–60.
[9] N.J. Alves, S.D. Stimple, M.W. Handlogten, et al., Small-molecule-based affinity chromatography method for antibody purification via nucleotide binding site targeting, Anal. Chem. 84 (2012) 7721–7728.
[10] Z. Tong, J.E. Schiel, E. Papastavros, et al., Kinetic studies of drug-protein interactions by using peak profiling and high-performance affinity chromatography: examination of multi-site interactions of drugs with human serum albumin columns, J. Chromatogr. A 1218 (2011) 2065–2071.
[11] J.H. Seo, C.S. Kim, H.J. Cha, Structural evaluation of GM1-related carbohydrate-cholera toxin interactions through surface plasmon resonance kinetic analysis, Analyst 138 (2013) 6924–6929.
[12] K.A. Frey, R.L. Albin, Receptor binding techniques, Curr. Protoc. Neurosci. Chapt. 1 (2001) (Unit 1.4).
[13] K. Brännström, A. Öhman, L. Nilsson, et al., The N-terminal region of amyloid β controls the aggregation rate and fibril stability at low pH through a gain of function mechanism, J. Am. Chem. Soc. 136 (2014) 10956–10964.
[14] B.R. Capraro, Z. Shi, T. Wu, et al., Kinetics of endophilin N-BAR domain dimerization and membrane interactions, J. Biol. Chem. 288 (2013) 12533–12543.
[15] H.S. Kim, D.S. Hage, Chromatographic analysis of carbamazepine binding to human serum albumin, J. Chromatogr. B 816 (2005) 57–66.
[16] L. Li, R. Zhou, H. Geng, et al., Discovery of two aminoglycoside antibiotics as inhibitors targeting the menin-mixed lineage leukaemia interface, Bioorg. Med. Chem. Lett. 24 (2014) 2090–2093.
[17] G. Perret, P. Simon, Radioreceptor assay: principles and applications to pharmacology, J. Pharmacol. 15 (1984) 265–286.
[18] D.B. Bylund, M.L. Toews, Radioligand binding methods: practical guide and tips, Am. J. Physiol. 265 (1993) L421–L429.
[19] J. Zhang, J. Wu, J. Toyohara, et al., Pharmacological characterization of [³H] CHIBA-3007 binding to glycine transporter 1 in the rat brain, PLoS One 6 (2011) e21322.
[20] J. Wu, J. Toyohara, Y. Tanibuchi, et al., Pharmacological characterization of [(125)I]CHIBA-1006 binding, a new radioligand for α7 nicotinic acetylcholine receptors, to rat brain membranes, Brain Res. 1360 (2010) 130–137.
[21] I. Szatmári, G. Tóth, I. Kertész, et al., Synthesis and binding characteristics of [^{3}H] H-Tyr-Ticpsi[CH_2-NH] Cha-Phe-OH, a highly specific and stable delta-opioid antagonist, Peptides 20 (1999) 1079–1083.
[22] S. Parkel, A. Rinken, Characteristics of binding of [^{3}H]WAY100635 to rat hippocampal membranes, Neurochem. Res. 31 (2006) 1135–1140.
[23] V. Casadó, C. Ferrada, J. Bonaventura, et al., Useful pharmacological parameters for G-protein-coupled receptor homodimers obtained from competition experiments. agonist-antagonist binding modulation, Biochem. Pharmacol. 78 (2009) 1456–1463.
[24] A. Alves-Rodrigues, R. Leurs, T.S. Wu, et al., [^{3}H]-thioperamide as a radioligand for the histamine H3 receptor in rat cerebral cortex, Br. J. Pharmacol. 118 (1996) 2045–2052.
[25] A. Uustare, A. Vonk, A. Terasmaa, et al., Kinetic and functional properties of [^{3}H]ZM241385, a high affinity antagonist for adenosine A2A receptors, Life Sci. 76 (2005) 1513–1526.
[26] S.B. Hwang, M.H. Lam, A.H. Hsu, Characterization of platelet-activating factor (PAF) receptor by specific binding of [^{3}H]L-659,989, a PAF receptor

antagonist, to rabbit platelet membranes: possible multiple conformational states of a single type of PAF receptors, Mol. Pharmacol. 35 (1989) 48–58.
[27] N.J. Brenner, G.Y. Stonesifer, K.A. Schneck, et al., [125I]PIP HOE 140, a high affinity radioligand for bradykinin B2 receptors, Life Sci. 53 (1993) 1879–1886.
[28] R.A. Armstrong, P.P. Humphrey, P. Lumley, Characteristics of the binding of [3H]-GR32191 to the thromboxane (TP-) receptor of human platelets, Br. J. Pharmacol. 110 (1993) 539–547.
[29] M.T. Le, M.K. Pugsley, G. Vauquelin, et al., Molecular characterisation of the interactions between olmesartan and telmisartan and the human angiotensin II AT1 receptor, Br. J. Pharmacol. 151 (2007) 952–962.
[30] D. Macut, D. Vojnović Milutinović, I. Božić, et al., Age, body mass index, and serum level of DHEA-S can predict glucocorticoid receptor function in women with polycystic ovary syndrome, Endocrine 37 (2010) 129–134.
[31] S. Sawai, H. Fukui, M. Fukuda, et al., [3H]mepyramine binding sites, histamine H1-receptors, in bovine retinal blood vessels, Curr. Eye Res. 10 (1991) 713–718.
[32] T.J. Turner, S.M. Goldin, Calcium channels in rat brain synaptosomes: identification and pharmacological characterization. High affinity blockade by organic Ca^{2+} channel blockers, J. Neurosci. 5 (1985) 841–849.
[33] X.L. Zhang, J.C. Mak, P.J. Barnes, Characterization and autoradiographic mapping of [3H]CP96,345, a nonpeptide selective NK1 receptor antagonist in guinea pig lung, Peptides 16 (1995) 867–872.
[34] A.J. Marchingo, J.M. Abrahams, E.A. Woodcock, et al., Properties of [3H]1-desamino-8-D-arginine vasopressin as a radioligand for vasopressin V2-receptors in rat kidney, Endocrinology 122 (1988) 1328–1336.
[35] J.J. Maguire, R.E. Kuc, A.P. Davenport, Radioligand binding assays and their analysis, Methods Mol. Biol. 897 (2012) 31–77.
[36] K.A. Krohn, The physical chemistry of ligand-receptor binding identifies some limitations to the analysis of receptor images, Nucl. Med. Biol. 28 (2001) 477–483.
[37] G. Tóth, J.R. Mallareddy, Tritiated opioid receptor ligands as radiotracers, Curr. Pharm. Des. 19 (2013) 7461–7472.
[38] A.B. Young, G.E. Fagg, Excitatory amino acid receptors in the brain: membrane binding and receptor autoradiographic approaches, Trends Pharmacol. Sci. 11 (1990) 126–133.
[39] M. Keen, Radioligand-binding methods for membrane preparations and intact cells, Methods Mol. Biol. 83 (1997) 1–24.
[40] H.H. Nguyen, J. Park, S. Kang, et al., Surface plasmon resonance: a versatile technique for biosensor applications, Sensors 15 (2015) 10481–10510.
[41] P.P. Vachali, B. Li, A. Bartschi, et al., Surface plasmon resonance (SPR)-based biosensor technology for the quantitative characterization of protein-carotenoidinteractions, Arch. Biochem. Biophys. 572 (2015) 66–72.
[42] E. Zeidan, C.L. Kepley, C. Sayes, et al., Surface plasmon resonance: a label-free tool for cellular analysis, Nanomedicine 10 (2015) 1833–1846.
[43] S.G. Patching, Surface plasmon resonance spectroscopy for characterisation of membrane protein-ligand interactions and its potential for drug discovery, Biochim. Biophys. Acta 2014 (1838) 43–55.
[44] W.T. Kuo, W.C. Lin, K.C. Chang, et al., Quantitative analysis of ligand-EGFR interactions: a platform for screening targeting molecules, PLoS One 10 (2015) e0116610.
[45] F. Li, J.L. Moake, L.V. McIntire, Characterization of von Willebrand factor interaction with collagens in real time using surface plasmon resonance, Ann. Biomed. Eng. 30 (2002) 1107–1116.
[46] K. Anraku, R. Fukuda, N. Takamune, et al., Highly sensitive analysis of the interaction between HIV-1 Gag and phosphoinositide derivatives based on surface plasmon resonance, Biochemistry 49 (2010) 5109–5116.
[47] L. Ma, K. Gu, C.H. Zhang, et al., Generation and characterization of a human nanobody against VEGFR-2, Acta Pharmacol. Sin. 37 (2016) 857–864.
[48] Y. Feng, Y. Wang, Z. Zhu, et al., Differential killing of CD56-expressing cells by drug-conjugated human antibodies targeting membrane-distal and membrane-proximal non-overlapping epitopes, MAbs 8 (2016) 799–810.
[49] K. Anraku, T. Inoue, K. Sugimoto, et al., Design and synthesis of biotinylated inositol 1,3,4,5-tetrakisphosphate targeting Grp1 pleckstrin homology domain, Bioorg. Med. Chem. 19 (2011) 6833–6841.
[50] Z. Su, L. Chen, Y. Liu, et al., 35 MHz quartz crystal microbalance and surface plasmon resonance studies on the binding of angiotensin converting enzyme with Lisinopril, Biosens. Bioelectron. 26 (2011) 3240–3245.
[51] H. Li, W. Cao, Z. Chen, et al., The antiangiogenic activity of a soluble fragment of the VEGFR extracellular domain, Biomed. Pharmacother. 67 (2013) 599–606.
[52] A. Lookene, L. Zhang, V. Tougu, et al., 1,1′-bis(anilino)-4-,4′-bis(naphtalene)-8,8′-disulfonate acts as an inhibitor of lipoprotein lipase and competes for binding with apolipoprotein CII, J. Biol. Chem. 278 (2003) 37183–37194.
[53] U. Holmskov, P.B. Fischer, A. Rothmann, et al., Affinity and kinetic analysis of the bovine plasma C-type lectin collectin-43 (CL-43) interacting with mannan, FEBS Lett. 393 (1996) 314–316.
[54] I. Habib, D. Smolarek, C. Hattab, et al., V(H)H (nanobody) directed against human glycophorin A: a tool for autologous red cell agglutination assays, Anal. Biochem. 438 (2013) 82–89.
[55] X. Pang, M. Zhang, L. Zhou, et al., Discovery of a potent peptidic cyclophilin A inhibitor Trp-Gly-Pro, Eur. J. Med. Chem. 46 (2011) 1701–1705.
[56] K.H. Lin, W.J. Lu, S.H. Wang, et al., Characteristics of endogenous γ-aminobutyric acid (GABA) in human platelets: functional studies of a novel collagen glycoprotein VI inhibitor, J. Mol. Med. 92 (2014) 603–614.
[57] X. Zheng, Z. Li, S. Beeram, et al., Analysis of biomolecular interactions using affinity microcolumns: a review, J. Chromatogr. B 968 (2014) 49–63.
[58] R. Matsuda, Z. Li, X. Zheng, et al., Analysis of multi-site drug-protein interactions by high-performance affinity chromatography: binding by glimepiride to normal or glycated human serum albumin, J. Chromatogr. A 1408 (2015) 133–144.
[59] Y. An, X. Li, H. Sun, et al., Target-directed screening of the bioactive compounds specifically binding to β2 -adrenoceptor in semen brassicae by high-performance affinity chromatography, J. Mol. Recognit. (2015), http://dx.doi.org/10.1002/jmr.2478.
[60] J. Anguizola, K.S. Joseph, O.S. Barnaby, et al., Development of affinity microcolumns for drug-protein binding studies in personalized medicine: interactions of sulfonylurea drugs with in vivo glycated human serum albumin, Anal. Chem. 85 (2013) 4453–4460.
[61] Z. Zeng, M. Hincapie, S.J. Pitteri, et al., A proteomics platform combining depletion, multi-lectin affinity chromatography (M-LAC), and isoelectric focusing to study the breast cancer proteome, Anal. Chem. 83 (2011) 4845–4854.
[62] M. Sanghvi, R. Moaddel, I.W. Wainer, The development and characterization of protein-based stationary phases for studying drug–protein and protein–protein interactions, J. Chromatogr. A 1218 (2011) 8791–8798.
[63] K. Jozwiak, S.C. Hernandez, K.J. Kellar, et al., Enantioselective interactions of dextromethorphan and levomethorphan with the alpha 3 beta 4-nicotinic acetylcholine receptor: comparison of chromatographic and functional data, J. Chromatogr. B Anal. Technol. Biomed. Life Sci. 797 (2003) 373–379.
[64] R. Moaddel, A. Rosenberg, K. Spelman, et al., Development and characterization of immobilized cannabinoid receptor (CB1/CB2) open tubular column for on-line screening, Anal. Biochem. 412 (2011) 85–91.
[65] D.S. Hage, J.A. Anguizola, C. Bi, et al., Pharmaceutical and biomedical applications of affinity chromatography: recent trends and developments, J. Pharm. Biomed. Anal. 69 (2012) 93–105.
[66] J.J. Slon-Usakiewicz, J.R. Dai, W. Ng, et al., Global kinase screening. applications of frontal affinity chromatography coupled to mass spectrometry in drug discovery, Anal. Chem. 77 (2005) 1268–1274.
[67] F. Beigi, I.W. Wainer, Syntheses of immobilized G protein-coupled receptor chromatographic stationary phases: characterization of immobilized í and K opioid receptors, Anal. Chem. 75 (2003) 4480–4485.
[68] E. Calleri, C. Temporini, G. Massolini, Frontal affinity chromatography in characterizing immobilized receptors, J. Pharm. Biomed. Anal. 54 (2011) 911–925.
[69] K.S. Joseph, A.C. Moser, S.B. Basiaga, et al., Evaluation of alternatives to warfarin as probes for Sudlow site I of human serum albumin: characterization by high-performance affinity chromatography, J. Chromatogr. A 1216 (2009) 3492–3500.
[70] D.S. Hage, J.A. Anguizola, A.J. Jackson, et al., Chromatographic analysis of drug interactions in the serum proteome, Anal. Methods 3 (2011) 1449–1460.
[71] X. Chen, Y. Cao, H. Zhang, et al., Comparative normal/failing rat myocardium cell membrane chromatographic analysis system for screening specific components that counteract doxorubicin-induced heart failure from Acontium carmichaeli, Anal. Chem. 86 (2014) 4748–4757.
[72] H. Du, J.Y. He, S.C. Wang, et al., Investigation of calcium antagonist-L-type calcium channel interactions by a vascular smooth muscle cell membrane chromatography method, Anal. Bioanal. Chem. 397 (2010) 1947–1953.
[73] S.C. Wang, M. Sun, Y.M. Zhang, et al., A new A431/cell membrane chromatography and online high performance liquid chromatography/mass spectrometry method for screening epidermal growth factor receptor antagonists from Radix sophorae flavescentis, J. Chromatogr. A 1217 (2010) 5246–5252.
[74] H. Du, J. Ren, S.C. Wang, et al., Cell membrane chromatography competitive binding analysis for characterization of α1A adrenoreceptor binding interactions, Anal. Bioanal. Chem. 400 (2011) 3625–3633.
[75] W.N. Ma, D.D. Zhang, J. Li, et al., Interactions between histamine H1 receptor and its antagonists by using cell membrane chromatography method, J. Pharm. Pharmacol. 67 (2015) 1567–1574.
[76] Y. Wang, B. Yuan, X. Deng, et al., Comparison of alpha1-adrenergic receptor cell-membrane stationary phases prepared from expressed cell line and from rabbit hepatocytes, Anal. Bioanal. Chem. 386 (2006) 2003–2011.
[77] H. Du, S.C. Wang, J. Ren, et al., Revealing multi-binding sites for taspine to VEGFR-2 by cell membrane chromatography zonal elution, J. Chromatogr. B 887–888 (2012) 67–72.
[78] W. Yu, B. Yuan, X. Deng, et al., The preparation of HEK293 alpha1A or HEK293 alpha1B cell membrane stationary phase and the chromatographic affinity study of ligands of alpha1 adrenoceptor, Anal. Biochem. 339 (2005) 198–205.
[79] B. Hochreiter, A.P. Garcia, J.A. Schmid, Fluorescent proteins as genetically encoded FRET biosensors in life sciences, Sensors 15 (2015) 26281–26314.
[80] J.Y. Liao, Y. Song, Y. Liu, A new trend to determine biochemical parameters by quantitative FRET assays, Acta Pharmacol. Sin. 36 (2015) 1408–1415.
[81] E. Hirata, E. Kiyokawa, Future perspective of single-molecule FRET biosensors and intravital FRET microscopy, Biophys. J. 111 (2016) 1103–1111.

[82] S. Ding, A.A. Cargill, S.R. Das, et al., Biosensing with förster resonance energy transfer coupling between fluorophores and nanocarbon allotropes, Sensors 15 (2015) 14766–14787.
[83] K.F. Chou, A.M. Dennis, Förster resonance energy transfer between quantum dot donors and quantum dot acceptors, Sensors 15 (2015) 13288–13325.
[84] M. Stanisavljevic, S. Krizkova, M. Vaculovicova, et al., Quantum dots-fluorescence resonance energy transfer-based nanosensors and their application, Biosens. Bioelectron. 74 (2015) 562–574.
[85] C. De. Los Santos, C.W. Chang, M.A. Mycek, et al., FRAP, FLIM, and FRET: detection and analysis of cellular dynamics on a molecular scale using fluorescence microscopy, Mol. Reprod. Dev. 82 (2015) 587–604.
[86] D. Shrestha, A. Jenei, P. Nagy, et al., Understanding FRET as a research tool for cellular studies, Int. J. Mol. Sci. 16 (2015) 6718–6756.
[87] C.D. Kinz-Thompson, R.L. Gonzalez Jr, smFRET studies of the 'encounter' complexes and subsequent intermediate states that regulate the selectivity of ligand binding, FEBS Lett. 588 (2014) 3526–3538.
[88] S. Lata, M. Gavutis, J. Piehler, Monitoring the dynamics of ligand-receptor complexes on model membranes, J. Am. Chem. Soc. 128 (2006) 6–7.
[89] Y.A. Domanov, J.G. Molotkovsky, G.P. Gorbenko, Coverage-dependent changes of cytochrome c transverse location in phospholipid membranes revealed by FRET, Biochim. Biophys. Acta 2005 (1716) 49–58.
[90] E. Alvarez-Curto, J.D. Pediani, G. Milligan, Applications of fluorescence and bioluminescence resonance energy transfer to drug discovery at G protein coupled receptors, Anal. Bioanal. Chem. 398 (2010) 167–180.
[91] S. Lu, Y. Wang, Fluorescence resonance energy transfer biosensors for cancer detection and evaluation of drug efficacy, Clin. Cancer Res. 16 (2010) 3822–3824.
[92] L. Lecarme, E. Prado, A. De Rache, et al., Interaction of polycationic Ni(II)-salophen complexes with G-quadruplex DNA, Inorg. Chem. 53 (2014) 12519–12531.
[93] R.S. Kasai, A. Kusumi, Single-molecule imaging revealed dynamic GPCR dimerization, Curr. Opin. Cell Biol. 27 (2014) 78–86.
[94] R.J. Falconer, A. Penkova, I. Jelesarov, et al., Survey of the year 2008: applications of isothermal titration calorimetry, J. Mol. Recognit. 23 (2010) 395–413.
[95] W.H. Ward, G.A. Holdgate, Isothermal titration calorimetry in drug discovery, Prog. Med. Chem. 38 (2001) 309–376.
[96] R.J. Falconer, Applications of isothermal titration calorimetry - the research and technical developments from 2011 to 2015, J. Mol. Recognit. 29 (2016) 504–515.
[97] R. Huang, B.L. Lau, Biomolecule-nanoparticle interactions: Elucidation of the thermodynamics by isothermal titration calorimetry, Biochim. Biophys. Acta 2016 (1860) 945–956.
[98] L.D. Hansen, M.K. Transtrum, C. Quinn, et al., Enzyme-catalyzed and binding reaction kinetics determined by titration calorimetry, Biochim. Biophys. Acta 1860 (2016) 957–966.
[99] M. Kabiri, L.D. Unsworth, Application of isothermal titration calorimetry for characterizing thermodynamic parameters of biomolecular interactions: peptide self-assembly and protein adsorption case studies, Biomacromolecules 15 (2014) 3463–3473.
[100] A. Daddaoua, T. Krell, C. Alfonso, et al., Compartmentalized glucose metabolism in Pseudomonas putida is controlled by the PtxS repressor, J. Bacteriol. 192 (2010) 4357–4366.
[101] M.W. Freyer, E.A. Lewis, Isothermal titration calorimetry: experimental design, data analysis, and probing macromolecule/ligand binding and kinetic interactions, Methods Cell Biol. 84 (2008) 79–113.
[102] X. Du, Y. Li, Y.L. Xia, et al., Insights into protein-ligand interactions: mechanisms, models, and methods, Int. J. Mol. Sci. 17 (2016).
[103] P. Draczkowski, D. Matosiuk, K. Jozwiak, Isothermal titration calorimetry in membrane protein research, J. Pharm. Biomed. Anal. 87 (2014) 313–325.

Journal of Pharmaceutical Analysis 8 (2018) 153–159

Contents lists available at ScienceDirect

Journal of Pharmaceutical Analysis

journal homepage: www.elsevier.com/locate/jpa
www.sciencedirect.com

Original Research Article

Quantification and pharmacokinetic study of tumor-targeting agent MHI148-clorgyline amide in mouse plasma using liquid chromatography-electrospray ionization tandem mass spectrometry

Zhijun Wang [a,b], Bogdan Z. Olenyuk [c], Jean Chen Shih [c,*], Jeffrey Wang [a,d,**]

[a] Center for Advancement of Drug Research and Evaluation, College of Pharmacy, Western University of Health Sciences, Pomona, CA 91766, USA
[b] Department of Pharmaceutical Sciences, College of Pharmacy, Marshall B. Ketchum University, Fullerton, CA 92831, USA
[c] Department of Pharmacology and Pharmaceutical Sciences, School of Pharmacy, Department of Cell and Neurobiology, Keck School of Medicine, USC-Taiwan Center for Translational Research, University of Southern California, Los Angeles, CA 90089, USA
[d] Department of Pharmaceutical Sciences, College of Pharmacy, Western University of Health Sciences, Pomona, CA 91766, USA

ARTICLE INFO

Article history:
Received 23 July 2017
Received in revised form
16 October 2017
Accepted 19 October 2017
Available online 20 October 2017

Keywords:
MHI148-clorgyline
HPLC
Mass spectrometry
Pharmacokinetics

ABSTRACT

A high-performance liquid chromatography-electrospray ionization tandem mass spectrometric (HPLC-ESI-MS/MS) method was developed for the quantification of MHI148-clorgyline amide (NMI-amide), a novel tumor-targeting monoamine oxidase A inhibitor, in mouse plasma. The method was validated in terms of sensitivity, precision, accuracy, recovery and stability and then applied to a pharmacokinetic study of NMI-amide in mice following intravenous administration. NMI-amide together with the internal standard (IS), MHI-148, was extracted by protein precipitation using acetonitrile. Multiple reaction monitoring was used for quantification of NMI-amide by detecting *m/z* transition of 491.2–361.9, and 685.3–258.2 for NMI-amide and the IS, respectively. The lower limit of quantification (LLOQ) of the HPLC–MS/MS method for NMI-amide was 0.005 μg/mL and the linear calibration curve was acquired with $R^2 > 0.99$ in the concentration range of 0.005–2 μg/mL. The intra- and inter-day precisions of the assay were assessed by percentage of the coefficient of variations, which was within 9.8% at LLOQ and 14.0% for other quality control samples, whereas the mean accuracy ranged from 86.8% to 113.2%. The samples were stable under storage and experimental conditions. This method was successfully applied to a pharmacokinetic study in mice following intravenous administration of 5 mg/kg NMI-amide.

1. Introduction

Monoamine oxidase A (MAOA) is a mitochondria-bound enzyme that degrades monoamine neurotransmitters such as serotonin, dopamine, norepinephrine, and dietary monoamines [1,2]. Recent studies showed that increased MAOA level is correlated with the prostate cancer progression and poor treatment outcome. Pharmacological inhibition of MAOA reduces the growth of prostate cancer cells in vitro and tumor xenografts in vivo [3–5]. MAOA inhibitors have long been used clinically as anti-depressants; they target either the central nervous system or peripheral tissues where MAOA is present. A tumor cell targeting MAOA inhibitor is highly desirable, as it could achieve better efficacy with less toxicity. A novel tumor-targeting MAOA inhibitor, MAOA-near-infrared (MAOA-NIR) dye conjugate, was synthesized in Shih and Olenyuk laboratories and it showed targeting efficacy in prostate tumor xenograft mouse model following intratumoral and intraperitoneal routes of administration. NIR imaging of the whole body in vivo and individual tumor and normal organs ex vivo showed its localization only in the tumors of the experimental animals. Treated mice showed significant delays in tumor growth and decreases in tumor weight as compared to control mice [6].

Subsequently, an improved version of this molecule was synthesized by combining a tumor-targeting NIR dye MHI-148 (Fig. 1) with a moiety of the MAOA inhibitor clorgyline by an amide bond. The resulting compound, MHI148-clorgyline amide (NMI-amide, Fig. 1), a new near-infrared monoamine oxidase inhibitor, was found to preferentially accumulate in the cancerous lesions and inhibit tumor growth in a human xenograft model [7].

Pharmacokinetic studies are necessary to characterize the plasma concentration profile following drug administration and

Peer review under responsibility of Xi'an Jiaotong University.
* Correspondence to: School of Pharmacy, University of Southern California, Los Angeles, CA 90089, USA.
** Corresponding author at: Department of Pharmaceutical Sciences, College of Pharmacy, Western University of Health Sciences, Pomona, CA 91766, USA.
E-mail addresses: jcshih@usc.edu (J.C. Shih), jwang@westernu.edu (J. Wang).

https://doi.org/10.1016/j.jpha.2017.10.001
2095-1779/

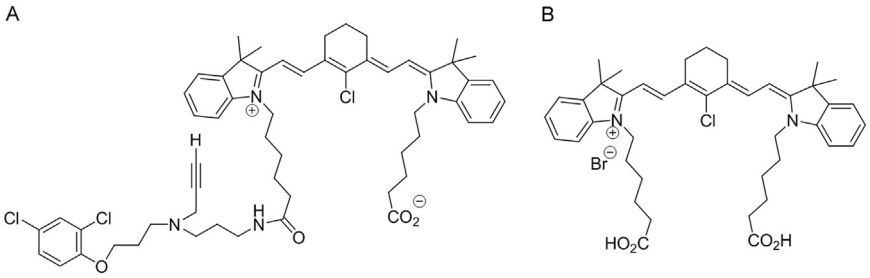

Fig. 1. Chemical structures of (A) NMI-amide and (B) MHI-148 (IS).

this information will be useful for further preclinical and clinical development of this novel anticancer agent. Chromatographic approaches have been most frequently used for quantification of the chemical compounds in plasma samples for pharmacokinetic studies. At present, only radioactive labeled based assay methods have been reported for the assay of clorgyline [8]. MHI-148 has been widely used for cancer detection and the acquisition of real-time pathophysiological information [9]. However, no chromatography based assay methods have been reported for the quantification of clorgyline or MHI-148 in plasma samples. In order to detect NMI-amide in plasma, a UV detector or a fluorescence detector can be potentially used, since NMI-amide has a maximum UV absorbance at 400 nm and a maximum emission wavelength at 808 nm. This is the first report of using mass spectrometry to detect the MHI dye imaging agent and its derivative (NMI-amide) in the plasma samples with high sensitivity and specificity.

Thus, a sensitive and specific high-performance liquid chromatography–mass spectrometric (HPLC–MS/MS) method was developed and validated in terms of accuracy, precision, reproducibility, and recovery. This method was applied to a pharmacokinetic study following intravenous administration of 5 mg/kg NMI-amide in mice.

2. Materials and instrument

2.1. Reagents and chemicals

Formic acid and ammonia acetate were purchased from Sigma-Aldrich (St. Louis, MO, USA). Acetonitrile and methanol were obtained from EMD (Billerica, MA, USA). MHI-148 and NMI-amide were synthesized as described [7,9]. Deionized water was prepared using a Barnstead Nanopure Diamond™ water purification system (APS Water Services Corporation, Van Nuys, CA, USA). C57BL6 mouse plasma was purchased from Innovative Research (Novi, MI, USA). C57B/L mice were purchased from Harlan Laboratories (Placentia, CA, USA). The animal studies were performed in accordance with the Guidelines for the Care and Use of Laboratory Animals with protocols approved by the Institutional Animal Care and Use Committee (IACUC) of University of Southern California (Los Angeles, CA, USA).

2.2. HPLC–MS/MS system

The HPLC–MS/MS system consisted of an API 3200 LC-MS/MS system (Sciex, Framingham, MA, USA) and two Shimadzu LC-20AD Prominence liquid chromatograph pumps equipped with an SIL-20A Prominence autosampler (Shimadzu, Columbia, MD, USA). Chromatography separation was carried out using a Symmetry® C_{18} column (4.6 mm × 75 mm, 3.5 μm; Waters, Milford, MA, USA).

The chromatographic separation was carried out using a mobile phase containing 80% acetonitrile and 20% buffer (0.1% formic acid containing 2 mM ammonium acetate) with a flow rate of 1 mL/min. The entire running time was 2.5 min. The temperatures of analytical column and autosampler were both set at room temperature (24 °C).

All the liquid chromatographic eluent was then introduced into the ESI source in the positive ionization mode. The initial 0.5 min eluent was bypassed from the system to avoid unnecessary contamination from the inorganic salts presented in the plasma samples. The mass spectrometric conditions were as follows: gas 1, nitrogen (40 psi); gas 2, nitrogen (40 psi); ion spray voltage, 4500 V; ion source temperature, 400 °C; curtain gas, nitrogen (25 psi). Multiple reaction monitoring (MRM) scanning mode was used to monitor the transition of *m/z* 491.2–361.9 and *m/z* 685.3–258.2 for NMI-amide and MHI-148, respectively. The MS conditions for NMI-amide and MHI-148 (Internal standard, IS) are shown in Table 1.

2.3. Sample preparation

The stock solution of NMI-amide and MHI-148 were prepared by dissolving appropriate amount of the standards in methanol to generate a concentration of 1 mg/mL. The stock solution of NMI-amide was further diluted appropriately to generate working solutions with concentrations of 0.05, 0.1, 0.2, 0.5, 1, 2, 5, 10, and 20 μg/mL. The stock solution of MHI-148 was diluted to 0.5 μg/mL using 50% methanol as the IS working solution.

The standard calibration samples were prepared by spiking 10 μL of NMI-amide working solutions and 10 μL of IS working solution into 100 μL of mice plasma to obtain the final nominal concentrations of 0.005, 0.01, 0.02, 0.05, 0.1, 0.2, 0.5, 1, and 2 μg/mL. The solution was vortex-mixed and 300 μL acetonitrile was added. The mixture was mixed vigorously for 1 min, followed by centrifuging at 10,000 *g* for 5 min. The supernatant was transferred to a sample vial and 10 μL was injected to the HPLC–MS/MS system for analysis. Of these standards, 0.01, 0.1, and 1 μg/mL were used as low, medium, and high quality control (QC) samples, while the others were used as the standard samples for constructing the standard curve.

Table 1
MS conditions for MHI148-clorgyline amide and MHI-148.

Compounds	Precursor ion (*m/z*)	Product ion (*m/z*)	DP (V)	EP (V)	CEP (V)	CE (V)	CXP (V)
MHI148-clorgyline amide	491.2 $[M+2H]^+$	361.9	45.0	7.0	24.0	27.0	4.0
MHI-148	685.3 $[M+H]^+$	258.2	101.0	7.5	24.0	85.0	4.0

DP, declustering potential; EP, entrance potential; CEP, collision cell entrance potential; CE, collision energy; CXP, collision cell exit potential.

2.4. Method validation

The validity of the assay method was assessed in terms of linearity, sensitivity, precision, accuracy, recovery, dilution integrity and stability. The QC samples at three concentration levels of low, medium and high concentrations (LQC, MQC and HQC, respectively) as well as sample of lower limit of quantification (LLOQ) were utilized and analyzed for method validation [10–12].

2.4.1. Selectivity and specificity

The selectivity of this method was evaluated by injecting the blank plasma sample or spiked with clorgyline (an MAOA inhibitor usually used as antidepressant) and NMI-amide. Clorgyline was detected using MRM by monitoring the *m/z* transition of 272.9–82.1 in positive ion mode.

The highest response product ion from the fragmentation of the precursor ion of NMI-amide (491.2) was used as a quantifier, while the next highest product ion (410.5) was used as a qualifier. Monitoring the signals of *m/z* transition for qualifier ions can confirm the presence of NMI-amide. The quantifier and qualifier signal ratio was determined at LLOQ, LQC, MQC, and HQC levels ($n = 3$). A tolerance of 30% was set for the confirmation as per SANCO/12571/2013 guideline [13].

2.4.2. Linearity and sensitivity

For construction of the standard calibration curve, standard samples were injected in triplicates at concentrations of 0.005, 0.02, 0.05, 0.2, 0.5, and 2 μg/mL. Calibration curve was constructed using the analyte/IS peak area ratio versus the analyte's nominal concentration, and fitted by linear least-squares regression analysis with a weighting factor of $1/x^2$ (x is the value of the nominal concentration).

Sensitivity of the method was evaluated in terms of limit of detection (LOD) and LLOQ. LOD was defined as the concentration of NMI-amide which yields a signal to noise ratio greater than 3. LLOQ was determined based on the two criteria: (1) the analyte response at the LLOQ would be at least 5 times that of the blank; and (2) the analyte peak would be identifiable, discrete, and reproducible with a precision within 20% and accuracy of 80%–120% [10,11].

2.4.3. Precision and accuracy

The intra- and inter-day precisions and accuracy of the method were evaluated using the spiked standard plasma samples at concentrations of LLOQ, 0.01, 0.1 and 1 μg/mL. Precision was calculated as the relative standard deviation (RSD) of the triplicate (inter-day) or five replicates (intra-day) samples, whereas accuracy was assessed as the percentage to the nominal concentration (%). The precision acceptance criteria were set at $<$ 20% for samples at LLOQ concentration, and 15% for other QC samples [10,11].

2.4.4. Recovery

Extraction recovery of NMI-amide and MHI-148 were assessed by comparing the peak areas of the extracted QC samples to the unextracted standard solutions containing equivalent amount of the analytes. Briefly, 300 μL of acetonitrile was added to 100 μL of blank plasma and the mixture was vortex-mixed for 1 min. Afterwards, 10 μL of NMI-amide working solutions was spiked to final concentrations of 0.01 and 1 μg/mL and MHI-148 working solutions were added. The samples were mixed well as post-extracted QC samples. After centrifuging at 10,000 *g* for 5 min, the supernatant was removed and analyzed. The peak area, representing 100% recovery, was compared with that from the extracted QC samples.

2.4.5. Dilution integrity

The plasma concentrations for the first few time points following intravenous administration are usually very high (greater than upper limit of quantification limit, ULOQ) and sample dilution is required. Dilution integrity of NMI-amide in plasma was verified by diluting the samples above ULOQ. In this study, five replicates of plasma samples spiked at concentration of 200 μg/mL underwent 100 and 200-fold dilutions to final concentrations of 2 and 1 μg/mL. The diluted samples were then processed and analyzed using the same procedure mentioned in Section 2.3 ($n = 5$). The precision and accuracy were then determined.

2.4.6. Stability

The stability of NMI-amide in terms of storage stability, freeze/thaw stability, injector stability, and handling stability was evaluated during the sample collection and handling, after long-term and short-term storage, freeze-thaw cycles, and after the entire analysis procedure. For storage stability, the QC samples were prepared and stored at -80 °C for 2 weeks. The samples were then processed and analyzed together with the freshly prepared samples. For freeze–thaw stability assessment, QC samples were exposed to three freeze (-80 °C) and thaw on ice for three cycles and then analyzed along with the freshly prepared samples. For injector stability, the prepared samples in the autosampler were evaluated by re-analyzing the samples after being placed at 4 °C for up to 4 h. For the stability during the handling process, the QC samples were prepared and kept on ice for 4 h and then analyzed along with the freshly prepared samples. All these stability tests were performed on two QC concentrations with triplicate samples. The percent deviation in concentration was used as an indicator of stability. The analyte can be considered stable when the percent deviation was within $\pm$ 15% of the nominal concentration [10,11].

2.5. Application to pharmacokinetic study

The validated assay method was applied to a pharmacokinetic study of NMI-amide in C57B/L mice following intravenous injection at a dose of 5 mg/kg. Five milligrams NMI-amide was precisely weighed and dissolved in DMSO to yield a concentration of 50 mg/mL and further diluted to 5 mg/mL using 50% glycerol:50% ethanol (1:1, v/v). For intravenous injection, approximate 30 μL of NMI-amide solution was injected via tail vein. Mice were euthanized and blood samples were collected via heart puncture at 0, 2, 5, 15, 30, 60 and 90 min post injection. Three mice were used at each point.

Blood samples were placed on ice immediately and centrifuged at 10,000 *g* for 3 min at 4 °C. The supernatant plasma was separated and stored at -80 °C until analysis. The plasma samples were then processed and analyzed by the validated HPLC–MS/MS method as described above. Concentration-time profile was constructed and relevant pharmacokinetic parameters were calculated.

3. Results

3.1. Mass spectrometry and chromatography

The MHI dye imaging agent and its derivative were detected using mass spectrometry. The full Q1 scans of NMI-amide and MHI 148 were acquired in positive ion mode by infusing the standard solutions at concentration of 1 μg/mL into the ESI source. The two proton adduct and one proton adduct were found to be the most

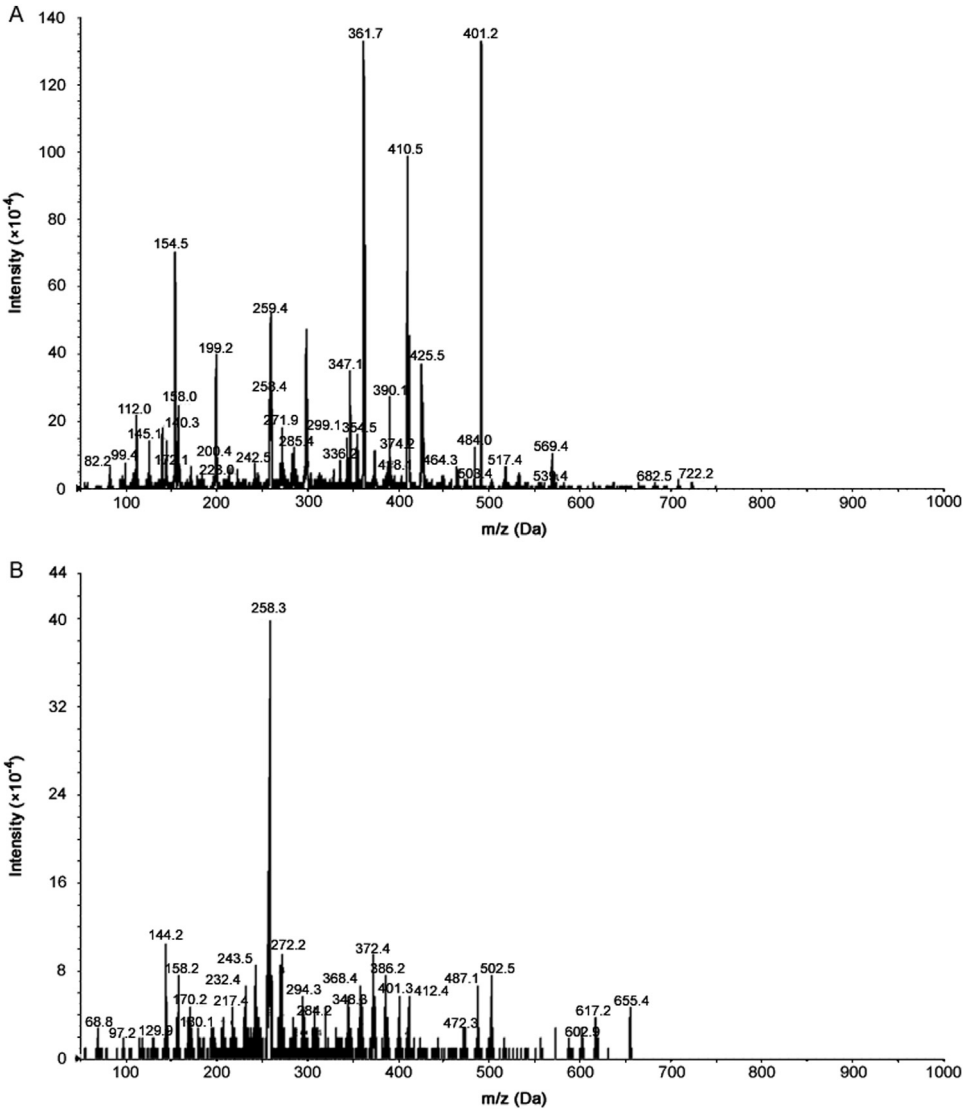

Fig. 2. Product ion mass spectra of (A) NMI-amide and (B) MHI-148 (IS).

intensive ions for NMI-amide (*m/z* 491.2) and MHI-148 (*m/z* 685.3), respectively. The product ion mass spectra of these two compounds are shown in Fig. 2. The most abundant product ion of each analyte was selected from MRM monitoring, and the MS/MS conditions were optimized to maximize the response of each of precursor/product transition (Table 1).

3.2. Method validation

3.2.1. Selectivity and specificity

No obvious peak was detected in blank plasma processed with the procedure in Section 2.3. In addition, in the sample spiked with clorgyline, only clorgyline peak was detected at retention time of 0.75 min (Fig. 3A) while NMI-amide was detected without any interference (Fig. 3B).

The ratios of the qualifier peaks to that of the quantifier peaks were (67.5 ± 9.4)%, (73.1 ± 3.3)%, (72.5 ± 2.0)% and (71.2% ± 1.4)% for LLOQ, LQC, MQC, and HQC, respectively. The RSD values were less than 13.9% (Fig. 4), indicating good specificity.

3.2.2. Linearity and sensitivity

The calibration curve of NMI-amide was linear over the concentration range of 0.005–2 μg/mL with the regression coefficient greater than 0.99, which is acceptable according to the FDA guidelines [10].

The standard curves are expressed as $y = ax + b$, where x is the concentration and y is the ratio of the signal intensity of test compounds over internal standard. The parameters of a and b are the corresponding slop and intercept, respectively. The following relationship was obtained: $y=0.1337x+0.1028$.

The representative MRM chromatograms of the QC sample at concentration of 1 μg/mL, IS (50 ng/mL) and a real plasma sample at 1 h post dose administration (the concentration was calculated to be 0.59 μg/mL) are shown in Figs. 3 C–G. No specific interference was observed surrounding the NMI-amide or IS peak. The LOD and LLOQ were found to be 0.0025 and 0.005 μg/mL, respectively.

3.2.3. Accuracy and precision

The precision and accuracy of the assay method for NMI-amide are summarized in Table 2. For QC samples at concentrations of LLOQ, 0.01, 0.1, and 1 μg/mL, the intra- and inter-day precisions (RSD) ranged from 1.1% to 14.0%. The accuracy, presented as percent deviation from the nominal concentrations, ranged from

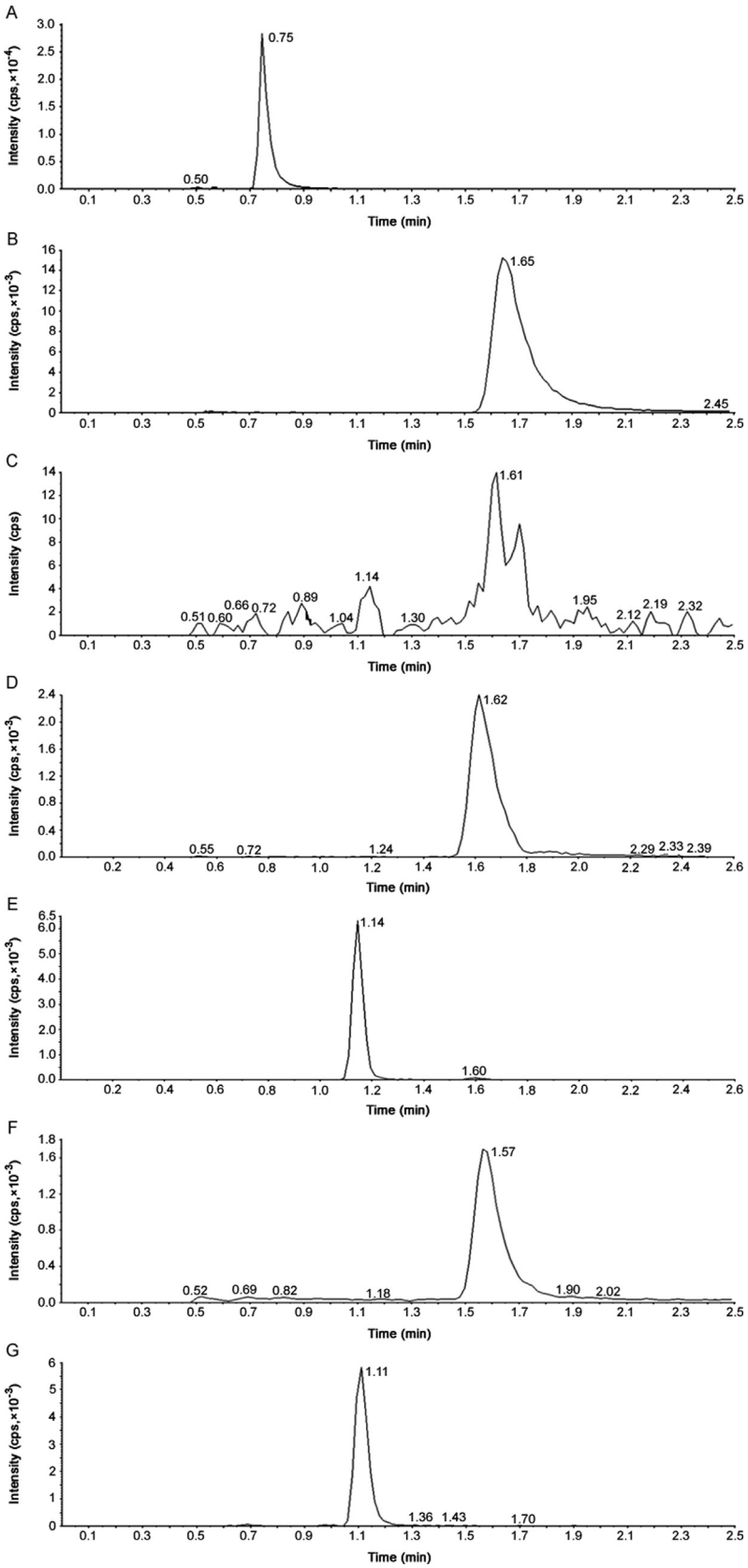

Fig. 3. MRM chromatograms of (A, B) clorgyline and NMI-amide from plasma sample spiked with clorgyline and NMI-amide, respectively; (C) blank plasma, (D) NMI-amide (1 μg/mL), (E) MHI-148, (IS, 50 ng/mL) and (F, G) NMI-amide and IS of a plasma sample of 1 h post dose administration.

86.8% to 113.2%. These results indicated that this method was accurate, precise and reproducible for quantification of NMI-amide in mouse plasma.

3.2.4. Recovery

The protein precipitation extraction method yielded a recovery of 85.4% and 95.9% for NMI-amide at LQC and HQC, respectively,

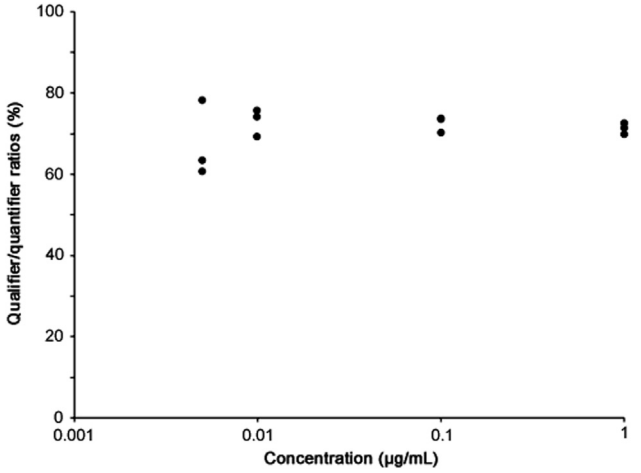

Fig. 4. Qualifier/quantifier peak ratios for samples at LLOQ, LQC, MQC, and HQC levels. (Quantifier: 491.2–361.9; Qualifier: 491.2–410.5).

Table 2
Precision and accuracy for MHI148-clorgyline amide analysis.

Nominal concentration (μg/mL)	Intra-day		Inter-day	
	Accuracy (%)	Precision (%)	Accuracy (%)	Precision (%)
0.005	107.6	9.8	104.4	2.8
0.01	86.8	7.0	99.3	14.0
0.1	104.2	1.1	106.0	11.6
1	113.2	8.6	109.4	6.6

Table 3
Recovery of MHI148-clorgyline amide and MHI-148.

Analyte	Conc. (μg/mL)	Recovery (%)
MHI148-clorgyline amide	0.01	85.4 ± 19.9
	1	95.9 ± 9.1
MHI-148 (IS)	0.05	59.7 ± 10.7

and 59.7% for the IS (MHI-148, Table 3), which suggested that recovery rates were consistent over the calibration ranges. Although the recovery of the IS was relatively low compared to that of NMI-amide, it did not affect the assay precision or accuracy. Thus, no further improvement of its recovery was attempted.

3.2.5. Dilution integrity

The original concentrations of the samples being diluted were back calculated. The accuracy values were 86.4% and 92.8% for 100- and 200-fold dilutions, respectively, while the precision was within 9.9% for both dilutions. The samples of the first three time points (2, 5, and 15 min) underwent dilution before assay.

3.2.6. Stability

NMI-amide was found stable under the storage condition (−80 °C) for at least two weeks and at least 4 h on ice (4 °C). In our preliminary study, NMI-amide was found unstable in plasma at room temperature with a degradation half-life of 11 h and 22 h for low concentration and high concentration, respectively. Thus, all the stock solutions and plasma samples were placed on ice during the entire process. The duration of sample preparation was kept within 4 h. The stability test results showed that NMI-amide was stable under current experiment settings (Table 4).

Table 4
Stability of MHI148-clorgyline amide under different conditions.

Condition	Conc. (μg/mL)	Measured conc. (μg/mL)
Handling stability (4 h on ice)	0.01	0.0099 ± 0.0005
	1	0.94 ± 0.10
Freeze and thaw stability (3 freeze (−80 °C) and thaw (on ice) cycles)	0.01	0.0095 ± 0.0009
	1	0.95 ± 0.03
Injector stability (4 h in the autosampler)	0.01	0.0098 ± 0.0010
	1	1.00 ± 0.09
Storage stability (2 weeks at −80 °C)	0.01	0.010 ± 0.004
	1	1.05 ± 0.06

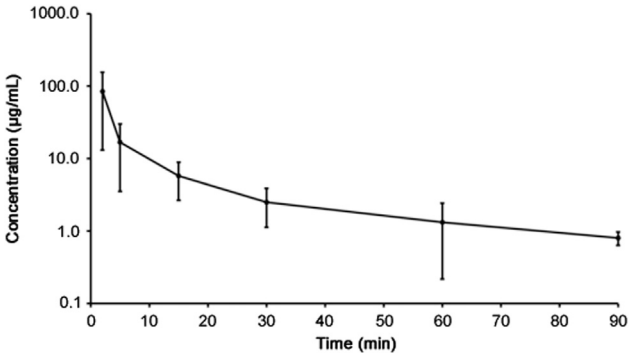

Fig. 5. Plasma concentration-time profile of NMI-amide in mice after an intravenous dose of 5 mg/kg.

3.3. Pharmacokinetic results

The mean plasma concentration–time profile of NMI-amide in C57B/L mice following intravenous injection at a dose of 5 mg/kg is shown in Fig. 5. The pharmacokinetic profile after intravenous injection indicates that NMI-amide pharmacokinetics followed a typical three-compartmental model with a very rapid distribution phase and a slow terminal elimination phase ($t_{1/2}$ of 36.6 min). All other relevant pharmacokinetic parameters are listed in Table 5.

4. Discussion

MHI dye imaging agent was for the first time detected and quantified using an HPLC and mass spectrometry based method. Such method could provide much higher sensitivity which is necessary for pharmacokinetic studies. Before developing the HPLC–MS/MS method, a UV detector was used with the maximum absorption wavelength of NMI-amide at 400 nm. However, the sensitivity of this method was too low and not feasible for a pharmacokinetic study. NMI-amide was well detected using mass spectrometry with acceptable sensitivity (LLOQ 5 ng/mL). The doubly protonated ion $[M + 2H]^{2+}$ was found to be most intensive as the parent ion for NMI-amide with the daughter ion fragments shown in Fig. 2A. Among these daughter ions, the highest response ion (361.7) was selected as a quantifier, while the second highest ion (410.5) as a qualifier. The variation of the peak ratio (qualifier/quantifier) was < 13.9% for all the samples tested, which was within the tolerance (30%) suggested by SANCO/12571/2013 guideline [13]. The results indicated a good specificity of this MS/MS method.

NMI-amide was found temperature sensitive and not stable at room temperature. Thus, the whole process of sample preparation

Table 5
Pharmacokinetic parameters of MHI148-clorgyline amide following an intravenous dose of 5 mg/kg ($n = 3$).

Parameters	Mean value
$t_{1/2}$ (min)	36.6
$AUC_{0-90\ min}$ (μg h/mL)	831.81
AUC_{0-inf} (μg h/mL)	832.76
CL (mL/h/kg)	7.75
V_d (mL/kg)	9.73

(formulation preparation, blood sampling, plasma separation, and compound extraction) was carried out on ice or under 4 °C whenever possible. Under this condition, NMI-amide was identified to be stable at least for 4 h, which could guarantee the completion of the assay without significant degradation of NMI-amide.

The internal standard, MHI-148, can be used as an imaging agent for cancers detection using a fluorescence detector [4,14], while its derivative, NMI-amide, can also be detected by a fluorescence detector or UV detector. However, the mass spectrometry was utilized with higher sensitivity and specificity. The recovery of MHI-148 was relatively low, probably due to the high protein binding. As a type of near infrared heptamethine cyanine dye, MHI-148 may bind to albumin and/or low-density lipoprotein [15]. However, the recovery was found to be stable and had no significant impact on the method reproducibility.

The assay method was found sensitive enough for quantification of NMI-amide in plasma sample up to 1.5 h. The pharmacokinetic profile of NMI-amide indicated that it may follow a three-compartmental model which suggests that the permeability of NMI-amide is quite different in central compartments (main the blood) and tissues. A relative short plasma elimination half-life was observed for NMI-amide (36.6 min) which may be caused by the metabolism and/or chemical degradation. This information will be used for dosage determination for future efficacy study and/or clinical trials.

5. Conclusions

A new HPLC–MS/MS assay for NMI-amide in mouse plasma has been successfully established and validated. This assay method is highly sensitive and specific, which has been proven useful for a pharmacokinetic study. The availability of this validated analytical method for NMI-amide will facilitate its further development as a novel tumor-targeting agent.

Conflicts of interest

Drs. B. Olenyuk and JC Shih have the patent on MHI-clorgyline, which is the same compound as MHI148-clorgylineamide (NMI-amide).

Acknowledgments

This work was supported by USC-Taiwan Center for Translational Research, the Daniel Tsai Family Fund and Boyd & Elsie Welin Professorship and by the Department of Defense Prostate Cancer Research Program Grant W81XWH-12-1-0282 (to J.C. Shih and B.Z. Olenyuk). We also thank Dr. Rajesh Kota, Dr. Ramin Dubey and Dr. Ivan V. Grishagin for help in synthesizing NMI-amide and precursors and Mr. Bin Qian for assistance in animal experiments (Department of Pharmacology and Pharmaceutical Sciences, University of Southern California, Los Angeles, CA, USA).

References

[1] J.C. Shih, K. Chen, M.J. Ridd, Monoamine oxidase: from genes to behavior, Annu. Rev. Neurosci. 22 (1999) 197–217.
[2] M. Bortolato, K. Chen, J.C. Shih, Monoamine oxidase inactivation: from pathophysiology to therapeutics, Adv. Drug Deliv. Rev. 60 (2008) 1527–1533.
[3] V. Flamand, H. Zhao, D.M. Peehl, Targeting monoamine oxidase A in advanced prostate cancer, J. Cancer Res. Clin. Oncol. 136 (2010) 1761–1771.
[4] J.B. Wu, C. Shao, X. Li, et al., Monoamine oxidase A mediates prostate tumorigenesis and cancer metastasis, J. Clin. Invest. 124 (2014) 2891–2908.
[5] H. Zhao, V. Flamand, D.M. Peehl, Anti-oncogenic and pro-differentiation effects of clorgyline, a monoamine oxidase A inhibitor, on high grade prostate cancer cells, BMC Med. Genom. 2 (2009) 55.
[6] J.B. Wu, T.P. Lin, J.D. Gallagher, et al., Monoamine oxidase A inhibitor–near-infrared dye conjugate reduces prostate tumor growth, J. Am. Chem. Soc. 137 (2015) 2366–2374.
[7] S. Kushal, W. Wang, V.P. Vaikari, et al., Monoamine oxidase A (MAO A) inhibitors decrease glioma progression, Oncotarget 7 (2016) 13842–13853.
[8] J. Logan, J.S. Fowler, Y.S. Ding, et al., Strategy for the formation of parametric images under conditions of low injected radioactivity applied to PET studies with the irreversible monoamine oxidase a tracers [11C]Clorgyline and deuterium-substituted [11C] clorgyline, J. Cereb. Blood Flow Metab. 22 (2002) 1367–1376.
[9] J. Yuan, X. Yi, F. Yan, et al., Near-infrared fluorescence imaging of prostate cancer using heptamethine carbocyanine dyes, Mol. Med. Rep. 11 (2015) 821–828.
[10] US FDA, Guidance for Industry Bioanalytical Method Validation, Food and Drug Administration, Center for Drug Evaluation and Research (CDER), Rockville, Maryland, USA, 2001.
[11] European Medicines Agency, Guideline on Bioanalytical Method Validation, 2011.
[12] Z. Wang, S. Qian, Q. Zhang, et al., Quantification of meclizine in human plasma by high performance liquid chromatography-mass spectrometry, J. Chromatogr. B Anal. Technol. Biomed. Life Sci. 879 (2011) 95–99.
[13] European Commission, Health & Consumer protection Directorate-General, Guidance document on analytical quality control and validation procedures for pesticide residues analysis in food and feed, SANCO/12571/2013, 2013.
[14] X. Yang, C. Shi, R. Tong, et al., Near IR heptamethine cyanine dye–mediated cancer imaging, Clin. Cancer Res. 16 (2010) 2833–2844.
[15] C. Shi, J.B. Wu, D. Pan, Review on near-infrared heptamethine cyanine dyes as theranostic agents for tumor imaging, targeting, and photodynamic therapy, J. Biomed. Opt. 21 (2016) 50901.

Journal of Pharmaceutical Analysis 8 (2018) 160–167

Contents lists available at ScienceDirect

Journal of Pharmaceutical Analysis

journal homepage: www.elsevier.com/locate/jpa
www.sciencedirect.com

Original Research Article

Simultaneous determination of acetaminophen and oxycodone in human plasma by LC–MS/MS and its application to a pharmacokinetic study

Wei Lu [a,b], Shunbo Zhao [b], Meng Gong [a,b], Luning Sun [c], Li Ding [a,b,*]

[a] Department of Pharmaceutical Analysis, China Pharmaceutical University, 24 Tongjiaxiang, Nanjing 210009, PR China
[b] Nanjing Clinical Tech Laboratories Inc., 18 Zhilan Road, Jiangning District, Nanjing 211000, PR China
[c] Research Division of Clinical Pharmacology, the First Affiliated Hospital, Nanjing Medical University, Nanjing 210029, PR China

ARTICLE INFO

Article history:
Received 15 October 2017
Received in revised form
22 January 2018
Accepted 26 January 2018
Available online 31 January 2018

Keywords:
Acetaminophen
Oxycodone
LC–MS/MS
Human plasma
Pharmacokinetics

ABSTRACT

A simple and rapid liquid chromatography–tandem mass spectrometry (LC–MS/MS) method was developed and validated for simultaneous determination of acetaminophen and oxycodone in human plasma. Acetaminophen-d4 and oxycodone-d3 were used as internal standards. The challenge encountered in the method development that the high plasma concentration level of acetaminophen made the MS response saturated while the desired lower limit of quantification (LLOQ) for oxycodone was hard to reach was well solved. The analytes were extracted by protein precipitation using acetonitrile. The matrix effect of the analytes was avoided by chromatographic separation using a hydrophilic C_{18} column coupled with gradient elution. Multiple reaction monitoring in positive ion mode was performed on tandem mass spectrometer employing electrospray ion source. The calibration curves were linear over the concentration ranges of 40.0–8000 ng/mL and 0.200–40.0 ng/mL for acetaminophen and oxycodone, respectively. This method, which could contribute to high throughput analysis and better clinical drug monitoring, was successfully applied to a pharmacokinetic study in healthy Chinese volunteers.

1. Introduction

Acetaminophen is a frequently used analgesic and antipyretic drug worldwide. Oxycodone hydrochloride, a semi-synthetic opiate derivative of thebaine, is widely used in analgesic agents due to remarkable analgesia effect and good tolerance [1]. The FDA-approved Percocet [2], combining acetaminophen with oxycodone, can be effective in pain control and help in reducing side effects and drug dependence. The commonly used dosage regimen is 325 mg and 5 mg for acetaminophen and oxycodone, respectively. The combination of acetaminophen and oxycodone provides a synergistic and opioid-sparing effect. Additionally, this combination has a safe pharmacokinetic profile, without increasing the incidence of drug addiction and acetaminophen-associated hepatotoxicity [3–7]. As the abuse of prescription opioids continues to rise, measurement of acetaminophen and oxycodone in human plasma will help researchers with better drug monitoring.

Several methods have been developed for the determination of acetaminophen in biological matrix, including immunoassay [8], gas chromatography (GC) [9,10], capillary electrophoresis [11], high performance liquid chromatography (HPLC) with UV detector [12–16] or with tandem mass spectrometer [17–19]. The analysis of oxycodone alone or with its major metabolites in human plasma with electrochemical detection [20,21], GC [22,23], liquid chromatography–tandem mass spectrometry (LC–MS) [24,25] and liquid chromatography–tandem mass spectrometry (LC–MS/MS) [26–37] has also been reported. Literature survey revealed that the majority of published methods determined acetaminophen and oxycodone in biological fluids individually, or in combination with other drugs [38–42]. Devarakonda et al. [43] quantified acetaminophen and oxycodone in plasma with liquid-liquid extraction, but the sample preparation and method validation were not clearly described.

Simultaneous determination of acetaminophen and oxycodone in human plasma by LC–MS/MS is challenged by two problems, one is the weak retention of the analytes on traditional C_{18} columns, and the other is that the plasma concentration of acetaminophen is much higher than that of oxycodone. The present article focuses on troubleshooting in method development, including screening of columns for better retention of the analytes, and overcoming the MS response saturation to acetaminophen

Peer review under responsibility of Xi'an Jiaotong University.

Abbreviations: LLOQ, lower limit of quantification; LQC, low quality control; MQC, middle quality control; HQC, high quality control

* Corresponding author at: Department of Pharmaceutical Analysis, China Pharmaceutical University, 24 Tongjiaxiang, Nanjing 210009, PR China.
E-mail address: dinglidl@hotmail.com (L. Ding).

https://doi.org/10.1016/j.jpha.2018.01.006

while ensuring the detection sensitivity for oxycodone. Finally, the application of the validated method to a clinical pharmacokinetic study in healthy Chinese volunteers following oral administration of Percocet tablet is described.

2. Experimental

2.1. Chemicals and reagents

The reference standards of acetaminophen and acetaminophen-d4 were purchased from Toronto Research Chemicals (Toronto, Canada). The reference standards of oxycodone hydrochloride and oxycodone-d3 solution were purchased from Sigma-Aldrich Company, USA. HPLC grade methanol and acetonitrile were purchased from Merck KGaA (Darmstadt, Germany). Acetic acid and ammonium acetate were obtained from Sigma-Aldrich Company, USA. Ultrapure water was generated in house with a Milli-Q system (Millipore, Bedford, MA, USA) and was used throughout the study. Blank human plasma was obtained from healthy Chinese volunteers. All the volunteers were given informed consent.

2.2. Liquid chromatography and mass spectrometric conditions

An Exion LC system (Applied Biosystems/Sciex, USA) consisted of a binary AD pump, a vacuum degasser, an autosampler (AD multiplate sampler) and a temperature-controlled compartment for column (AD column oven). Separation of analytes was performed on a Venusil ASB C_{18} column (2.1 mm × 50 mm, 3 μm, 150 A; Bonna-Agela Technologies, Tianjin, China) with a Security Guard Cartridges C_{18} (4 mm × 2.0 mm, Phenomenex, Torrance, CA, USA) maintained at 40 °C. The autosampler temperature was set at 8 °C. The mobile phase was composed of 2 mM ammonium acetate containing 0.1% (v/v) acetic acid (A; pH 3.6) and acetonitrile (B). The gradient elution program started at a composition of 6% B for 0.4 min, and then was ramped to 15% B at 0.5 min and held for another 1.5 min. The composition of mobile phase B was maintained at 80% from 2.1 min to 2.8 min. The system returned to the initial condition at 3.0 min and held for another 1.5 min. The total run time was 4.5 min and the flow rate was constantly 0.5 mL/min. The injection volume was 5 μL.

Detection of analytes and internal standards was operated on a triple quadrupole mass spectrometer, AB SCIEX Triple Quad™ 6500+ (Applied Biosystems/Sciex, USA), equipped with an electrospray ion source in positive mode. Quantitation was performed using the multiple reaction monitoring (MRM) with a dwell time of 100 ms per transition. The MRM parameters of acetaminophen, oxycodone, acetaminophen-d4 and oxycodone-d3 are listed in Table 1. The optimized source parameters were as follows: 30 psi for curtain gas; 8 psi for collision activation dissociation; 650 °C for turbo heater temperature; 3500 V for ionspray voltage; 50 psi for Gas 1; 55 psi for Gas 2. Quadrupole 1 and quadrupole 3 were maintained at unit resolution. Data processing was performed using Analyst 1.6.3 software. The fragmentation of acetaminophen (A), oxycodone (B), acetaminophen-d4 (C) and oxycodone-d3 (D) is given in Fig. 1.

Table 1
MRM parameters of acetaminophen, oxycodone, acetaminophen-d4 and oxycodone-d3.

Analytes	Precursor ion (Da)	Product ion (Da)	DP (V)	EP (V)	CE (V)	CXP (V)
Acetaminophen	152.0	110.1	38	8	42	12
Oxycodone	316.1	241.1	56	12	39	13
Acetaminophen-d4	155.8	114.1	90	14	30	11
Oxycodone-d3	319.0	244.1	84	8	39	10

DP, declustering potential; EP, entrance potential; CE, collision energy; CXP, collision cell exit potential.

2.3. Preparation of stock and working solutions

Primary stock solutions for preparation of calibration standards and quality control (QC) samples were prepared from separate weighing. The standard stock solutions of acetaminophen, oxycodone and acetaminophen-d4 were prepared by dissolving accurately weighed compounds in acetontrile-water (50:50, v/v) to give a concentration of 1.0 mg/mL. The primary standard solution of oxycodone-d3 in methanol was provided at a certified concentration of 1.0 mg/mL. The combined working solutions of analytes over the desired concentration range were prepared by further dilution of stock solutions with acetontrile-water (50:50, v/v). A combined internal standard working solution was prepared in acetontrile-water (50:50, v/v) at 10.0 ng/mL for oxycodone-d3 and 80.0 ng/mL for acetaminophen-d4. All stock and working solutions were stored at −20 °C and brought to room temperature before use.

2.4. Preparation of calibration standards and QC samples

The calibration standards and QC samples were prepared by spiking plasma with appropriate volume of respective working solutions. Calibration standards were prepared at concentrations of 40.0, 80.0, 200, 600, 2000, 5000, and 8000 ng/mL for acetaminophen; 0.200, 0.400, 1.00, 3.00, 10.0, 25.0, and 40.0 ng/mL for oxycodone. QC samples were prepared at 40.0 ng/mL (lower limit of quantification, LLOQ), 100 ng/mL (low QC, LQC), 1200 ng/mL (middle quality control, MQC), and 6400 ng/mL (high quality control, HQC) for acetaminophen; 0.200 ng/mL (LLOQ), 0.500 ng/mL (LQC), 6.00 ng/mL (MQC), and 32.0 ng/mL (HQC) for oxycodone.

2.5. Sample preparation

50 μL aliquot of plasma sample was transferred to a clean 96-well plate and mixed with 25 μL of internal standard working solution. The mixture was deproteinized with 200 μL acetonitrile, vortex-mixed for 10 min, and then centrifuged at 4000 rpm for 10 min. 30 μL of the supernatant was transferred to another clean 96-well plate, to which 330 μL of acetontrile-water (10:90, v/v) was added. After vortex mix for 3 min, the mixture was injected into the LC-MS/MS system for analysis.

2.6. Method validation

The validation of this method was carried out following the USFDA guidelines [44]. The validation included specificity, linearity, precision and accuracy, recovery, matrix effect, dilution integrity, carryover effect and stability.

The specificity was tested for interference in the MRM channels using the proposed extraction procedure and LC–MS/MS conditions. Six batches of blank plasma obtained from six individual volunteers were analyzed and the results were compared to those obtained from samples at LLOQ. Best-fit calibration curves of peak area ratio versus analyte concentrations were drawn for acetaminophen and oxycodone. The calibration curve was fitted to a $1/x^2$ weighed regression analysis where x is the concentration of the analyte. Precision and accuracy were evaluated at four concentration levels (LLOQ, LQC, MQC, and HQC) in six replicates. Intra-run precision and accuracy were assessments of precision and accuracy during a single analytical run. Inter-run precision and

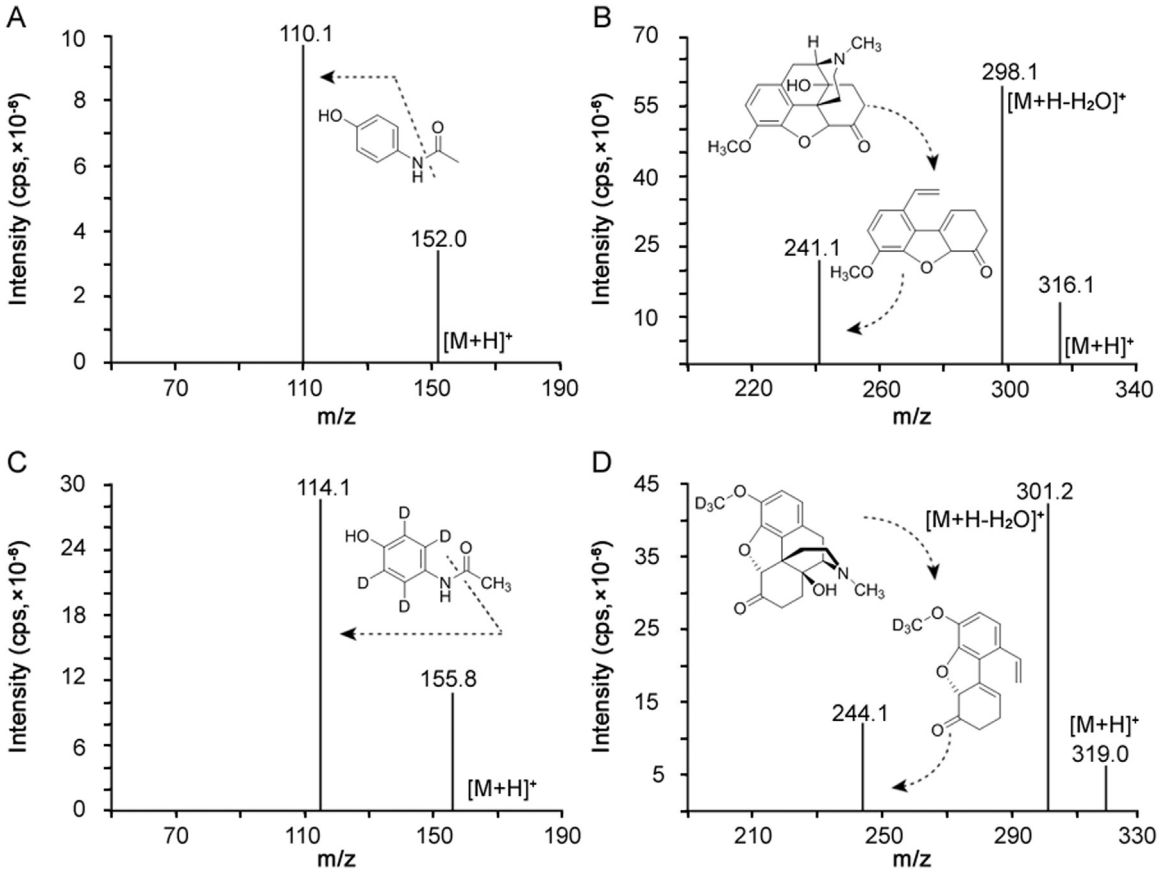

Fig. 1. Product ion mass spectra of (A) acetaminophen, (B) oxycodone, (C) acetaminophen-d4 and (D) oxycodone-d3 in positive mode and their proposed fragmentation patterns.

accuracy were evaluated over two days by quantification of three validation runs. Recovery experiments were performed by comparing peak area of extracted samples (spiked before extraction) to the peak area of unextracted samples (QC working solutions spiked in extracted plasma) at LQC, MQC and HQC levels. The matrix effect was assessed by comparing the peak area obtained from an amount of the analyte added in extracted blank plasma to the peak area obtained from equal concentration of the analyte in solvent. Dilution integrity was performed with six replicates each for samples spiked at concentrations of HQC and 2 times of the upper limit of quantification (ULOQ) diluted 5-fold with blank plasma. In this study, stability tests evaluated the stability of acetaminophen and oxycodone in stock solutions and plasma samples under different conditions. For stock solutions, the stability was evaluated by comparing the area response of analytes in stability samples to that of freshly prepared stock solutions. For plasma samples, bench top stability, autosampler stability, freeze-thaw stability and long-term stability were evaluated with three replicates each at LQC and HQC levels.

2.7. Pharmacokinetic study

Ten healthy Chinese volunteers were enrolled in the clinical pharmacokinetic study. Preliminary screening involved a medical history, physical examination, medical and laboratory evaluations. The protocol approval was obtained from a local ethics committee and informed consent was obtained from each subject. After an overnight fast of at least 10 h, all subjects were administered with a single dose of one Percocet tablet (acetaminophen/oxycodone, 325 mg/5 mg, Endo Pharmaceuticals Inc.). Blood samples were collected before drug administration (0 h) and at 0.17, 0.33, 0.5, 0.75, 1, 1.33, 1.67, 2, 2.5, 3, 4, 5, 6, 8, 10, 12 and 24 h post-dosing. Whole blood was collected into heparinized tubes and centrifuged at 3000 rpm for 5 min. The plasma samples were stored at −20 °C until analysis. The pharmacokinetic parameters were calculated with non-compartment model using WinNonlin software version 6.4.

3. Results and discussion

3.1. Method development

The method development included selection of mobile phase, column types, MS detector, MS parameters and sample extraction. Acetaminophen and oxycodone are compounds with low lipophilicity and retain weakly on C_{18} columns; thus the initial organic phase ratio should be low to achieve appropriate chromatographic separation. In the column screening stage, appropriate retention for both acetaminophen and oxycodone could not achieve on numerous C_{18} columns, such as a Zorbax Eclipse Plus C_{18} column (2.1 mm × 50 mm, 3.5 μm; Agilent Technologies), a Zorbax Extend-C_{18} column (2.1 mm × 50 mm, 3.5 μm; Agilent Technologies) and a Poroshell 120 SB-C_{18} column (2.1 mm × 50 mm, 2.7 μm; Agilent Technologies), except on an Ultimate XB-C_{18} column (2.1 mm × 100 mm, 3 μm; Welch Materials, Inc., Shanghai, China). It was observed that pure water and acetonitrile as mobile phase gave the best sensitivity and peak shape on the Ultimate XB-C_{18} column. Tailing peak was observed when methanol was used as mobile phase B. Addition of acid in mobile phase A resulted in oxycodone eluted at dead time and addition of ammonium acetate led to unacceptable peak shapes of oxycodone. However, endogenous interference and matrix effect existed while pure water

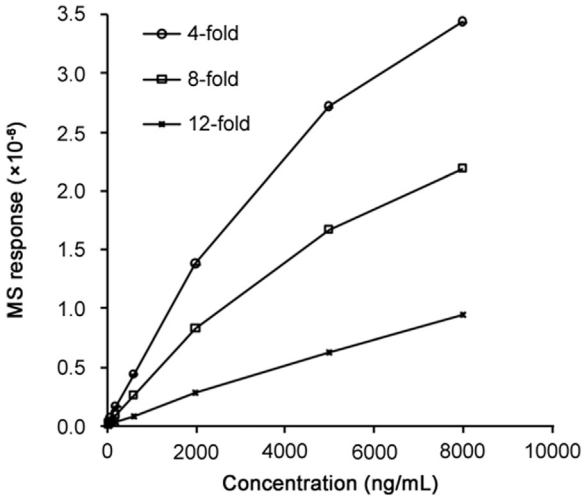

Fig. 2. The MS response to acetaminophen obtained by using different volumes of acetontrile-water (10:90, v/v) to dilute the supernatant of deproteinized samples.

was employed as mobile phase A. A Venusil ASB C_{18} column (2.1 mm × 50 mm, 3 μm, 150 Å) was then tested. The optimized mobile phase was composed of 2 mM ammonium acetate containing 0.1% (v/v) acetic acid and acetonitrile to achieve symmetrical peak shapes and better MS response. Higher concentration of ammonium acetate at 5 mM and 10 mM would inhibit MS response for all analytes. More addition of acid like 0.2% (v/v) acetic acid or 0.1% (v/v) formic acid in aqueous mobile phase would weaken the chromatographic retention of the analytes. The difference between the above two columns lies in that the Ultimate XB-C_{18} column is a traditional reversed-phase column with end-capping while the Venusil ASB C_{18} column is an uncapped hydrophilic column. The end-capping process might increase the lipophilicity of stationary phase, resulting in weak absorption of polar compounds. The hydrophilic column could provide better chromatographic retention and separation for strong polar compounds within a pH range of 1–5. The proportion of organic phase started at 6% to elute endogenous substance, and then increased to 15% to separate acetaminophen and oxycodone. Optimized flow rate of 0.5 mL/min helped in separation and elution of all compounds in 2 min. Whereafter, the composition of mobile phase B was set at 80% for 0.8 min to wash column and inhibit matrix effect. The elution program changed to the initial condition in order to back toward equilibrium state.

The MS-MS detection was initially performed on an API 4000 mass spectrometer (Applied Biosystems/Sciex, USA). The plasma concentration of acetaminophen was much higher than that of oxycodone after oral administration of Percocet tablet. If the analytes in plasma were not diluted, the plasma concentration of acetaminophen would be so high that the saturation of MS response to acetaminophen would result in its poor linearity of calibration curve. This means that the analytes in plasma should be diluted for determination of acetaminophen. However, if the plasma sample was massively diluted, the quantification of oxycodone at LLOQ was difficult to ensure. Even though the much higher sensitive instrument AB SCIEX Triple Quad™ 6500+ was applied, the problems were not easily overcome without further optimization described below.

By using an AB SCIEX Triple Quad™ 6500+ mass spectrometer, the protonated molecular ion $[M+H]^+$ was chosen as the parent ion in the Q1 full scan spectra for acetaminophen, oxycodone and the internal standards. The parent ion was used as the precursor ion to obtain the product ion in the Q3 spectra. The fragment ions with the highest relative abundance were at *m/z* 110.1, 298.1, 114.1, and 301.1 for acetaminophen, oxycodone, acetaminophen-d4 and oxycodone-d3, respectively (Fig. 1). Interestingly, MRM transitions at *m/z* 316.1→241.1 for oxycodone and *m/z* 319.0→244.1 for oxycodone-d3 showed more steady and reproducible signal intensities. Gaudette et al. [35] reported the fragmentation pattern of these transitions. The authors speculated that transitions at *m/z* 316.1→298.1 for oxycodone and *m/z* 319.0→301.1 for oxycodone-d3 might be the results of dehydration rearrangements. The mass-to-charge ratios of $[M+H\text{-}H_2O]^+$ ions for oxycodone and oxycodone-d3 corresponded to 298.1 and 301.1. Ion source parameters and electrical parameters were optimized by monitoring the selected mass transition for the analytes. The great difference in the concentration ranges between acetaminophen and oxycodone made it challenging that both analytes in processed samples could give suitable signal intensities simultaneously via the same sample preparation. In order to avoid the MS response saturation to acetaminophen as well as guarantee the LLOQ of oxycoden detection, the analytes in plasma were diluted to a limited extent. Despite massive dilution of analytes in plasma, the MS response saturation to acetaminophen could not be avoided completely. Optimization of collision energy was also conducted to make fewer product ions of acetaminophen generated in Q3 to avoid the MS response saturation to acetaminophen. The MS condition optimization test showed that to obtain the highest intensity for acetaminophen, the collision energy of 20 V should be adapted. Actually, a collision energy we wanted should inhibit the MS response saturation to acetaminophen. This meant that the collision energy should be increased appropriately to decrease the generation of the product ions of acetaminophen to an acceptable extent. Finally, the collision energy for acetaminophen was adjusted to 42 V to obtain adaptive MS response. Other optimized parameters are listed in Table 1.

Previous pharmacokinetic research of drug formulations combining acetaminophen and oxycodone reported extraction of acetaminophen and oxycodone simultaneously from human plasma with liquid-liquid extraction [43]. As the purpose was to develop a simple and rapid method, protein precipitation was tested. Precipitants including methanol, acetonitrile and methanol-acetontrile (1:1, v/v) were compared. Single precipitant of acetonitrile showed higher extraction recovery and negligible matrix effect. Due to the saturation of MS response to acetaminophen at high concentration level, the volume of acetontrile-water (10:90, v/v) used to dilute the supernatant of deproteinized samples was tested. The results of a 4-fold dilution, an 8-fold dilution and a 12-fold dilution are given in Fig. 2. A 12-fold dilution, 30 μL of the supernatant diluted with 330 μL of acetontrile-water (10:90, v/v), showed the best linearity. The major advantage was its efficiency in simultaneous extraction of both analytes and internal standards with single step of protein precipitation.

3.2. Method validation

3.2.1. Specificity

The typical chromatograms of blank plasma, drug-free plasma spiked with both analytes at LLOQ and a clinical sample from a volunteer at 4 h after single oral administration of one Percocet tablet are shown in Fig. 3. No significant endogenous interference was observed in blank plasma at the retention time of acetaminophen, oxycodone and internal standards. Potential interference of stable isotope-labeling internal standards was also evaluated in this study. The internal standards had no interference in the channel of acetaminophen and oxycodone.

3.2.2. Linearity

The calibration curves showed good linearity over the concentration of 40.0–8000 ng/mL for acetaminophen and 0.200–40.0 ng/mL for oxycodone. The correlation coefficient (r) of the

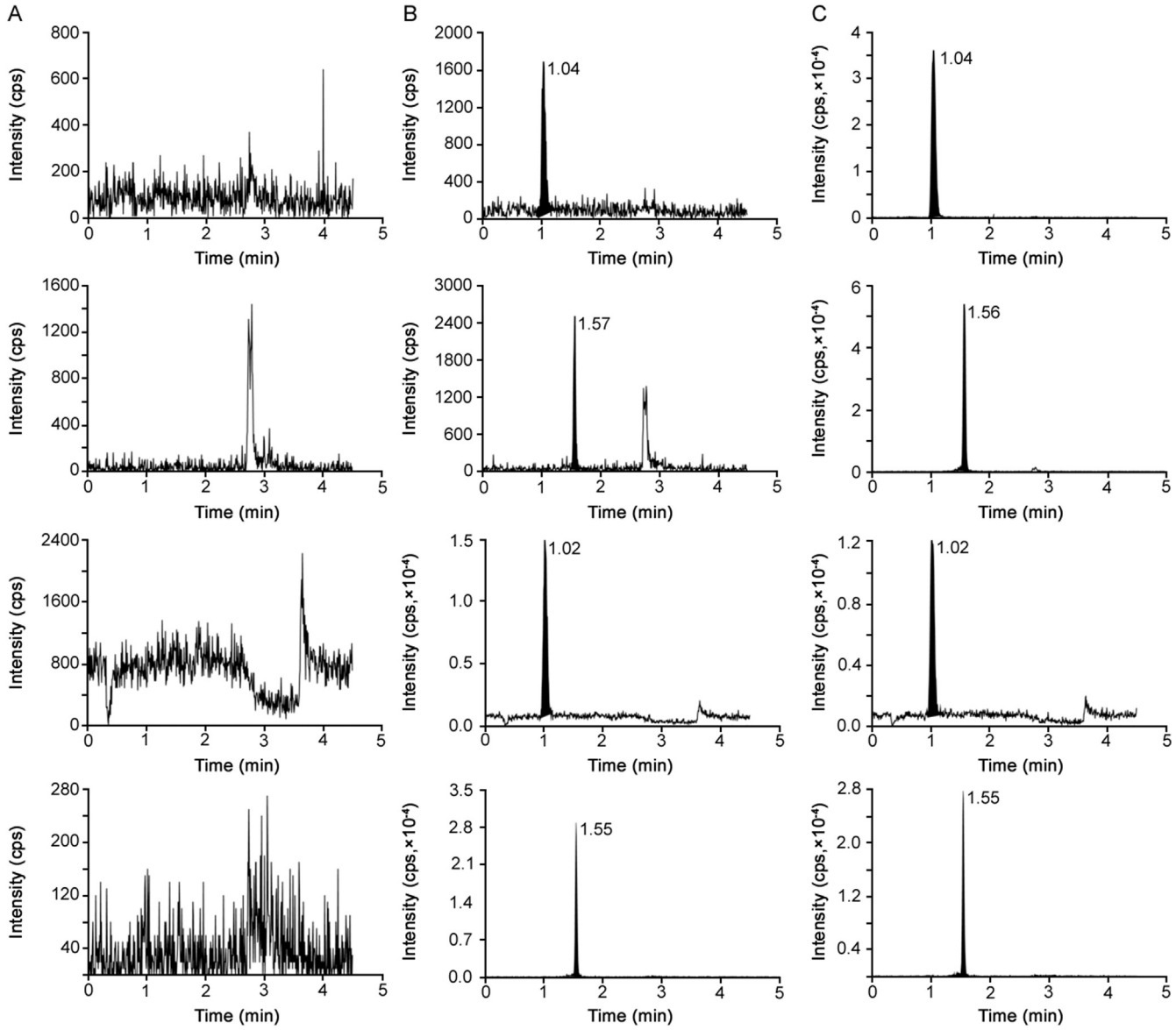

Fig. 3. Typical MRM chromatograms of acetaminophen, oxycodone and internal standards: (A) blank human plasma, (B) calibration standards at LLOQ and (C) a clinical sample from a volunteer at 4 h after single oral administration of one Percocet tablet.

Table 2
Intra-run and inter-run precision and accuracy data for acetaminophen and oxycodone in human plasma.

Analytes	Intra-run			Inter-run		
	Mean concentration (ng/mL)	Accuracy (%)	CV%	Mean concentration (ng/mL)	Accuracy (%)	CV%
Acetaminophen						
LLOQ QC (40.0 ng/mL)	38.7 ± 0.5	96.8	1.3	39.3 ± 3.3	98.3	8.4
LQC (100 ng/mL)	97.0 ± 4.1	97.0	4.2	101 ± 9	101.0	8.9
MQC (1200 ng/mL)	1160 ± 17	96.7	1.5	1187 ± 42	98.9	3.5
HQC (6400 ng/mL)	6097 ± 201	95.3	3.3	6130 ± 180	95.8	2.9
Oxycodone						
LLOQ QC (0.200 ng/mL)	0.196 ± 0.019	98.0	9.7	0.198 ± 0.020	99.0	10.1
LQC (0.500 ng/mL)	0.513 ± 0.028	102.6	5.5	0.507 ± 0.010	101.4	2.0
MQC (6.00 ng/mL)	5.96 ± 0.16	99.3	2.7	6.05 ± 0.15	100.8	2.5
HQC (32.0 ng/mL)	32.0 ± 1.4	100.0	4.4	32.2 ± 1.1	100.6	3.4

The mean concentration was presented in the form of mean ± SD. CV, coefficient of variation.

weighed calibration curves for both analytes during the validation was ≥ 0.995. Precision and accuracy of the back-calculated concentrations of calibration standards well met the acceptance criteria.

3.2.3. Precision and accuracy

The intra-run and inter-run precision and accuracy was summarized in Table 2. The regression equations for calibration curves were used to back-calculate the measured values of QC samples at

four concentration levels. For both acetaminophen and oxycodone, the deviations of mean value from the nominal value were all within ± 15% and the coefficient of variation (CV) determined at each concentration level did not exceed 10.1%.

3.2.4. Recovery

Six replicates at LQC, MQC and HQC were prepared for recovery experiment. The recovery extent of each analyte and its corresponding internal standard was consistent and reproducible. The mean recovery data (with the precision) at LQC, MQC and HQC was 96.0% (7.6%), 94.7% (5.0%), and 95.7% (4.5%) for acetaminophen; 91.1% (5.4%), 94.0% (2.4%), and 94.7% (2.3%) for oxycodone. The recovery of acetaminophen-d4 was 95.3% with the precision of 9.3%. The recovery of oxycodone-d3 was 94.1% with the precision of 2.6%.

3.2.5. Matrix effect

No significant matrix effect was observed in six batches of human plasma for both analytes at three concentration levels (low, middle and high). The matrix effects at concentrations of LQC, MQC and HQC were (96.7 ± 6.0) %, (97.8 ± 3.2) %, and (98.5 ± 1.4) % for acetaminophen; (96.6 ± 2.7) %, (98.6 ± 1.1) %, and (97.3 ± 1.0) % for oxycodone. The matrix effect of acetaminophen-d4 and oxycodone-d3 was (92.4 ± 1.6) % and (98.7 ± 1.6) %, respectively.

3.2.6. Dilution integrity

The diluted samples were prepared by a 5-fold dilution of samples at HQC and 2 times of the ULOQ with blank plasma. The determined concentrations were corrected for dilution factor. The mean back calculated concentrations for both analytes at each level were within 85%–115% of their nominal values. The maximum of CV was 6.8%. The results demonstrated that the ULOQ could be extended to 16,000 ng/mL for acetaminophen and 80.0 ng/mL for oxycodone by a 5-fold dilution with blank plasma.

3.2.7. Carryover effect

Carryover was assessed and monitored by analyzing blank plasma samples instantly following plasma samples at ULOQ. No obvious response at the retention time of analytes was observed in blank matrix samples.

3.2.8. Stability

The stock solution was found to be stable for 20 h at room temperature and 33 days at −20 °C. Table 3 lists the stability of acetaminophen and oxycodone in human plasma under different conditions. Bench top stability experiment was conducted to keep QC samples at room temperature for 24 h. The freeze-thaw stability was determined over three freeze-thaw cycles. The processed samples were analyzed after being kept in autosampler at 8 °C for 24 h (autosampler stability). The storage time for evaluating long-term stability at −20 °C was designed to be 23 days.

Table 3
Stability of acetaminophen and oxycodone in human plasma under different storage conditions.

Storage conditions	Analytes	Nominal (ng/mL)	Mean (ng/mL)	RE (%)	CV (%)
Autosampler stability (24 h, 8 °C)	Acetaminophen	100	99.7	−0.3	5.5
		6400	6247	−2.4	5.8
	Oxycodone	0.500	0.507	1.4	7.7
		32.0	31.6	−1.3	4.4
Bench top stability (24 h, room temperature)	Acetaminophen	100	98.7	−1.3	1.0
		6400	6170	−3.6	1.6
	Oxycodone	0.500	0.503	0.6	3.2
		32.0	30.7	−4.1	2.0
Freeze-thaw stability (3 cycles, −20 °C)	Acetaminophen	100	103	3.0	2.9
		6400	5740	−10.3	4.2
	Oxycodone	0.500	0.510	2.0	4.1
		32.0	30.6	−4.4	2.3
Long-term stability (23 days, −20 °C)	Acetaminophen	100	93.3	−6.7	5.0
		6400	5740	−10.3	0.5
	Oxycodone	0.500	0.511	2.2	10.2
		32.0	31.5	−1.6	4.1

RE, relative error; CV, coefficient of variation.

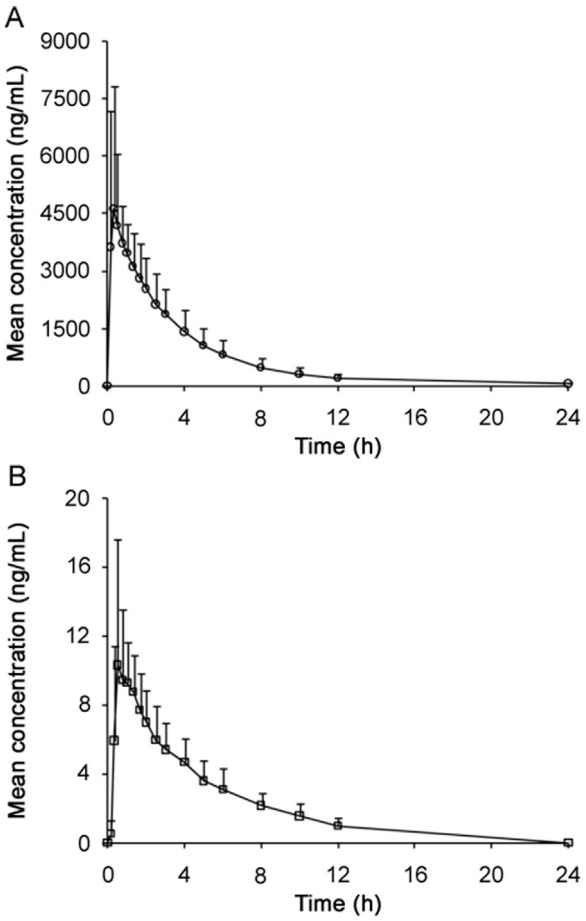

Fig. 4. Mean plasma concentration-time profiles of (A) acetaminophen and (B) oxycodone in human plasma.

3.3. Method application

The validated method was applied to quantify acetaminophen and oxycodone in human plasma samples collected from healthy Chinese volunteers after a single oral administration of one Percocet tablet. The mean plasma concentration-time profile of acetaminophen and oxycodone is shown in Fig. 4. The typical pharmacokinetic parameters are presented in Table 4. No literature revealed the pharmacokinetic profile of acetaminophen after administration of Percocet. Gammaitoni et al. [30] only evaluated the pharmacokinetics of oxycodone following single-dose administration of Percocet at three dose levels. For the 325 mg/5 mg (acetaminophen/oxycodone) dose level, the reported mean values of peak plasma concentration (C_{max}), area under the plasma concentration-time curve from 0 h to 24 h (AUC_{0-24}), time to peak plasma concentration (T_{max}) and terminal elimination half-life ($t_{1/2}$) were 9.96 ng/mL, 48.62 h ng/mL, 1.33 h and 3.28 h, respectively. AUC_{0-24} and $t_{1/2}$ of oxycodone listed in Table 4 were consistent with those earlier reported values. C_{max} of oxycodone in Table 4 was slightly higher than the value in the previous study while T_{max} was somewhat lower. This may be due to differences in race, age and genetics of the study subjects.

Table 4
Pharmacokinetic parameters of acetaminophen and oxycodone in healthy Chinese volunteers following oral administration of one Percocet tablet (mean ± SD, $n=10$).

Parameters	Acetaminophen	Oxycodone
C_{max} (ng/mL)	6326 ± 2574	12.8 ± 4.6
AUC_{0-24} (h ng/mL)	16,205 ± 5871	46.5 ± 17.0
$AUC_{0-\infty}$ (h ng/mL)	16,744 ± 6026	51.2 ± 18.1
T_{max} (h)	0.48 ± 0.41	0.77 ± 0.36
$t_{1/2}$ (h)	4.56 ± 2.16	3.74 ± 1.18
Ke (1/h)	0.185 ± 0.083	0.204 ± 0.072
MRT_{0-24} (h)	3.81 ± 1.04	4.17 ± 0.90
$MRT_{0-\infty}$ (h)	4.54 ± 1.42	5.49 ± 1.38

C_{max}, peak concentration in plasma; *AUC*, area under the plasma mean concentrations-time curve; T_{max}, time to peak concentration; $t_{1/2}$, terminal elimination half-life; *Ke*, elimination rate constant; *MRT*, mean residence time.

4. Conclusion

A simple method has been developed and validated for determination of acetaminophen and oxycodone in human plasma. To the best of our knowledge, no published methods are available for simultaneous quantification of acetaminophen and oxycodone in human plasma using protein precipitation so far. The validated method has advantages in terms of the usage of simple protein precipitation extraction and a short analysis time, which promotes high-throughput pharmacokinetic study and is useful for routine therapeutic drug monitoring. This method has been successfully applied to a pharmacokinetic study in healthy Chinese volunteers following oral administration of one Percocet tablet.

Conflicts of interest

The authors declare that there are no conflicts of interest.

References

[1] H. Ma, Y. Liu, L. Huang, et al., The adverse events of oxycodone in cancer-related pain: a systematic review and meta-analysis of randomized controlled trials, Medicine 95 (2016):e3341.
[2] L.R. Webster, B. Bath, R.A. Medve, Opioid formulations in development designed to curtail abuse: who is the target? Expert Opin. Investig. Drugs 18 (2009) 255–263.
[3] S. Natoli, M. Lazzari, R. Carpenedo, et al., Retrospective evaluation of a fixed-dose combination of oxycodone and acetaminophen to manage moderate pain: the lower the better, Adv. Ther. 33 (2016) 1025–1032.
[4] B. Ward, J.M. Alexander-Williams, Paracetamol revisited: a review of the pharmacokinetics and pharmacodynamics, Acute Pain. 2 (1999) 139–149.
[5] S.A. Cooper, H. Precheur, D. Rauch, et al., Evaluation of oxycodone and acetaminophen in treatment of postoperative dental pain, Oral. Surg. Oral. Med. Oral. Pathol. 50 (1980) 496–501.
[6] J.A. Forrest, J.A. Clements, L.F. Prescott, Clinical pharmacokinetics of paracetamol, Clin. Pharmacokinet. 7 (1982) 93–107.
[7] N. Huang, J. Zeng, J. Liang, et al., A randomized, double-blind, placebo-controlled study of oral oxycodone plus acetaminophen for the treatment of pain in photodynamic therapy on port wine stains, Photodiagnosis Photodyn. Ther. 11 (2014) 134–140.
[8] S.E. Halcomb, M.L. Sivilotti, A. Goklaney, et al., Pharmacokinetic effects of diphenhydramine or oxycodone in simulated acetaminophen overdose, Acad. Emerg. Med. 12 (2005) 169–172.
[9] A. Trettin, A.A. Zoerner, A. Bohmer, et al., Quantification of acetaminophen (paracetamol) in human plasma and urine by stable isotope-dilution GC-MS and GC-MS/MS as pentafluorobenzyl ether derivative, J. Chromatogr. B Analyt. Technol. Biomed. Life Sci. 879 (2011) 2274–2280.
[10] M.D. Rawlins, D.B. Henderson, A.R. Hijab, Pharmacokinetics of paracetamol (acetaminophen) after intravenous and oral administration, Eur. J. Clin. Pharmacol. 11 (1977) 283–286.
[11] M.E. Bosch, A.J.R. Sanchez, F.S. Rojas, et al., Determination of paracetamol: historical evolution, J. Pharm. Biomed. Anal. 42 (2006) 291–321.
[12] K. Allegaert, M.Y. Peeters, B. Beleyn, et al., Paracetamol pharmacokinetics and metabolism in young women, BMC Anesthesiol. 15 (2015): 163.
[13] K. Allegaert, B.J. Anderson, G. Naulaers, et al., Intravenous paracetamol (propacetamol) pharmacokinetics in term and preterm neonates, Eur. J. Clin. Pharmacol. 60 (2004) 191–197.
[14] O.Y.P. Hu, L.H. Pao, S.T. Ho, et al., Pharmacokinetic properties and relative bioavailability of acetaminophen tablets, J. Med. Sci. 11 (1991) 281–295.
[15] A.M. Rittau, A.J. McLachlan, Investigating paracetamol pharmacokinetics using venous and capillary blood and saliva sampling, J. Pharm. Pharmacol. 64 (2012) 705–711.
[16] R.A. Langford, M. Hogg, A.R. Bjorksten, et al., Comparative plasma and cerebrospinal fluid pharmacokinetics of paracetamol after intravenous and oral administration, Anesth. Analg. 123 (2016) 610–615.
[17] J. Cha, B.K. Kim, M.R. Gwon, et al., Development and validation of a UPLC-MS/MS method for the quantification of acetaminophen in human plasma and its application to pharmacokinetic studies, Transl. Clin. Pharmacol. 24 (2016) 30–36.
[18] S.F. Cook, J.K. Roberts, S. Samiee-Zafarghandy, et al., Population pharmacokinetics of intravenous paracetamol (acetaminophen) in preterm and term neonates: model development and external evaluation, Clin. Pharmacokinet. 55 (2016) 107–119.
[19] S.F. Cook, A.D. King, J.N. van den Anker, et al., Simultaneous quantification of acetaminophen and five acetaminophen metabolites in human plasma and urine by high-performance liquid chromatography-electrospray ionization-tandem mass spectrometry: method validation and application to a neonatal pharmacokinetic study, J. Chromatogr. B Analyt. Technol. Biomed. Life Sci. 1007 (2015) 30–42.
[20] J.J. Schneider, E.J. Triggs, D.W.A. Bourne, et al., Determination of oxycodone in human plasma by high-performance liquid chromatography with electrochemical detection, J. Chromatogr. B Biomed. Sci. Appl. 308 (1984) 359–362.
[21] K.P. Leow, M.T. Smith, J.A. Watt, et al., Comparative oxycodone pharmacokinetics in humans after intravenous, oral, and rectal administration, Ther. Drug Monit. 14 (1992) 479–484.
[22] P. Välitalo, M. Kokki, V.P. Ranta, et al., Maturation of oxycodone pharmacokinetics in neonates and infants: a population pharmacokinetic model of three clinical trials, Pharm. Res. 34 (2017) 1125–1133.
[23] B. Parodi, E. Russo, G. Caviglioli, et al., Buccoadhesive oxycodone hydrochloride disks: plasma pharmacokinetics in healthy volunteers and clinical study, Eur. J. Pharm. Biopharm. 44 (1997) 137–142.
[24] M. Kokki, M. Heikkinen, P. Välitalo, et al., Maturation of oxycodone pharmacokinetics in neonates and infants: oxycodone and its metabolites in plasma and urine, Br. J. Clin. Pharmacol. 83 (2017) 791–800.
[25] B. Lalovic, E. Kharasch, C. Hoffer, et al., Pharmacokinetics and pharmacodynamics of oral oxycodone in healthy human subjects: role of circulating active metabolites, Clin. Pharmacol. Ther. 79 (2006) 461–479.
[26] G.T. Hao, H.Y. Zhou, H.Z. Gao, et al., Pharmacokinetics of oxycodone hydrochloride and three of its metabolites after intravenous administration in Chinese patients with pain, Pharmacol. Rep. 66 (2014) 153–158.
[27] T.I. Saari, H. Ihmsen, P.J. Neuvonen, et al., Oxycodone clearance is markedly reduced with advancing age: a population pharmacokinetic study, Br. J. Anaesth. 108 (2012) 491–498.
[28] M. Neuvonen, P.J. Neuvonen, Determination of oxycodone, noroxycodone, oxymorphone, and noroxymorphone in human plasma by liquid chromatography-electrospray-tandem mass spectrometry, Ther. Drug Monit. 30 (2008) 333–340.
[29] W.B. Fang, M.R. Lofwall, S.L. Walsh, et al., Determination of oxycodone, noroxycodone and oxymorphone by high-performance liquid chromatography–electrospray ionization-tandem mass spectrometry in human matrices: in vivo and in vitro applications, J. Anal. Toxicol. 37 (2013) 337–344.
[30] A.R. Gammaitoni, M.W. Davis, Comparison of the pharmacokinetics of oxycodone administered in three Percocet formulations, J. Clin. Pharmacol. 42 (2002) 192–197.
[31] J. Hardy, R. Norris, H. Anderson, et al., Is saliva a valid substitute for plasma in pharmacokinetic studies of oxycodone and its metabolites in patients with cancer? Support. Care Cancer 20 (2012) 767–772.
[32] J. Malone, L. Hughes, An HPLC-MS/MS method for the determination of oxycodone, noroxycodone & oxymorphone in human plasma, Almac Sciences (2014), http://dx.doi.org/10.13140/RG.2.1.5059.0242.
[33] M. Dawson, B. Fryirs, T. Kelly, et al., A rapid and sensitive high-performance liquid chromatography-electrospray ionization-triple quadrupole mass spectrometry method for the quantitation of oxycodone in human plasma, J. Chromatogr. Sci. 40 (2002) 40–44.
[34] A.E. Olesen, R. Upton, D.J.R. Foster, et al., A pharmacokinetic and pharmacodynamic study of oral oxycodone in a human experimental pain model of hyperalgesia, Clin. Pharmacokinet. 49 (2010) 817–827.
[35] F. Gaudette, A. Sirhan-Daneau, M. St-Onge, et al., Development of a sensitive method for the determination of oxycodone and its major metabolites noroxycodone and oxymorphone in human plasma by liquid chromatography-tandem mass spectrometry, J. Chromatogr. B 1008 (2016) 174–180.
[36] M. Wagner, E. Bourgogne, E. Varesio, et al., Quantitation of polar analytes using column-switching: application to oxycodone and three metabolites in human plasma, J. Chromatogr. B 878 (2010) 637–644.
[37] F. Pantano, S. Brauneis, A. Forneris, et al., Determination of oxycodone and its major metabolites noroxycodone and oxymorphone by ultra-high-performance liquid chromatography tandem mass spectrometry in plasma and urine: application to real cases, Clin. Chem. Lab. Med. (2017), http://dx.doi.org/10.1515/cclm-2016-0990.

[38] T. Dahn, J. Gunn, S. Kriger, et al., Quantitation of morphine, codeine, hydrocodone, hydromorphone, oxycodone, oxymorphone, and 6-monoacetylmorphine (6-MAM) in urine, blood, serum, or plasma using liquid chromatography with tandem mass spectrometry detection, Methods Mol. Biol. 603 (2010) 411–422.
[39] X. Qiu, D. Lou, D. Su, et al., Simultaneous determination of acetaminophen and dihydrocodeine in human plasma by UPLC-MS/MS: its pharmacokinetic application, J. Chromatogr. B 992 (2015) 91–95.
[40] R. Coles, M.M. Kushnir, G.J. Nelson, et al., Simultaneous determination of codeine, morphine, hydrocodone, hydromorphone, oxycodone, and 6-acetylmorphine in urine, serum, plasma, whole blood, and meconium by LC-MS-MS, J. Anal. Toxicol. 31 (2007) 1–14.
[41] H.C. Atkinson, I. Stanescu, C. Frampton, et al., Pharmacokinetics and bioavailability of a fixed-dose combination of ibuprofen and paracetamol after intravenous and oral administration, Clin. Drug Investig. 35 (2015) 625–632.
[42] T. Zhu, L. Ding, X. Guo, et al., Simultaneous determination of tramadol and acetaminophen in human plasma by LC–ESI–MS, Chromatographia 66 (2007) 171–178.
[43] K. Devarakonda, T. Morton, R. Margulis, et al., Pharmacokinetics and bioavailability of oxycodone and acetaminophen following single-dose administration of MNK-795, a dual-layer biphasic IR/ER combination formulation, under fed and fasted conditions, Drug Des. Dev. Ther. 8 (2014) 1125–1134.
[44] Guidance for Industry, Bioanalytical Method Validation, U.S. Department of Health and Human Services, Food and Drug Administration Centre for Drug Evaluation and Research (CDER), Centre forVeterinary Medicine (CVM), May, 2001.

Journal of Pharmaceutical Analysis 8 (2018) 168–175

Contents lists available at ScienceDirect

Journal of Pharmaceutical Analysis

journal homepage: www.elsevier.com/locate/jpa
www.sciencedirect.com

Original Research Article

Evaluation of physicochemical properties as supporting information on quality control of raw materials and veterinary pharmaceutical formulations

Sara da Silva Anacleto [a], Marcella Matos Cordeiro Borges [a], Hanna Leijoto de Oliveira [a], Andressa Reis Vicente [b], Eduardo Costa de Figueiredo [c], Marcone Augusto Leal de Oliveira [d], Bárbara Juliana Pinheiro Borges [e], Marcelo Antonio de Oliveira [f], Warley de Souza Borges [b], Keyller Bastos Borges [a,*]

[a] Departamento de Ciências Naturais, Universidade Federal de São João del-Rei, Campus Dom Bosco, Praça Dom Helvécio 74, Fábricas, 36301-160 São João del-Rei, Minas Gerais, Brazil
[b] Departamento de Química, Universidade Federal do Espírito Santo, Avenida Fernando Ferrari, 514, Goiabeiras, 29075-910 Vitória, Espírito Santo, Brazil
[c] Laboratório de Análise de Toxicantes e Fármacos, Faculdade de Ciências Farmacêuticas, Universidade Federal de Alfenas, Rua Gabriel Monteiro da Silva 700, Centro, 37130-000 Alfenas, Minas Gerais, Brazil
[d] Departamento de Química, Universidade Federal de Juiz de Fora, Rua José Lourenço Kelmer, s/n, 36036-330 Juiz de Fora, Minas Gerais, Brazil
[e] Centro de Ciências da Saúde, Universidade Federal do Espírito Santo, Avenida Marechal Campos, 1468, Maruípe, 29.043-900 Vitóri, Espírito Santo, Brazil
[f] Centro Universitário Norte do Espírito Santo, Universidade Federal do Espírito Santo, Br 101 Norte, Km 67, São Mateus, Espírito Santo, Brazil

ARTICLE INFO

Article history:
Received 21 September 2017
Received in revised form
5 January 2018
Accepted 9 January 2018
Available online 17 January 2018

Keywords:
HPLC
Physicochemical characterization
Quality control
Veterinary pharmaceutical formulation
Raw material

ABSTRACT

This study aimed to show that the physicochemical proprieties obtained by Fourier transform infrared spectroscopy (FTIR), thermogravimetry (TG), and scanning electronic microscopy (SEM) can be useful tools for evaluating the quality of active pharmaceutical ingredients (APIs) and pharmaceutical products. In addition, a simple, sensitive, and efficient method employing HPLC-DAD was developed for simultaneous determination of lidocaine (LID), ciprofloxacin (CFX) and enrofloxacin (EFX) in raw materials and in veterinary pharmaceutical formulations. Compounds were separated using a Gemini C_{18} (250 mm × 4.6 mm, 5 μm) Phenomenex® column, at a temperature of 25 °C, with a mobile phase containing 10 mM of phosphoric acid (pH 3.29): acetonitrile (85.7:14.3, v/v) and a flow rate of 1.5 mL/min. Physicochemical characterization by TG, FTIR, and SEM of raw materials of LID, CFX, and EFX provided information useful for the evaluation, differentiation, and qualification of raw materials. Finally, the HPLC method was proved to be useful for evaluation of raw material and finished products, besides satisfying the need for an analytical method that allows simultaneous determination of EFX, CFX, and LID, which can also be extended to other matrices and applications.

1. Introduction

During the development of pharmaceutical products, it is crucial to know the physicochemical properties of drugs. Pharmaceutical laws oblige drug manufacturers to assess the compatibility of active substances, excipients, and medicinal products with established standards. However, characterization of the active pharmaceutical ingredients (APIs) improves the quality parameters of all raw materials used during the manufacturing process of pharmaceuticals, as well as those in the final products [1].

For adequate investigation of APIs, it is necessary to use appropriate instrumental analysis techniques, and recent reports have shown a high interest in the use of thermogravimetry analysis (TGA) [2,3], Fourier transform infrared spectroscopy (FTIR) [4,5], near-infrared spectroscopy [6], and Raman spectroscopy [7].

Fluoroquinolones are broad-spectrum antibiotics with potent activity against pathogens that have clinical relevance in human and veterinary medicine. They are mainly employed in prevention of and therapy for diseases such as infections of the urinary, gastrointestinal, and respiratory tract, sexually transmitted diseases, skin infections, and chronic osteomyelitis [8].

This class of agents is characterized by a favorable pharmacokinetic profile, high tissue penetration, and rapid bactericidal action. Currently, the most frequently used fluoroquinolone is enrofloxacin (EFX, Fig. S1). Its antimicrobial properties constitute

Peer review under responsibility of Xi'an Jiaotong University.
* Corresponding author.
E-mail address: keyller@ufsj.edu.br (K.B. Borges).

https://doi.org/10.1016/j.jpha.2018.01.001

an advantage for use in poultry, notably for treating mycoplasma infections, colibacillosis, and in animals on pastures. EFX is also used in aquaculture, both as a prophylactic and as a chemotherapeutic agent. In the aquatic environment, it is employed against common bacterial pathogens, namely *Yersinia ruckeri*, *Vibrio anguillarum*, *Renibacterium salmoninarum*, and *Aeromonas salmonicida*. There are reports that ciprofloxacin (CFX, Fig. S1), a primary metabolite of EFX, has a greater microbial efficacy [9]. In fact, CFX has become the first fluoroquinolone widely available since the second half of the 1980s. This drug is efficient against numerous gram-negative and gram-positive pathogens, and has been used for treating a variety of bacterial infections [10], both in humans and poultry. One of its disadvantages is the food-drug interaction with divalent and trivalent atoms, such as Ca^{2+} and Al^{3+}, respectively [11]. The oral absorption of CFX can be significantly reduced by concomitant administration of food containing milk, for example. Hence, CFX interaction with food may result in changes both in the rate and the extent of absorption and can potentially lead to sub-therapeutic concentrations of the drug and even treatment failure.

Lidocaine (LID, Fig. S1), the most commonly used local anesthetic, is also used as a diluent in injectable formulations. LID contributes to relieving pain related to surgical, dental, and gynecological procedures, both in humans and in animals, despite having no antimicrobial or antiparasitic activity [12]. Thus, it can be administered in association with other drugs, such as antiparasitics, anti-inflammatories, and antibiotics. For example, the use of LID in conjunction with fluoroquinolones has been reported previously: CFX for human prostate surgery [13] and EFX for surgical procedures in birds, for insertion of transmitters for the purpose of species migration research [14]. Therefore, the simultaneous analysis of LID, CFX, and EFX in pharmaceutical formulations and other matrices is highly desirable.

Several bioanalytical methods used for measuring concentrations of CFX have been reported, including capillary electrophoresis [15], spectrophotometry [16,17], high performance liquid chromatography (HPLC) with ultraviolet (UV) detection [18–23], and fluorescence detection [24–31]. Recently, HPLC methods coupled with mass spectrometry for the determination of CFX in human plasma have also been published. However, there have been few reports of methods for simultaneous determination of EFX and CFX, and mostly in biological fluids and animal tissue [32–41]. No method for simultaneous analysis of these compounds in raw materials and veterinary pharmaceutical formulations has been reported. In addition, many HPLC procedures for analysis of LID in pharmaceutical preparations and biological fluids have been published [42–44], as have the use of electrochemical methods for the direct quantification of LID and its impurities in pharmaceutical samples [42–46].

Hence, the objectives of this study were to: (i) show that FTIR, thermogravimetry (TG), and scanning electronic microscopy (SEM) can be useful for evaluation of the APIs (bulk drugs), i.e. LID, CFX, and EFX, supplied as raw materials; (ii) develop and validate an HPLC method for simultaneous determination of LID, CFX, and EFX in bulk drugs and veterinary pharmaceutical formulations; and (iii) apply this method in commercial tablets of EFX; and injectables of CFX and LID. Despite the existence of a wide range of studies for determining LID, CFX, and EFX, simultaneous determination of these drugs in raw materials and veterinary pharmaceutical formulations, aimed at application in quality control, are still lacking. Similarly, there is a lack of physicochemical studies of raw materials as a coadjutant in quality control described in literature. Finally, the availability of new methods with multidetection ability is very important, because this strategy can simplify the routine, improve the sensitivity and selectivity, and decrease operational costs.

2. Experimental

2.1. Standards and samples

All reference standards of LID, CFX, and EFX from United States Pharmacopeia (USP) were acquired from Sigma Aldrich® (St Louis, MO, USA). Samples of CFX and EFX as bulk drugs were obtained from Hebei Veyong (Shanghai, China) and LID was obtained from Henrifarma (São Paulo, SP, Brazil). Samples of finished product of Enrotrat® 200 mg (Ourofino®, Ribeirão Preto, SP, Brazil), Lidovet® injectable 2% (Bravet®, Rio de Janeiro, RJ, Brazil), and Ciprodez® injectable 10% (Biovet, Vargem Grande Paulista, SP, Brazil) were purchased from commercial sources in the local market.

2.2. Solvents and chemicals

Acetonitrile and methanol (HPLC grade) and triethylamine were obtained from J.T. Baker® (Mexico City, MX, Mexico). Water was distilled and purified using Millipore Milli-Q Plus system (Bedford, MA, USA). Analytical grade phosphoric acid (H_3PO_4, 85%) was purchased from Merck® (Darmstadt, Germany). All other chemicals were of analytical grade with the highest purity available.

2.3. Instruments for characterization of raw materials

Analysis by FTIR was carried out using Fourier Transform Spectrometer (Bomem Hartmann & Braun, MB series, Quebec, Canada), operating between 4000 and 400 cm^{-1}, with a resolution of 4 cm^{-1}, using the KBr pellet method. TGA was conducted in a termobalance (2950 Thermal Analysis Instrument, TA Instrument, New Castle, DE, USA) with a heating rate of 10 °C/min, under a flow rate of nitrogen at 50 mL/min, 25–600 °C. The SEM images were obtained at magnifications of 200 × and 500 × using a microscope TM3000 Hitachi Analytical Table Top (Tarrytown, NY, USA) with an acceleration of tension at 5 kV, employing carbon tape to fix raw materials in the carrier.

2.4. Instrument for chromatographic separation

The Agilent (Agilent Technologies, Palo Alto, CA, USA) chromatographic system used to develop and validate this method consisted of an Agilent LC 1260 quaternary pump (G1311 B), a thermostat, model 1290 (G1330B), an automatic injector, model 1260 Hip ALS (G1367E), a column oven, model 1290 TCC (G1316C), and a diode array detector (DAD), model 1260 VL^+ (G1315C). An Agilent OpenLAB Chromatography Data System® was used to control the HPLC system and was used for data acquisition. Separation was performed on a Gemini C_{18} column (250 mm × 4.6 mm, 5 μm) from Phenomenex® (Torrance, CA, USA). The analyses were performed at the Laboratório de Separações, Departamento de Ciências Naturais, Universidade Federal de São João del-Rei (UFSJ).

2.5. Analytical conditions

The mobile phase consisted of a mixture of 10 mM of phosphoric acid (pH 3.29):acetonitrile (85.7:14.3, v/v). UV detection was performed at 210 and 280 nm. All chromatographic procedures were conducted at 25 °C. A flow rate of 1.5 mL/min was used, and the injection volume was 10 μL for standards and samples.

2.6. Preparation of reference solutions and mobile phase

Working solutions of LID, CFX, and EFX used during the method validation step were prepared daily by diluting the stock solution with methanol to concentrations of 48, 52, 56, 60, 64, 68, and

72 μg/mL for CFX; 96, 104, 112, 120, 128, 136, and 144 μg/mL for EFX and 144, 156, 168, 180, 192, 204, and 216 μg/mL for LID.

The aqueous solution was prepared by diluting 2.5 mL concentrated phosphoric acid in 500 mL of purified water. The pH adjustment (pH 3.29) was performed with solutions of 1.0, 0.1, and 0.01 M triethylamine.

2.7. Validation of the method

The parameters were evaluated following the International Conference on Harmonization [47]. The method was validated for analysis of bulk drugs from Hebei Veyong® (CFX and EFX) and Henrifarma® (LID), and samples of finished products: Lidovet® injectable 2%, Ciprodez® injectable 10%, and Enrotrat® 200 mg tablets. The following parameters were studied: selectivity, linearity, limit of detection (LOD), limit of quantification (LOQ), precision, and accuracy.

Samples were fortified and analyzed to evaluate the selectivity of the method. The linearity of the assay method was determined by constructing three calibration graphs using seven concentration levels ranging from 80% to 120% of the assay analytes concentration of LID (144, 156, 168, 180, 192, 204, and 216 μg/mL), CFX (48, 52, 56, 60, 64, 68, and 72 μg/mL), and EFX (96, 104, 112, 120, 128, 136, and 144 μg/mL). Three replicate injections of the standard solutions were performed, and the peak areas of the chromatograms were plotted against the concentrations of analytes to obtain the respective calibration curves. The data were then subjected to regression analysis by the least-squares method in order to calculate the calibration model and correlation coefficient (r) value.

The LOD and LOQ values were calculated directly using the calibration curve. The LOD and LOQ were calculated from the slope and the standard deviation (SD) of the intercept of the mean of the three calibration curves determined by a linear regression model [47].

The precision of the method was determined by repeatability and intermediate precision studies. Repeatability was determined by analyzing samples at three different concentrations of LID (156, 180, and 204 μg/mL), CFX (52, 60, and 68 μg/mL), and EFX (104, 120, and 136 μg/mL) on the same day and under the same experimental conditions (intraday). The intermediate precision of the method was assessed by performing the analysis on two different days (interday). The accuracy was evaluated by applying the proposed method to the analysis of an in-house mixture of the placebo with known amounts of analytes. In order to carry out the test, the pharmaceutical solutions were prepared at the same concentration levels as precision test, and submitted for analysis under previously determined conditions so as to obtain the band areas of each reference chemical substance, at each concentration level. Precision and accuracy results obtained were expressed in terms of RSD (%) and relative error percentage (RE, %), respectively.

2.8. Pharmaceutical formulation and sample preparation

The Enrotrat® 200 mg tablet samples were milled using a mortar and pestle. Twenty tablets were weighed separately, triturated and dissolved in methanol and diluted to a concentration of 120 μg/mL for EFX analysis. The mixture was then sonicated for 10 min and allowed to rest for 10 min. The samples of Lidovet® injectable 2% and Ciprodez® injectable 10% were diluted with methanol at 60 and 180 μg/mL. All analyses were performed in real triplicates and filtered through a Millipore Millex nylon membrane with a 0.45 μm pore size (Merck, Darmstadt, Germany).

3. Results and discussion

There have been some reports of studies combining analytical techniques, such as thermogravimetry and spectroscopy in stability tests [48], polymorphism [49], and quality control of drugs [2,5,6,50–52]. Wesolowski et al. [5] evaluated the quality of 27 medicinal products and the composition of marketed pharmaceutical preparations using differential scanning calorimetry, FTIR, and Raman spectroscopy. In order to assess the utility of TG, FTIR and SEM as potential techniques for identification of the constituents of the raw materials, LID, CFX, and EFX were chosen, because methods for the simultaneous determination of these drugs in raw materials and veterinary pharmaceutical formulations are currently lacking. The results obtained by the physicochemical characterization of raw materials are represented by FTIR spectra (Fig. 1), TGA (Fig. 2), and images of morphological structures (Fig. 3).

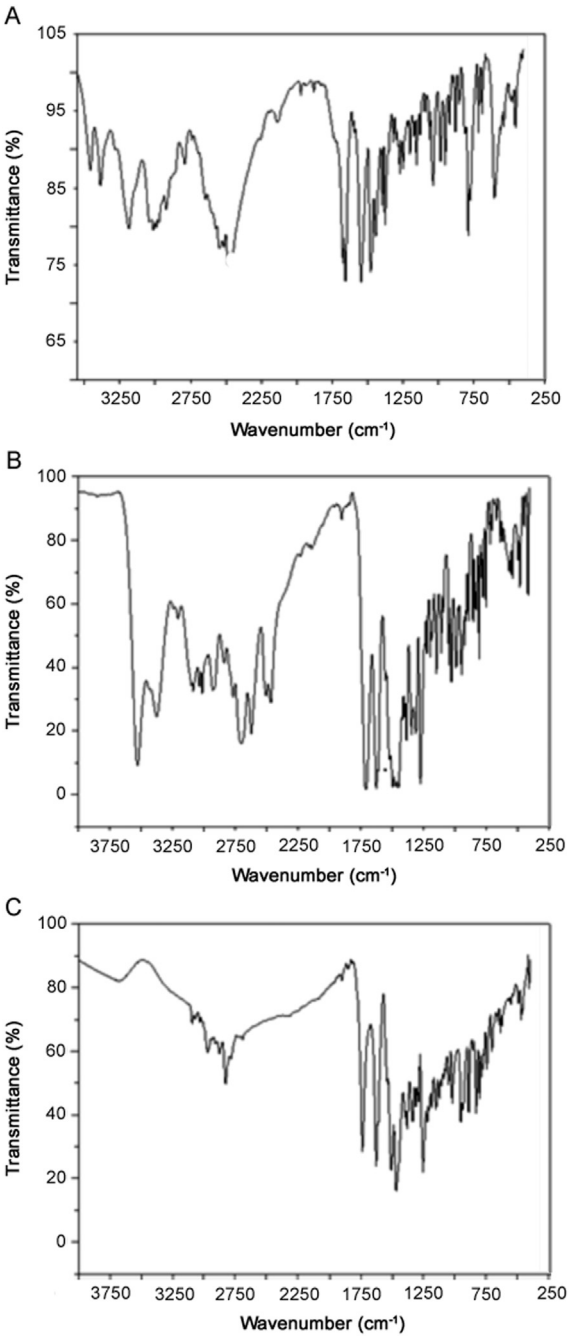

Fig. 1. FTIR spectra of (A) lidocaine (LID), (B) ciprofloxacin (CFX), and (C) enrofloxacin (EFX).

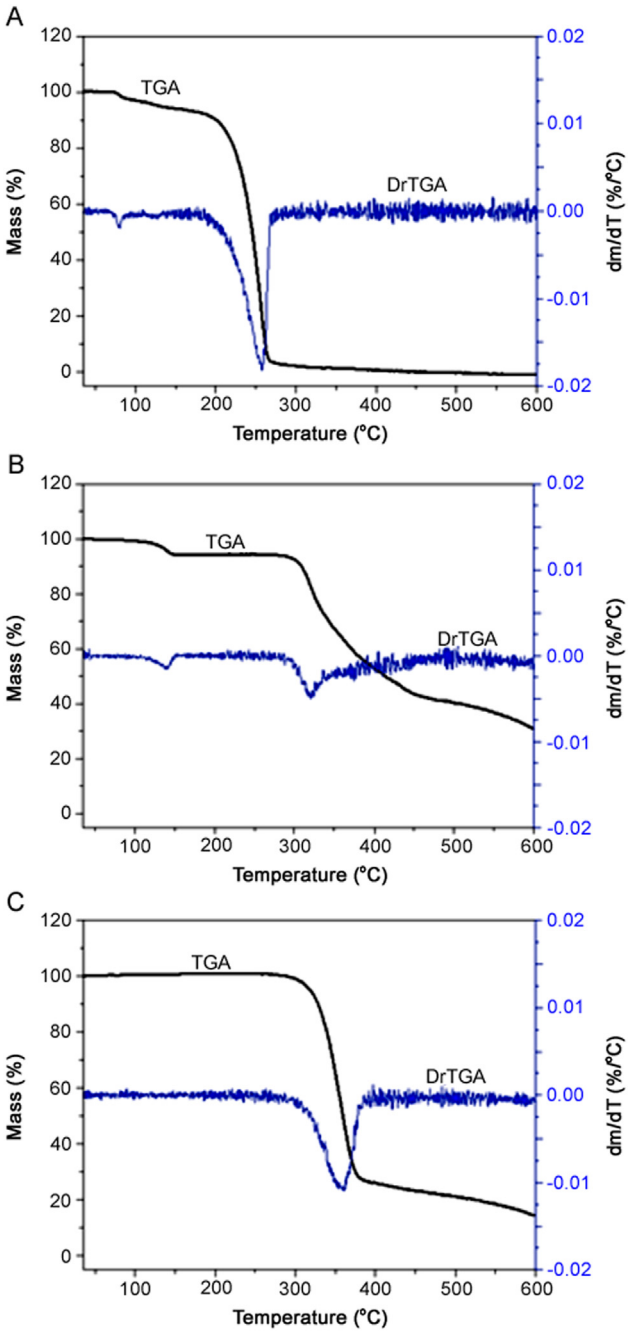

Fig. 2. Thermogravimetric curve (TGA) and derivative thermogravimetric curve (DrTGA) of (A) lidocaine (LID), (B) ciprofloxacin (CFX), and (C) enrofloxacin (EFX).

3.1. Characterization of CFX, EFX, and LID raw materials

3.1.1. FTIR

The FTIR spectra offered valuable information about the bulk pharmaceuticals (APIs). As can be seen in Fig. 1, the spectra of raw material were different, and can be used for identification of APIs from different suppliers. Fig. 1A presents the FTIR spectrum of LID: 3500 cm^{-1} (OH stretching and bonding intermolecular H), 3000 cm^{-1} (aromatic CH stretch and alkene), 1750 cm^{-1} (CO stretch acid group), 1600 cm^{-1} (NH bending present in quinolones), 1500 cm^{-1} (CO stretch carbonyl group), 1250 cm^{-1} (OH bending), and 1050 cm^{-1} (stretching the group CF). The FTIR spectrum of CFX shown in Fig. 1B presents the following as main bands: low intensity band at 3600 cm^{-1} (OH stretching), 3000 cm^{-1} (aromatic CH stretch and alkene), 1750 cm^{-1} (CO stretch acid group), 1600 cm^{-1} (NH bending present in quinolones), 1250 cm^{-1} (OH bending), and 1000 cm^{-1} (stretching the group CF). The FTIR spectrum presented in Fig. 1C for EFX demonstrates the following as main bands: 3400 cm^{-1} (stretch NH_2), 1650 cm^{-1} (stretching C=O primary amide), 1550 cm^{-1} (stretching C=C aromatic ring), 1480 and 1450 cm^{-1} (stretch C-N), and 800 cm^{-1} (flexing outside the aromatic ring plane).

3.1.2. TGA

TGA of LID, CFX, and EFX in nitrogen presented two, two, and one thermal decomposition stages, respectively. Fig. 2A shows two thermal events for LID. The first event (between 100 and 150 °C) exhibits a small mass loss (< 10%), due to evaporation of volatile compounds. The second event (approximately 300 °C) indicates the decomposition process of the drug, demonstrating rapid weight loss (around 55%). CFX presented two thermal events as can be seen in Fig. 2B. The first thermal event (up to 100 °C) has a small weight loss (< 10%) due to water evaporation. The second thermal event (approximately 350 °C) indicates the drug decomposition process, which causes a rapid weight loss (around 85%). The thermogram of Fig. 2C for EFX shows only a thermal event. In the single thermal event (about 350 °C), the drug decomposition process causes rapid weight loss (around 70%).

3.1.3. SEM

These figures were obtained at magnifications of 200 × and 500 × for each raw material. Figs. 3A and B show that LID has a morphological structure that is highly heterogeneous as it is possible to observe some larger, some smaller, and even some intermediate parts. It is also possible to observe that the LID particles are much larger than CFX and EFX particles. Figs. 3C and D show that the morphological structure of CFX is very homogeneous and takes the form of small needles, unlike the others compounds. Finally, in Figs. 3E and F the morphological structure of EFX is shown; it is heterogeneous and it is possible to observe some larger and other smaller parts. There is a large difference in the particle size of CFX and EFX.

3.2. HPLC method development

Due to the need for a method allowing simultaneous determination of CFX and EFX in the presence of the analgesic LID, we have developed and validated a reverse HPLC method. Analytical conditions were selected after testing the influence of different parameters, such as different columns, mobile phase composition, flow rate, temperature, and other chromatographic conditions. The chromatograms presented in Fig. S2 show that the increase in temperature caused loss of resolution and asymmetry. The optimized chromatographic conditions, such as mobile phase, column, wavelength, flow rate, injection volume, temperature and elution mode, are described in Table 1. Moreover, the chromatographic parameters, such as asymmetric factor, resolution, retention factor, separation factor, and theoretical plates, presented satisfactory results (Table 2). Fig. 4 shows typical chromatograms of LID, CFX, and EFX under optimized conditions at 210 and 280 nm, in which LID does not show absorbance at 210 nm.

In the present study, some validation parameters, such as selectivity, linearity, LOD, LOQ, precision, and accuracy, were evaluated. Tables 3 and 4 show that the results were satisfactory. The application of the developed method showed satisfactory results. In order to optimize the separation of all analytes, three HPLC columns: Gemini C_{18} column (250 mm × 4.6 mm, 5 μm) from Phenomenex®, Gemini C_8 column (250 mm × 4.6 mm, 5 μm) from Phenomenex®, and an Agilent Poroshcell 120 EC-C_{18} column (100 mm × 3.0 mm, 2.7 μm), and several mobile phase compositions (phosphoric acid and monopotassium phosphate buffer solutions at different pHs, and different acetonitrile and methanol percentages) were

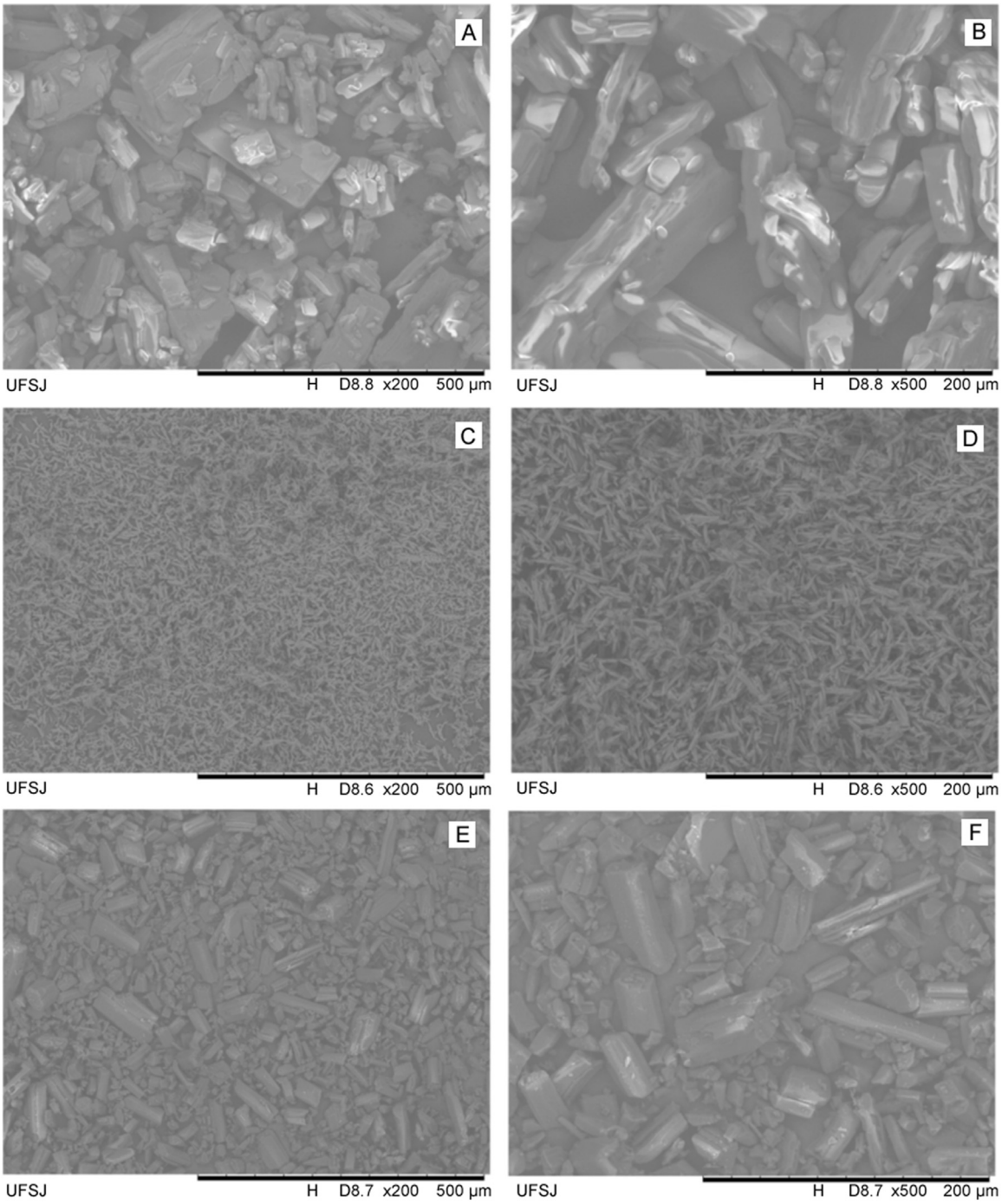

Fig. 3. Scanning electron microscopy (SEM) images of lidocaine (LID) at magnifications of 200 × (A) and 500 × (B), ciprofloxacin (CFX) at magnifications of 200 × (C) and 500 × (D), and enrofloxacin (EFX) at magnifications of 200 × (E) and 500 × (F).

Table 1
HPLC conditions for determination of lidocaine (LID), ciprofloxacin (CFX), and enrofloxacin (EFX) in raw material and pharmaceutical veterinary formulations.

Chromatographic variables	Optimized conditions
Mobile phase	10 mM phosphoric acid (pH 3.29) adjusted with triethylamine:acetonitrile (85.7:14.3, v/v)
Column	Gemini C_{18} Phenomenex® (250 mm × 4.6 mm i.d., 5 µm)
Wavelength	210 and 280 nm
Flow rate	1.5 mL/min
Injection volume	10 µL
Temperature	25 °C
Elution mode	Isocratic

Table 2
Chromatographic parameters for lidocaine (LID), ciprofloxacin (CFX), and enrofloxacin (EFX) under optimized conditions.

Analyte	Retention time (min)	*%RSD (peak area)*	*Af*	*Rs*	*k*	*α*	*N*
LID	6.49	1.2	0.84	–	2.26	–	4503
CFX	7.83	1.8	0.84	3.39	2.93	1.30	5925
EFX	11.26	1.4	0.79	6.35	4.66	1.59	4472

%RSD, relative standard deviation of all analyses expressed as a percentage; *Af*, asymmetric factor; *Rs*, resolution; *k*, retention factor (t_m = 1.99 min, defined as the first significant baseline disturbance, corresponding to the retention time of a non-retained solute); *α*, separation factor; *N*, theoretical plates.

Table 3
Linearity, limit of detection, and limit of quantification of the proposed method.

Parameters	LID	CFX	EFX
Linear equation[a]	y = 35,149x +3,000,000	y = 97,510x +430,183	y = 81,902x −67,213
Coefficient of correlation (*r*)	0.9960	0.9920	0.9910
Concentrations (μg/mL)	144–216	48–72	96–144
RSD (%)[b]	0.02	1.25	0.04
Shapiro-Wilk (normality test)[c], *p*-value	0.215	0.092	0.189
LOD (μg/mL)	15.17	0.91	11.13
LOQ (μg/mL)	50.55	3.04	37.09
RSD (%)[d]	0.62	3.81	2.47

[a] Calibration curves were performed in triplicate ($n = 3$) for each concentration, $y = ax + b$; where y is the peak area of analytes, a is the slope, b is the linear coefficient, and x is the concentration of the analyzed in μg/mL solution.
[b] RSD (%), relative standard deviation of the slope of the analytical curves.
[c] Normality test in residues: *p*-value higher than 0.05, indicating positive result to normality test within 95% confidence interval.
[d] RSD (%), relative standard deviation limit of quantitation.

evaluated. Experiments carried out using different mobile phases showed that the chromatographic signals corresponding to the three analytes were better resolved using the Gemini C_{18} column.

CFX and EFX are amphoteric, with pKa_1 values between 5.5 and 6.0 and pKa_2 between 7.7 and 8.5, respectively [53]. LID has a pKa value of 7.9 [54]. As they have functional ionisable groups, the pH of the mobile phase is a key factor in their separation. In this way, acid pH has been used to protonate the amino groups and the residual silanol groups of the stationary phase, in such a way that peak asymmetry could be reduced.

To achieve the best chromatographic separation of the analytes, different mixtures of methanol and/or acetonitrile with 10 mM of phosphoric acid with the pH adjusted between 3 and 5 with 1, 0.1, and 0.01 M triethylamine, were evaluated as the mobile phase. The tests showed that 10 mM of phosphoric acid (pH 3.29) provided a better separation, resulting in narrow and symmetrical peaks with good resolution. The analytical conditions were selected as adequate once all analytes showed baseline separation within 12 min. After careful evaluation of the electronic spectrum profile in the DAD system, the wavelength was set at 210 nm for LID and at 280 nm for CFX and EFX for quantitative analytical purposes. Therefore, a simple, rapid, low cost, and efficient HPLC method for separation of LID, CFX, and EFX was developed.

3.3. HPLC method validation

The calibration curves were prepared by plotting peak areas of LID, CFX, and EFX against the analyte concentrations, and they were linear in the range of 144–216 μg/mL, 48–72 μg/mL, and 96–144 μg/mL, respectively. Peak areas and concentrations were subjected to least-squares linear regression analysis to calculate the calibration equation and *r* value. All *r* values were ≥ 0.99, showing acceptable linearity for all analytes, since the normality test (Shapiro-Wilk) performed in residues presented no statistically significant result (*p*-value > 0.05). The developed method presented LOD and LOQ in the concentration range of μg/mL, which permitted correct determination of the concentration of the studied drugs. The LOD and LOQ were found to be between 0.91 and 15.17 and between 3.04 and 50.55 μg/mL, respectively, for all analytes. The precision and accuracy of the method were evaluated by calculating RSD% and RE%, respectively, for six determinations of CFX (52, 60, and 68 μg/mL), EFX (104, 120, and 136 μg/mL), and LID (156, 180, and 204 μg/mL) over the course of 2 days and under the same experimental conditions. Six replicates were carried out for each concentration ($n = 6$) in the intraday test. These results confirmed the precision and accuracy of the method within the desired range. The results were satisfactory, as all values were less than 3.0%. The validation procedure was repeated the next day in order to evaluate the efficiency of the method on different days (interday). All the studied compounds showed good results with low RE%.

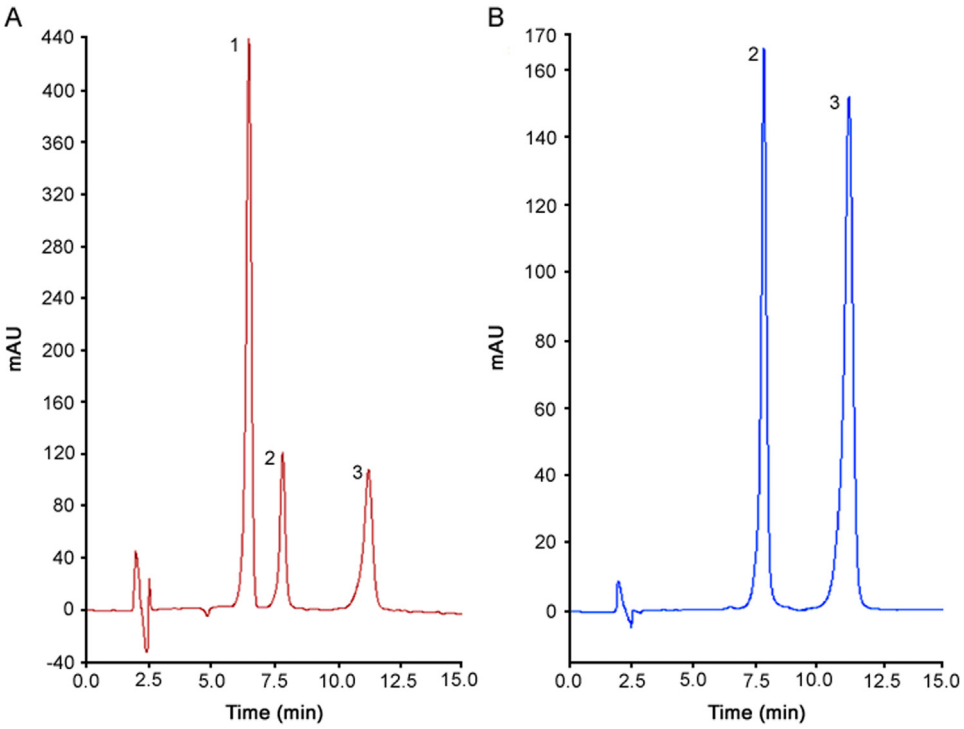

Fig. 4. Chromatogram referring to the optimized method for analysis of (1) Lidocaine (LID), (2) ciprofloxacin (CFX), and (3) enrofloxacin (EFX). Conditions: Gemini C_{18} (250 mm × 4.6 mm i.d., 5.0 μm) Phenomenex® column, mobile phase consisting of 10 mM of phosphoric acid (pH 3.29):acetonitrile (85.7: 14.3, v/v) at a flow rate of 1.5 mL/min, detection at 210 and 280 nm using a DAD, temperature at 25 °C, injection volume of 10 μL, and isocratic mode.

Table 4
Precision and accuracy for the simultaneous determination of lidocaine (LID), ciprofloxacin (CFX) and enrofloxacin (EFX).

Drug	Nominal conc. (μg/mL)	Intraday (n^a = 6)			Interday (n^d = 2)		
		Found conc. (μg/mL)	RSD (%)[b]	RE (%)[c]	Found conc. (μg/mL)	RSD (%)[b]	RE (%)[c]
LID	156.00	151.31	0.14	−3.00	152.58	1.16	−2.19
	180.00	178.63	0.22	−0.76	179.30	0.81	−0.39
	204.00	199.29	0.71	−2.31	201.14	0.98	−1.40
CFX	52.00	52.79	0.93	1.53	53.03	1.53	1.97
	60.00	59.51	1.82	−0.82	60.63	2.61	1.06
	68.00	67.30	1.62	−1.03	68.06	2.16	0.09
EFX	104.00	105.22	0.47	1.17	105.87	1.07	1.80
	120.00	117.34	0.71	−2.22	117.94	1.19	−1.72
	136.00	135.61	0.83	−0.29	135.39	−1.72	−0.45

[a] n = number of determinations.
[b] RSD (%), relative standard deviation in percentage.
[c] RE (%), relative error.
[d] n = number of days.

Table 5
Determination of lidocaine (LID), ciprofloxacin (CFX) and enrofloxacin (EFX) in bulk drugs and finished products.

Sample	Found conc. (μg/mL)	RSD (%)[a]	RE (%)[b]
Bulk drug			
LID	93.1		
	92.5	0.26	−0.22
	92.8		
CFX	84.90		
	83.90	0.62	−0.42
	85.10		
EFX	83.8		
	84.9	0.71	−0.43
	85.2		
Finished product			
LID	100.01		
	101.45	1.39	1.64
	103.45		
CFX	102.45		
	102.48	0.96	3.16
	104.56		
EFX	103.78		
	103.98	0.26	3.70
	103.34		

[a] RSD (%), relative standard deviation in percentage.
[b] RE (%), relative error.

3.4. Application of the method in drug bulk and finished products

The applicability of the proposed method was evaluated by determination of LID, CFX, and EFX in drug bulk and finished products, which were Enrotrat® 200 mg (Ourofino®, Ribeirão Preto, SP, Brazil), Lidovet® injectable 2% (Bravet®, Rio de Janeiro, RJ, Brazil), and Ciprodez® injectable 10%. All results are presented in Table 5. All analyses showed RSD (%) lower than 5%, which proves the efficiency of the developed method. In addition, bulk drugs showed values around 92.8% for LID and 84.6% for CFX and EFX. This approach allows testing of raw material and can help raw material suppliers to produce finished products with the correct dosage and to adjust the dosage appropriately. Finally, all finished products that were analyzed are in accordance with their specifications.

4. Conclusions

The physicochemical proprieties obtained by FTIR, TGA, and SEM for LID, CFX, and EFX raw materials showed the presence of bands that are characteristic of the presence of the organic groups that comprise their molecular structures, a significance difference in the thermal events related to mass loss, and large differences between their morphological structures, respectively. These findings are useful for the evaluation, differentiation and quality assurance of raw materials. In this study, a HPLC-DAD method has been developed that allows simultaneous determination of raw materials and veterinary pharmaceutical formulations containing LID, CFX, and EFX. This method was proved to be simple, rapid, low cost, and efficient. The obtained results were considered satisfactory since the baseline separation for all analytes occurred in less than 12 min under isocratic conditions. Temperature and pH conditions can markedly influence the elution of analytes during the optimization process. The method developed was proved to be useful for evaluation of raw materials and finished products, in addition to providing an analytical method for simultaneous determination of EFX, CFX, and LID, which can also be extended to other matrices and applications.

Conflicts of interest

The authors declare that there are no conflicts of interest.

Acknowledgments

The authors would like to thank the Brazilian agencies CNPq (Conselho Nacional de Desenvolvimento Científico e Tecnológico), CAPES (Coordenação de Aperfeiçoamento de Pessoal de Nível Superior), FAPES (Fundação de Amparo à Pesquisa e Inovação do Espírito Santo) and FAPEMIG (Fundação de Amparo à Pesquisa do Estado de Minas Gerais) for financial support. This work is a collaborative research project with members of Rede Mineira de Química (RQ-MG) supported by FAPEMIG (Project: REDE-113/10; Project: CEX - RED-0010–14).

Appendix A. Supplementary material

Supplementary data associated with this article can be found in the online version at doi:10.1016/j.jpha.2018.01.001.

References

[1] ICH, International Conference on Harmonization of Technical Requirements for Registration of Pharmaceuticals for Human Use, ⟨http://www.ich.org/home.htlm⟩ (Accessed 16 September 2016).
[2] A.P.B. Gomes, L.P. Correia, M.O. da Silva Simoes, et al., Development of thermogravimetric method for quantitative determination of ketoconazole, J. Therm. Anal. Calorim. 91 (2008) 317–321.
[3] M. Lappalainen, M. Karppinen, Techniques of differential scanning calorimetry for quantification of low contents of amorphous phases, J. Therm. Anal. Calorim. 102 (2010) 171–180.
[4] C. Tanase, L. Odochian, N. Apostolescu, TG-FTIR analysis applied to the study of thermal behaviour of some edible mushrooms, J. Therm. Anal. Calorim. 103 (2011) 1079–1085.
[5] M. Wesolowski, P. Szynkaruk, E. Makurat, DSC and IR as supporting tools for identification of methylxanthines in solid dosage forms of drugs, J. Therm. Anal. Calorim. 109 (2012) 807–815.
[6] G.J. Vergote, Ch Vervaet, J.P. Remon, et al., Near-infrared FT-Raman spectroscopy as a rapid analytical tool for the determination of diltiazem hydrochloride in tablets, Eur. J. Pharm. Sci. 16 (2002) 63–67.
[7] Y. Roggo, K. Degardin, P. Margot, Identification of pharmaceutical tablets by Raman spectroscopy and chemometrics, Talanta 81 (2010) 988–995.
[8] P.C. Appelbaum, P.A. Hunter, The fluoroquinolone antibacterials: past, present and future perspectives, Int. J. Antimicrob. Agents 16 (2000) 5–15.
[9] N. Gorla, E. Chiostri, L. Ugnia, et al., HPLC residues of enrofloxacin and ciprofloxacin in eggs of laying hens, Int. J. Antimicrob. Agents 8 (1997) 253–256.

[10] D.A. Talan, K.G. Naber, J. Palou, et al., Extended-release ciprofloxacin (Cipro XR) for treatment of urinary tract infections, Int. J. Antimicrob. Agents 23 (Suppl.) (2004) S54–S66.
[11] K. Pápai, M. Budai, K. Ludányi, et al., In vitro food–drug interaction study: which milk component has a decreasing effect on the bioavailability of ciprofloxacin? J. Pharm. Biomed. Anal. 52 (2010) 37–42.
[12] D. Smith, Determination and temperature effects of lidocaine (Lignocaine) hydrochloride, epinephrine, methylparaben, 2,6-dimethylaniline, and p-hydroxybenzoic acid in USP Lidocaine Injection by ion-pair reversed-phase high pressure liquid chromatography, J. Chromatogr. Sci. 19 (1981) 253–258.
[13] D.E. Leocádio, T.L. Frenkl, B.S. Stein, Office based transurethral needle ablation of the prostate with analgesia and local anesthesia, J. Urol. 178 (2007) 2052–2054.
[14] J.-P.L. Savard, L. Lesage, S.G. Gilliland, et al., Molting, staging, and wintering locations of common eiders breeding in the Gyrfalcon Archipelago, Ungava Bay, Arctic 64 (2011) 197–206.
[15] M.I. Pascual-Reguera, G.P. Parras, A.M. Díaz, Solid-phase UV spectrophotometric method for determination of ciprofloxacin, Microchem. J. 77 (2004) 79–84.
[16] K.H. Bannefeld, H. Stass, G. Blaschke, Capillary electrophoresis with laser-induced fluorescence detection, an adequate alternative to high-performance liquid chromatography, for the determination of ciprofloxacin and its metabolite desethyleneciprofloxacin in human plasma, J. Chromatogr. B 692 (1997) 453–459.
[17] S. Mostafa, M. El-Sadek, E.A. Alla, Spectrophotometric determination of ciprofloxacin, enrofloxacin and pefloxacin through charge transfer complex formation, J. Pharm. Biomed. Anal. 27 (2002) 133–142.
[18] L. Pou-Clave, F. Campos-Barreda, C. Pascual-Mostaza, Determination of ciprofloxacin in human serum by liquid chromatography, J. Chromatogr. B 563 (1991) 211–215.
[19] G. Mack, Improved high-performance liquid chromatographic determination of ciprofloxacin and its metabolites in human specimens, J. Chromatogr. B 582 (1992) 263–267.
[20] G.J. Krol, G.W. Beck, T. Benham, HPLC analysis of ciprofloxacin and ciprofloxacin metabolites in body fluids, J. Pharm. Biomed. Anal. 14 (1995) 181–190.
[21] M.T. Maya, N.J. Gonçalves, N.B. Silva, et al., Simple high-performance liquid chromatographic assay for the determination of ciprofloxacin in human plasma with ultraviolet detection, J. Chromatrogr. B 755 (2001) 305–309.
[22] R.M. Pellegrino, F. Segonoli, C. Cagini, Simultaneous determination of ciprofloxacin and the active metabolite of prulifloxacin in aqueous human humor by high-performance liquid chromatography, J. Pharm. Biomed. Anal. 47 (2008) 567–574.
[23] S. Watabe, Y. Yokoyama, K. Nakazawa, et al., Simultaneous measurement of pazufloxacin, ciprofloxacin, and levofloxacin in human serum by high-performance liquid chromatography with fluorescence detection, J. Chromatogr. B 878 (2010) 1555–1561.
[24] S. Zhai, M.R. Korrapati, X. Wei, et al., Simultaneous determination of theophylline, enoxacin and ciprofloxacin in human plasma and saliva by high-performance liquid chromatography, J. Chromatogr. B 669 (1995) 372–376.
[25] B.B. Ba, D. Ducint, M. Fourtillan, et al., Fully automated high-performance liquid chromatography of ciprofloxacin with direct injection of plasma and Mueller–Hinton broth for pharmacokinetic/pharmacodynamic studies, J. Chromatogr. B 714 (1998) 317–324.
[26] H. Scholl, K. Schmidt, B. Weber, Sensitive and selective determination of picogram amounts of ciprofloxacin and its metabolites in biological samples using high-performance liquid chromatography and photothermal post-column derivatization, J. Chromatogr. 416 (1987) 321–330.
[27] A. Misuno, T. Uematsu, M. Nakashima, Simultaneous determination of ofloxacin, norfloxacin and ciprofloxacin in human hair by high-performance liquid chromatography and fluorescence detection, J. Chromatogr. B 653 (1994) 187–193.
[28] A. Zotou, N. Miltiadou, Sensitive LC determination of ciprofloxacin in pharmaceutical preparations and biological fluids with fluorescence detection, J. Pharm. Biomed. Anal. 28 (2002) 559–568.
[29] S. Imre, M.T. Dogaru, C.E. Vari, et al., Validation of an HPLC method for the determination of ciprofloxacin in human plasma, J. Pharm. Biomed. Anal. 33 (2003) 125–130.
[30] O.R. Idowu, J.O. Peggins, Simple, rapid determination of enrofloxacin and ciprofloxacin in bovine milk and plasma by high-performance liquid chromatography with fluorescence detection, J. Pharm. Biomed. Anal. 35 (2004) 143–153.
[31] Z. Bybíralová, M. Nobilis, J. Zoulova, et al., High-performance liquid chromatographic determination of ciprofloxacin in plasma samples, J. Pharm. Biomed. Anal. 37 (2005) 851–858.
[32] K.L. Tyczkowska, K.M. Hedeen, D.P. Aucoin, et al., High-performance liquid chromatographic method for the simultaneous determination of enrofloxacin and its primary metabolite ciprofloxacin in canine serum and prostatic tissue, J. Chromatogr. 493 (1989) 337–346.
[33] V. Hormazabal, A. Rogstad, I. Steffenak, et al., Rapid assay for monitoring residues of enrofloxacin and sarafloxacin in fish tissues by high performance liquid chromatography, J. Liq. Chromatogr. 14 (1991) 1605–1614.
[34] K. Flammer, D.P. Aucoin, D.A. Whitt, Intramuscular and oral disposition of enrofloxacin in African grey parrots following single and multiple doses, J. Vet. Pharmacol. Ther. 14 (1991) 359–366.
[35] J.A. Tarbin, D.J. Tyler, G. Shearer, Analysis of enrofloxacin and its metabolite ciprofloxacin in bovine and porcine muscle by high-performance liquid chromatography following cation exchange clean-up, Food Addit. Contam. 9 (1992) 345–350.
[36] M. Horie, K. Saito, N. Nose, et al., Simultaneous determination of benofloxacin, danofloxacin, enrofloxacin and ofloxacin in chicken tissues by high-performance liquid chromatography, J. Chromatogr. B 653 (1994) 69–76.
[37] K.L. Tyczkowska, R.D. Voyksner, K.L. Anderson, et al., Simultaneous determination of enrofloxacin and its primary metabolite ciprofloxacin in bovine milk and plasma by ion-pairing liquid chromatography, J. Chromatogr. B 658 (1994) 341–348.
[38] G. Carlucci, Analysis of fluoroquinolones in biological fluids by high-performance liquid chromatography, J. Chromatogr. A 812 (1998) 343–367.
[39] L. Escuder-Gilabert, S. Sagrado, R.M. Villanueva-Camafiasand, et al., Analysis of pharmaceutical preparations containing local anesthetics by micellar liquid chromatography and spectrophotometric detection, Chromatographia 49 (1999) 85–90.
[40] J. Manceau, M. Gicquel, M. Laurentine, et al., Simultaneous determination of enrofloxacin and ciprofloxacin in animal biological fluids by high-performance liquid chromatography: application in pharmacokinetic studies in pig and rabbit, J. Chromatogr. B 726 (1999) 175–184.
[41] A. Posyniak, J. Zmudzki, S. Semeniuk, et al., Determination of fluoroquinolone residues in animal tissues by liquid chromatography, Biomed. Chromatogr. 13 (1999) 279–285.
[42] Z. Fijałek, E. Baczynski, A. Piwońska, et al., Determination of local anaesthetics and their impurities in pharmaceutical preparations using HPLC method with amperometric detection, J. Pharm. Biomed. Anal. 37 (2005) 913–918.
[43] M.A.A. Mohammad, LC determination of lidocaine and prilocaine containing potential risky impurities and application to pharmaceuticals, Chromatographia 70 (2009) 563–568.
[44] M. Abdel-Rehim, M. Bielenstein, Y. Askemark, et al., High-performance liquid chromatography–tandem electrospray mass spectrometry for the determination of lidocaine and its metabolites in human plasma and urine, J. Chromatogr. B 741 (2000) 175–188.
[45] British Pharmacopoeia, Medicines and Healthcare Products Regulatory Agency, London, UK, 2011.
[46] European Pharmacopoeia, European Directorate for the Quality of Medicines & Healthcare (EDQM), Strasbourg, France, 2011.
[47] International Conference on Harmonization (ICH), Validation of Analytical Procedures: Methodology, Technical Requirements for the Registration of Pharmaceuticals for Human Use, Geneva, Switzerland, 1996.
[48] S.Y. Lin, S.L. Wang, Advances in simultaneous DSC–FTIR microspectroscopy for rapid solid-state chemical stability studies: some dipeptide drugs as examples, Adv. Drug Deliv. Rev. 64 (2012) 461–478.
[49] S.Y. Lin, An overview of famotidine polymorphs: solid-state characteristics, thermodynamics, polymorphic transformation and quality control, Pharm. Res. 31 (2014) 1619–1631.
[50] L.C.S. Cides, A.A.S. Araújo, M. Santos-Filho, et al., Thermal behaviour, compatibility study and decomposition kinetics of glimepiride under isothermal and non-isothermal conditions, J. Therm. Anal. Calorim. 84 (2006) 441–445.
[51] F.A. Aguiar, C.M. de Gaitani, K.B. Borges, Capillary electrophoresis method for the determination of isradipine enantiomers: stability studies and pharmaceutical formulation analysis, Electrophoresis 32 (2011) 2673–2682.
[52] F.A. de S. Ribeiro, C.R.T. Tarley, K.B. Borges, et al., Development of a square wave voltammetric method for dopamine determination using a biosensor based on multiwall carbon nanotubes paste and crude extract of *Cucurbita pepo* L, Sens. Actuators B Chem. 185 (2013) 743–754.
[53] J. Barbosa, D. Barron, J. Cano, et al., Evaluation of electrophoretic method versus chromatographic, potentiometric and absorptiometric methodologies for determining pKa values of quinolones in hydroorganic mixtures, J. Pharm. Biomed. Anal. 24 (2001) 1087–1098.
[54] H.A. McLure, A.P. Rubin, Review of local anaesthetic agents, Minerva. Anestesiol. 71 (2005) 59–74.

Journal of Pharmaceutical Analysis 8 (2018) 176–180

Contents lists available at ScienceDirect

Journal of Pharmaceutical Analysis

journal homepage: www.elsevier.com/locate/jpa
www.sciencedirect.com

Original Research Article

Identification of three kinds of *Plumeria* flowers by DNA barcoding and HPLC specific chromatogram

Leilei Zhao [a,b], Xiaoxue Yu [a,b], Jie Shen [a,b], Xinjun Xu [a,b,*]

[a] School of Pharmaceutical Sciences, Sun Yat-sen University, Guangzhou 510006, China
[b] Guangdong Technology Research Center for Advanced Chinese Medicine, Guangzhou, China

ARTICLE INFO

Article history:
Received 14 September 2017
Received in revised form
28 January 2018
Accepted 8 February 2018
Available online 9 February 2018

Keywords:
Plumeria
DNA barcoding
HPLC specific chromatogram
Chemometrics analysis
Identification

ABSTRACT

DNA barcoding and HPLC specific chromatogram were used to identify three kinds of *Plumeria* flowers respectively. DNAs extracted from the three *Plumeria* species were amplified by PCR with universal primers, and the *psb*A-*trn*H region was selected. All the amplified products were sequenced and the results were analyzed by MEGA 5.0. Chemometric methods including principal components analysis and hierarchical clustering analysis were conducted on the SAS 9.0 software to demonstrate the variability among samples. In conclusion, the *psb*A-*trn*H of all samples were successfully amplified from total DNA and sequenced. These three varieties of *Plumeria* can be differentiated by the *psb*A-*trn*H region and clustered into three groups respectively through building neighbor joining tree, which conformed to their germplasm origins. However, it was hard to distinguish them by HPLC specific chromatograms combined with chemometrics analysis. These indicated that DNA barcoding was a promising and reliable tool for the identification of three kinds of *Plumeria* flowers compared to HPLC specific chromatogram generally used. It could be treated as a powerful complementary method for traditional authentication, especially for those varieties which are difficult to be identified by conventional chromatography.

1. Introduction

Plumeria is a kind of deciduous tree belonging to Apocynaceae. It has a significant medicinal value and can be used for the treatment of various ailments, such as sore throat, heatstroke, belly-ache, cough, and dysentery [1]. The main chemical components of *Plumeria* are iridoids, triterpenes, flavonoids, essential oil and so on. Mansour et al. [2] found that the iridoids in *Plumeria* have a toxic effect on a series human tumor cells. The extracts of the flowers can significantly inhibit streptococcus faecalis, bacillus, and corynebacterium pyogenes [3]. Gupta et al. [4] indicated that the flowers extracts of *Plumeria* had the antipyretic-analgesic effect. As a medicine with dual-purpose of drug and food, the flowers of *Plumeria* are also popular among people in making herbal tea to relieve the summer heat.

There are many varieties of *Plumeria*, such as *Plumeria rubra* L., *Plumeria rubra* var. *alba*, and *Plumeria rubra* 'Acutifolia'. Some researches have indicated that the chemical components vary from different *Plumeria* flowers, some of which may have good bioactivities [5–8]. However, it is difficult to identify *Plumeria* flowers because they are very alike after dried and processed. Thus, authenticity assurance is crucial for their quality control. We intended to use DNA barcoding technique and HPLC specific chromatograms to identify three kinds of *Plumeria*.

DNA barcoding is a technique for identifying biological specimens using short DNA sequences from either nuclear or organelle genomes [9]. This technique has three advantages as follows. Firstly, the results have good repeatability compared to other molecular identification methods. Secondly, DNA barcoding technique is highly universal. The traditional taxonomic method requires that the leaves, flowers, fruits and other organs of plants must exist. However, DNA barcoding technique is not limited by growth stage, organ, tissue difference or the external environment. And a small number of samples are enough for the identification. Lastly, it can establish a unified database and identification platform to realize digital species identification [10]. DNA barcoding technique has been applied to identification of animals, gymnosperms, angiosperms, fungi and so on [11].

The chloroplast DNA (cpDNA) has been commonly used for DNA barcoding studies in plants. The cpDNA contains variable DNA regions, among which the most commonly used cpDNA intergenic spacer is *psb*A-*trn*H, which has shown high variability and can be used to elucidate genetic relationships at the intraspecific level [12,13]. In this pioneering study, we selected *psb*A-*trn*H to identify three varietas of *Plumeria*, at the same time, the HPLC specific

Peer review under responsibility of Xi'an Jiaotong University.
* Corresponding author at: School of Pharmaceutical Sciences, Sun Yat-sen University, Guangzhou 510006, China.
E-mail address: xxj2702@sina.com (X. Xu).

https://doi.org/10.1016/j.jpha.2018.02.002

chromatogram that is commonly used for identification was also used for distinguishing these three varieties of *Plumeria* to make comparison. We hope that our established method will be helpful for the future quality control of *Plumeria* flowers.

2. Experimental

2.1. Materials and reagents

Twelve samples of *Plumeria* flowers were collected from three districts in Guangzhou, Guangdong, China (Table 1). They were authenticated by Associate Professor Lin Jiang, Sun Yat-Sen University, China. Methanol was of analytical grade and manufactured by Tianjin Zhiyuan Chemical Reagent Factory (Tianjin, China). TAE buffer, agarose, PVP-40 and *Taq* PCR Master Mix (2 ×, blue dye) were purchased from Sangon Biotech (Shanghai, China). DNA secure Plant Kit was purchased from Tiangen Biotech (Beijing, China). Goldview (MYM Biological Technology Co., Ltd., USA) was used for agarose examination. Acetonitrile was of HPLC grade manufactured by SK Chemicals (Korea). Ultrapure water was obtained from a Milli-QRG purification unit (Millipore, Bedford, MA, USA).

2.2. Apparatus

An electronic balance (KERN ABT 220-5DM, 0.1 mg, Germany), an ultrasonic machine (SB25-12DTD, Xinzhi Biotechnical Ltd., Ningbo, China) and an eppendorf centrifuge 5417R (Eppendorf AG, Hamburg, Germany) were used for sample preparation and DNA extraction. PCR amplification was performed on the K960 thermal cycler (Hangzhou Jingge Scientific Instrument Co., Ltd, Hangzhou, China). HPLC analysis was performed on the Shimadzu LC-15C high performance liquid chromatograph (Shimadzu, Japan) with a Dikma Diamonsil C_{18} column (250 mm × 4.6 mm, 5 μm; Dikma, Beijing, China) and a guard column (15 mm × 4.6 mm, 5 μm; Dikma, Beijing, China).

2.3. Sample pre-treatment for DNA extraction and total DNA extraction

The fresh flowers were washed up and wiped with 75% alcohol aqueous. About 100 mg of each sample was grinded with 1% (m/m) PVP-40. Then, DNA secure Plant Kit was used for total DNA extraction. The process followed the instruction of the Kit.

2.4. PCR amplification and DNA sequencing

DNA barcodes were amplified by polymerase chain reaction using universal primers (fwd: 5′-GTTATGCATGAACGTAATGCTC-3′ and rev: 5′-CGCGCATGGATTCACAATCC-3′). Each 25 μL reaction mixture contained 12.5 μL *Taq* PCR Master Mix, 1 μL Genomic DNA, 1 μL of each 10 μM primer, 1 μL $MgCl_2$ solution and 8.5 μL ddH_2O The PCR conditions for amplification were 1 cycle 94 °C for 5 min; 40 cycles of 94 °C 30 s, 56 °C 30 s, 72 °C 45 s; and 1 cycle 72 °C for 10 min, and hold 4 °C. To detect amplified products successfully, PCR products were examined on 2% agarose gels stained with Goldview and visualized under ultraviolet light.

2.5. Sequence alignment and analysis

All the amplified products were sent to Sangon Guangzhou for sequencing. The sequences were analyzed by MEGA 5.0.

2.6. Preparation of sample solution for HPLC analysis

Test solutions were prepared by extracting 0.5 g dried and pulverized herbs with 10 mL 70% methanol aqueous under ultrasonic condition at room temperature for 30 min. After cooling, the extracted solution was added with 70% methanol aqueous to the original weight. The extracts were filtered through a 0.45 μm filter before used for HPLC analysis.

2.7. HPLC conditions

Chromatographic separation was carried out on a Diamonsil C_{18} column along with a guard column. The separation was conducted at 35 °C with a flow rate of 0.7 mL/min. 0.5% acetic acid aqueous solution (A) and acetonitrile (B) were used as the mobile phase in gradient elution mode. The elution gradient was set as follows: 0–10 min, 10% (B); 10–30 min, 10%→15% (B); 30–70 min, 15%→20% (B); 70–85 min, 20%→65% (B); 85–90 min, 65%→90% (B); 90–95 min, 90% (B). The detection wavelength was 240 nm. The injection volume was 20 μL.

2.8. Chemometric analysis

Principal components analysis (PCA) and hierarchical clustering analysis (HCA) were conducted on the SAS 9.0 software to demonstrate the variability among the 12 samples.

3. Results and discussion

3.1. DNA barcode result analysis

Authenticity assurance is crucial for quality control of natural products. It is essential to develop different approaches to authenticate the natural products as each approach has advantages that complementary to one another [14]. A desirable DNA barcode

Table 1
Information of the collected sample.

Samples	Latin name	District
R1	*Plumeria rubra* L.	Sun Yat-Sen University campus · Panyu · Guangzhou
R2	*Plumeria rubra* L.	Sun Yat-Sen University campus · Panyu · Guangzhou
R3	*Plumeria rubra* L.	Sun Yat-Sen University campus · Panyu · Guangzhou
R4	*Plumeria rubra* L.	Sun Yat-Sen University campus · Panyu · Guangzhou
P1	*Plumeria rubra* var. *alba*	Sun Yat-Sen University campus · Panyu · Guangzhou
P2	*Plumeria rubra* var. *alba*	Liwan-Lake Park · Liwan · Guangzhou
P3	*Plumeria rubra* var. *alba*	Tianhe Park · Tianhe · Guangzhou
P4	*Plumeria rubra* var. *alba*	Tianhe Park· Tianhe · Guangzhou
W1	*Plumeria rubra* 'Acutifolia'	Sun Yat-Sen University campus · Panyu · Guangzhou
W2	*Plumeria rubra* 'Acutifolia'	Sun Yat-Sen University campus · Panyu · Guangzhou
W3	*Plumeria rubra* 'Acutifolia'	Sun Yat-Sen University campus · Panyu · Guangzhou
W4	*Plumeria rubra* 'Acutifolia'	Sun Yat-Sen University campus · Panyu · Guangzhou

Table 2
Properties of the *psb*A-*trn*H region of the 12 samples.

Samples	Length (bp)	GC content (%)	Variable sites																				
			1	1	1	1	1	2	2	2	2	3	3	3	3	3	4	4	4	4	4	4	4
			2	2	2	2	3	1	3	4	5	1	4	6	7	7	0	2	5	7	7	9	9
			0	7	8	9	0	6	8	5	2	6	2	5	0	5	8	7	5	1	7	0	7
R1	518	27.99	A	–	–	T	A	T	G	G	C	G	T	G	G	G	G	G	G	G	T	T	T
R2	540	28.52	A	–	–	T	A	T	G	G	C	G	T	G	G	G	G	G	G	G	T	T	T
R3	540	28.52	A	–	–	T	A	T	G	G	C	G	T	G	G	G	G	G	G	G	T	T	T
R4	543	29.10	A	–	–	T	A	T	G	G	C	G	T	G	G	G	G	G	G	G	T	T	T
P1	545	28.62	A	T	T	–	A	T	G	G	A	T	T	G	G	C	G	G	G	G	T	T	T
P2	533	27.95	A	T	T	–	A	T	G	G	A	T	T	G	G	C	G	G	G	G	T	T	T
P3	543	27.81	A	T	T	–	A	T	G	G	A	T	T	G	G	C	G	G	G	G	T	T	T
P4	528	27.46	A	T	T	–	A	T	G	G	A	T	T	G	G	C	G	G	G	G	T	T	T
W1	530	28.49	T	T	T	T	T	G	A	A	C	T	G	A	A	G	A	A	G	C	G	G	G
W2	541	28.65	T	T	T	T	T	G	A	A	C	T	G	A	A	G	A	A	G	C	G	G	T
W3	538	27.51	T	T	T	T	T	G	A	A	C	T	G	A	A	G	A	A	A	C	G	G	T
W4	540	27.96	T	T	T	T	T	G	A	A	C	T	G	A	A	G	A	A	A	C	G	G	G

* Numbers above the variable sites are their positions in the multiple sequence alignment. R1-R4: *Plumeria rubra* L., P1-P4: *Plumeria rubra* var. *alba*, and W1-W4: *Plumeria rubra* 'Acutifolia'.

should process high interspecific divergences and low intraspecific variations. The Consortium for the Barcode of Life (CBOL) suggested comparing the interspecies distance (d_{inter}) and intraspecies distance (d_{intra}) to estimate the identification effectiveness of the selected barcode. The interspecific divergences of an ideal 'barcoding gap' should be significantly larger than intraspecific divergences. If d_{inter}/d_{intra} is smaller than 1, it may not be a suitable DNA barcode [10].

The results of DNA barcoding showed a good differentiation. The *psb*A-*trn*H of all samples were successfully amplified from total DNA and sequenced. Properties of the *psb*A-*trn*H region are summarized in Table 2. The genetic distance was calculated by MEGA 5.0, based on Kimura-2-parameter model. The intraspecies distances of *Plumeria rubra* L. and *Plumeria rubra* 'Acutifolia' were 0.001 and 0.004, respectively. There was no intraspecies distance for *Plumeria rubra* var. *alba*. The interspecies distance was 0.007 between *Plumeria rubra* L. and *Plumeria rubra* var. *alba*, 0.034 between *Plumeria rubra* L. and *Plumeria rubra* 'Acutifolia', 0.033 between *Plumeria rubra* var. *alba* and *Plumeria rubra* 'Acutifolia'. Results of each d_{inter}/d_{intra} were larger than 1, which indicated that the *psb*A-*trn*H region was suitable for the identification of three varietas of *Plumeria*. The neighbor joining tree was built by MEGA 5.0 by repeated 1000 times bootstrap (Fig. 1). The neighbor joining tree showed that the samples of *Plumeria rubra* L., *Plumeria rubra* var. *alba* and *Plumeria rubra* 'Acutifolia' can be clustered into three groups, respectively. Therefore, the *psb*A-*trn*H region was an appropriate DNA barcode for identifying these three varietas of *Plumeria*.

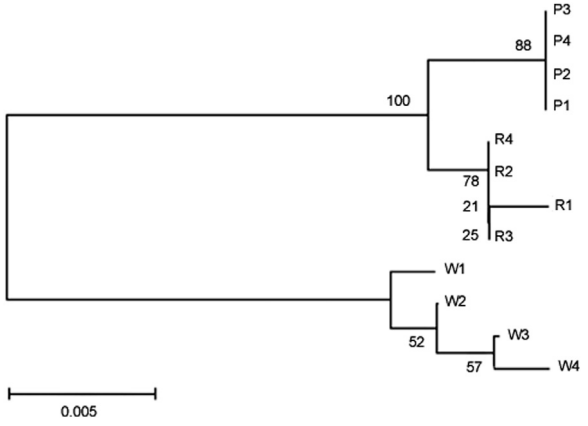

Fig. 1. The neighbor joining tree of *Plumeria rubra* L. (R1-R4), *Plumeria rubra* var. *alba* (P1-P4) and *Plumeria rubra* (W1-W4) 'Acutifolia' based on the *psb*A-*trn*H sequence with K2P model.

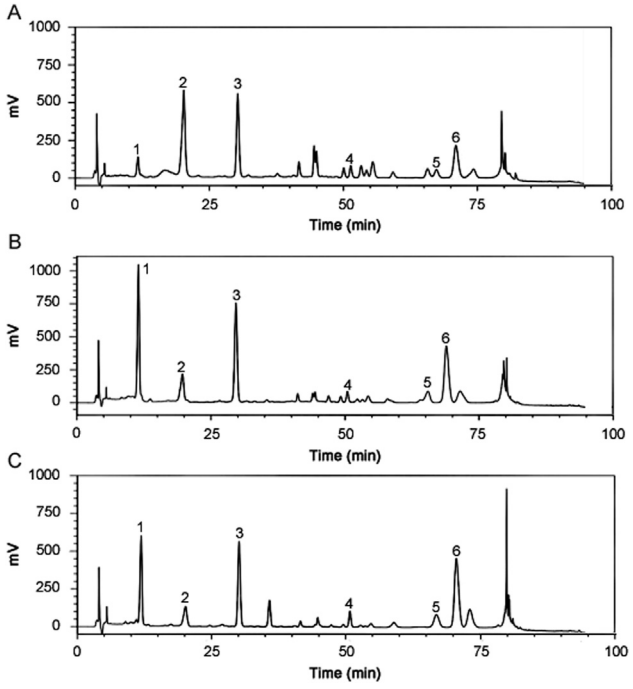

Fig. 2. The liquid chromatograms of the three *Plumeria* (A: *Plumeria rubra* L., B: *Plumeria rubra* var. *alba*, C: *Plumeria rubra* 'Acutifolia').

3.2. HPLC analysis

Fig. 2 shows the HPLC specific chromatograms of samples R1 (*Plumeria rubra* L.), P1 (*Plumeria rubra* var. *alba)* and W1 (*Plumeria rubra* 'Acutifolia'), their HPLC chromatograms were so similar that it was difficult to separate the three varietas visually.

3.3. Principal component analysis (PCA)

PCA, a multivariate analysis technique, could visualize similarities or differences within multivariate data [15]. It was employed to analyze the differences among these 12 samples. The peak areas of 6 characteristic peaks were set as variables, while 12 samples were set as observations. PC1 explained 41.2% of the total variance in the data set while PC2 explained 32.4%. The cumulative

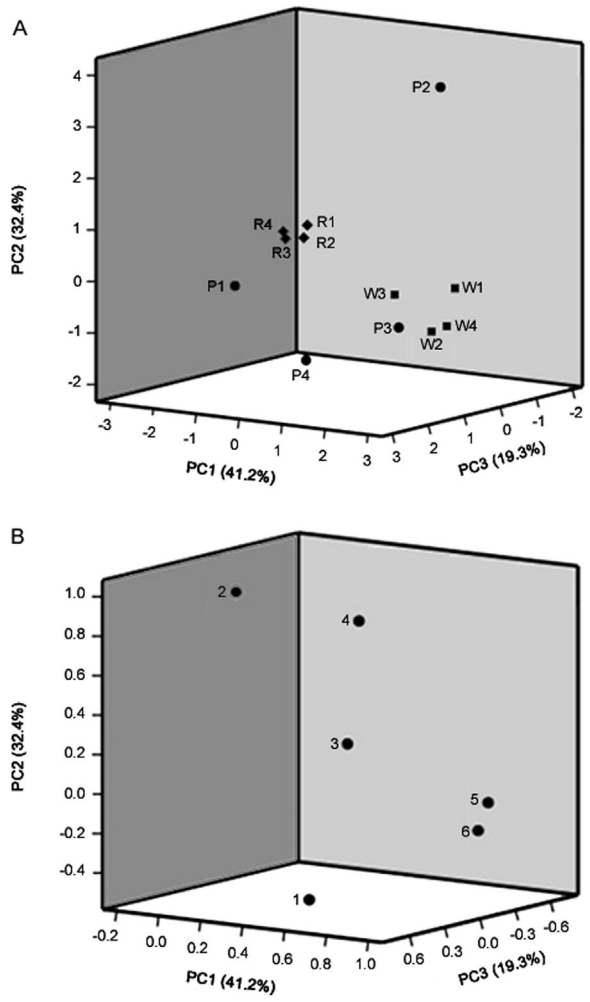

Fig. 3. Score plot (A) and loading plot (B) of PCA.

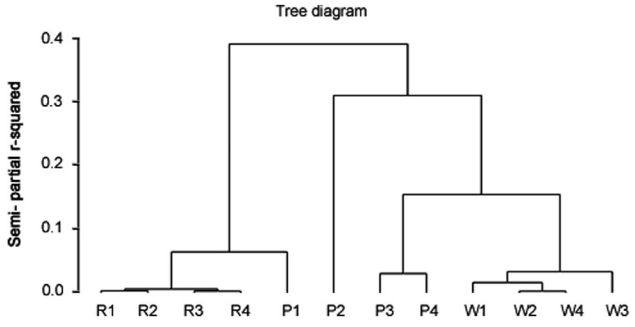

Fig. 4. The dendrogram of 12 batches of *Plumeria* by HCA. R1-R4: *Plumeria rubra* L., P1-P4: *Plumeria rubra* var. *alba*, and W1-W4: Plumeria rubra 'Acutifolia'.

proportion of PCA as well as the loading diagram is shown in Fig. 3. According to the loading diagram, PC1 showed a strong correlation with peak 5 and peak 6. PC2 showed a strong correlation with peak 2 and peak 4. PC3 showed a strong correlation with peak1 and peak 5. The distinguished results of HPLC specific chromatograms combined with PCA were not as accurate as that of DNA barcoding.

3.4. Hierarchical cluster analysis (HCA)

HCA, one of the most commonly used unsupervised pattern recognition methods, is a useful multivariate statistic technique to assign a data set into groups by creating a cluster tree or dendrogram according to similarity [15]. In order to assess the resemblance and differences of these samples, HCA of *Plumeria* samples was performed based on the peak area of the 6 characteristic chromatographic peaks by SAS 9.0 software. The Ward's method was applied as the amalgamation rule and the squared Euclidean distance was selected to measure the resemblance and classify the 12 samples. The result is shown in Fig. 4. Samples R1–R4 (*Plumeria rubra* L.) were categorized into one cluster, W1–W4 (*Plumeria rubra* 'Acutifolia') were categorized into another cluster. However, samples P1–P4 (*Plumeria rubra* var. *alba)* cannot cluster together. Samples R1–R4 and W1–W4 were collected from the same district, but samples P1–P4 were from three different districts. Therefore, we speculated that the environment affected the chemical component which affected the result of PCA and HCA.

4. Conclusion

This study has shown that DNA barcoding combined with chemometrics analysis can distinguish *Plumeria rubra* L., *Plumeria rubra* 'Acutifolia' and *Plumeria rubra* var. *alba.* while the HPLC method can not identify these three varietas because the specific chromatograms were similar. DNA barcoding technique is hopeful for automation as it is more stable, accurate and not affected by growth stage, tissue difference or external environment. This technique is an effective supplement for traditional authentication methods, especially when different species are mixed together. This work also provides an experimental reference for identification of natural medicines by DNA barcoding technique.

Conflicts of interest

The authors declare that there are no conflicts of interest.

Acknowledgments

This work was supported by the Industry-University-Research Cooperation Program from Science and Technology Department of Guangdong Province (No.: 2013B090600058); the National Key Research and Development Program of China (2017YFC170116).

References

[1] Chinese Herbal Medicines Guangxi Standard, 1st volume, The Guangxi Zhuang Autonomous Region Health Department, Guangxi Science and Technology Press, Nanning, 1990: 59.
[2] A.K. Mansour, M.M. Eid, N.S.A.M. Khalil, Synthesis and reactions of some new heterocyclic carbohydrazides and related compounds as potential anticancer agents, Molecules 8 (2003) 744–755.
[3] P.A. Egwaikhide, S.O. Okeniyi, C.E. Gimba, Screening for anti-microbial activity and phytochemical constituents of some Nigerian medicinal plants, J. Med. Plants Res. 3 (2009) 1088–1091.
[4] M. Gupta, U.K. Mazumder, P. Gomathi, Evaluation of antipyretic and anti-nociceptive activities of *Plumeria* acuminata leaves, J. Med. Sci. 7 (2007) 452–456.
[5] Z. Zahee, A.G. Konale, K.A. Patel, et al., Comparative phytochemical screening of flowers of *Plumeria alba* and *Pulmeria rubra*, Asian J. Pharm. Clin. Res. 3 (2010) 88–89.
[6] N. Tohar, M.A. Mohd, I. Jantan, et al., A comparative study of the essential oils of the genus *Plumeria* Linn. from Malaysia, Flavour Fragr. J. 6 (2006) 304–309.

[7] N. Tohar, K. Awang, M.A. Mohd, et al., Chemical composition of the essential oils of four Plumeria specials grown on Peninsular Malayasia, J. Essent. Oil Res. 6 (2006) 613–617.
[8] Y.Q. Liu, H.W. Wang, S. Wei, et al., Chemical composition and antimicrobial activity of the essential oils extracted by microwave-assisted hydrodistillation from the flowers of two Plumeria species, Anal. Lett. 45 (2012) 2389–2397.
[9] N. Techen, I. Parveen, Z.Q. Pan, et al., DNA barcoding of medicinal plant material for identification, Curr. Opin. Biotechnol. 25 (2014) 103–110.
[10] S.L. Chen, DNA Barcoding Molecular Markers in Chinese Medicinal Materials, People's Medical Publishing House, Beijing, 2012: 18-19.
[11] S.L. Chen, Y. Hui, J.P. Han, et al., Validation of the ITS2 region as a novel DNA barcode for identifying medicinal plant species, PLoS One 5 (2010) e8613.
[12] H. Azum, J.G. García-Franco, V. Rico-Gray, et al., Molecular phylogeny of the Magnoliaceae: the biogeography of tropical and temperate disjunctions, Am. J. Bot. 88 (2001) 2275–2285.
[13] M.B. Hamilton, J.M. Braverman, D.F. Soria-Hernanz, Patterns and relative rates of nucleotide and insertion/deletion evolution at six chloroplast intergenic regions in new world species of the Lecythidaceae, Mol. Biol. Evol. 20 (2003) 1710–1721.
[14] P.C. Shaw, J. Wang, P.P.H. But, Authentication of Chinese Medicinal Materials by DNA Technology, World Scientific, Singapore, 2002: 1–23.
[15] Z.S. Xie, S.Z. Lam, J.W. Wu, et al., Chemical fingerprint and simultaneous determination of flavonoids in Flos Sophorae Immaturus by HPLC-DAD and HPLC-DAD-ESI-MS/MS combined with chemometrics analysis, Anal. Methods 6 (2014) 4328–4335.

Journal of Pharmaceutical Analysis 8 (2018) 181–186

Contents lists available at ScienceDirect

Journal of Pharmaceutical Analysis

journal homepage: www.elsevier.com/locate/jpa
www.sciencedirect.com

Original Research Article

Enhancing the dissolution of phenylbutazone using Syloid® based mesoporous silicas for oral equine applications

Laura J. Waters [a,*], John P. Hanrahan [b], Joseph M. Tobin [b], Catherine V. Finch [a], Gareth M.B. Parkes [a], Shamsuddeen A. Ahmad [a], Faraj Mohammad [a], Maria Saleem [a]

[a] School of Applied Sciences, University of Huddersfield, Queensgate, Huddersfield HD1 3DH, UK
[b] Glantreo Ltd, ERI Building, Lee Road, Cork City T23 XE10, Ireland

ARTICLE INFO

Article history:
Received 21 November 2017
Received in revised form
23 January 2018
Accepted 24 January 2018
Available online 31 January 2018

Keywords:
Dissolution
Syloid® silicas
Drug-loading
Phenylbutazone
Solubility

ABSTRACT

Three mesoporous silica excipients (Syloid® silicas AL-1 FP, XDP 3050 and XDP 3150) were formulated with a model drug known for its poor aqueous solubility, namely phenylbutazone, in an attempt to enhance the extent and rate of drug dissolution. Although other forms of mesoporous silica have been investigated in previous studies, the effect of inclusion with these specific Syloid® silica based excipients and more interestingly, with phenylbutazone, is unknown. This work reports a significant enhancement for both the extent and rate of drug release for all three forms of Syloid® silica at a 1:1 drug:silica ratio over a period of 30 min. An explanation for this increase was determined to be conversion to the amorphous form and an enhanced drug loading ability within the pores. Differences between the release profiles of the three silicas were concluded to be a consequence of the physicochemical differences between the three forms. Overall, this study confirms that Syloid® silica based excipients can be used to enhance dissolution, and potentially therefore bioavailability, for compounds with poor aqueous solubility such as phenylbutazone. In addition, it has been confirmed that drug release can be carefully tailored based on the choice of Syloid® silica and desired release profile.

1. Introduction

Mesoporous silica has been shown to exhibit a great potential to aid in the formulation of pharmaceutical compounds with poor aqueous solubility, as reviewed by Choudhari et al. [1]. As a drug carrier system, mesoporous silica can accommodate drugs that have been introduced through organic solvent immersion, incipient wetness impregnation or melted in [2]. Specific advantages of using excipients such as mesoporous silicas are their nanoporous structures, high surface areas, clinical safety and large pore volumes [3]. Current opinion is that substantial progress has been made in recent years in the characterisation and development of mesoporous drug delivery systems although more work is needed regarding dissolution enhancement potential and related physicochemical properties [4]. There are several reasons for this need to continue exploring the possible use of mesoporous silica such as practical considerations such as manufacturability to large scale quantities (e.g. tonne) and regulation, as well as physicochemical considerations such as the possibility of re-adsorption onto the silica surface [4]. Adsorption of small drug particles on the surface of large excipients has been a successful strategy for low-dose drugs, poorly water soluble drugs, targeted drug release [5], sustained drug delivery [6] and stability enhancement. This is mainly a result of improving the dissolution profile by increasing drug surface area or transformation of the drug from a crystalline to amorphous form [7], and its ability to be retained within the silica pores [8]. In many cases, the method of formulation can be critical in defining the properties of the resultant formulation. For example, silica-based drug delivery vehicles have been investigated to avoid hydrolisation of the active compound using supercritical CO_2 [9,10], a formulation method known for its high drug-loading ability [11] amongst other advantages [12]. Several other formulation methods have also been attempted, for example, to create liquid (also known as liquisolid) formulations [13] and pediatric (solvent free) formulations [14]. The work within our group that has previously confirmed the application of microwave irradiation for mesoporous silicas [15]. Furthermore, there is clearly an interest in developing mesoporous silica formulations as evidenced by recent work to predict in vivo performance, for example, using in silico techniques [16], to overcome multidrug resistance [17] as well as to ameliorate toxic side effects [18].

One particular category of mesoporous silicas where only very limited studies have been conducted to date is regarding Syloid®

Peer review under responsibility of Xi'an Jiaotong University.
* Corresponding author.
E-mail address: l.waters@hud.ac.uk (L.J. Waters).

https://doi.org/10.1016/j.jpha.2018.01.004

silica based formulations. These forms of silica have a highly developed network of mesopores that provide access to the large surface area, i.e. a combination of a high adsorption capacity, along with a desirable pore size and surface morphology. For these reasons, these silicas tend to be used to improve the flow properties of pharmaceuticals where liquid ingredients can be converted into free-flowing powders. Although these properties are beneficial, their suitability to enhance dissolution has only briefly been considered (by publication) for two forms of Syloid® silica (244 and AL-1) with two model drugs, namely, indomethacin [19] and itraconazole [20]. Interestingly, for both compounds, an enhancement in the rate and extent of dissolution was observed in both studies. Yet surprisingly, other forms of Syloid® silica have not yet been considered even though they may provide a plethora of advantages for drug-loading formulations.

One specific drug renowned for having poor aqueous solubility: 0.05 mg/mL [21], and therefore problematic dissolution with potentially low bioavailability, is phenylbutazone. This particular compound is commonly used in equine environments as a non-steroidal anti-inflammatory drug (NSAID) [22,23], often prescribed for pain control [24,25]. Although drug solubility is significantly greater in ethanol and 1-octanol [26], the low level of aqueous solubility results in complications for formulators. One study has successfully enhanced the dissolution through the creation of a solid dispersion with polyethylene glycol 8000 [27] and another with SBA-15 [28], yet there is still a clear need for developing alternative formulations that can achieve an even greater enhancement in release of the active compound. Phenylbutazone is an excellent candidate for exploring the potential to enhance solubility through formulation with a dissolution-limiting low solubility yet incredibly significant usage within the equine community. This is because many of the present formulations available on the market tend to be unfavourable with issues surrounding drug delivery and poor palatability [29]. Thus ways to enhance phenylbutazone-based formulations are highly desirable.

This work investigates the suitability of using three types of Syloid® silica based excipients to quantify their potential to enhance the rate of dissolution of phenylbutazone and determine the causes of any enhancements observed.

2. Materials and methods

2.1. Materials

Phenylbutazone, potassium phosphate dibasic, and potassium phosphate monobasic (all $\geq$ 99%) were purchased from Sigma Aldrich (Dorset, UK) and used as received. Syloid® silicas (AL-1 FP, XDP 3050 and XDP 3150) were kindly donated by Glantreo Ltd, Cork, Ireland and W. R. Grace & Co, Maryland, USA. Table 1 provides a summary of the physicochemical properties of the Syloid® silicas, and the data presented were determined using nitrogen gas sorption isotherms. These were measured at 77 K using a Micromeritics TriStar II surface area analyzer (Micromeritics, Norcross, GA, USA). Samples were pre-treated by heating at 200 °C under nitrogen for 12 h. The surface area was measured using the Brunauer-Emmett-Teller (BET) method. The pore volume and pore diameter data was calculated using the Barrett, Joyner and Halenda (BJH) method [2]. Specific surface areas were calculated from the measured relative pressure in the range of $P/P_0 = 0.01$ to $P/P_0 = 0.3$. Mesoporous volumes were estimated from the volume of nitrogen adsorbed after the micropores have been filled until after condensation into the mesopores was complete. Of particular interest is the range of surface areas and pore volumes exhibited by the three Syloid® silicas as based on previous research, such properties may influence dissolution. For example, pore size has been known to effect drug release profiles for other mesoporous systems [30].

Table 1
The physicochemical properties of the Syloid® silicas used in this study.

Name	Mean particle size (μm)	Shape	Surface area (m^2/g)	Pore volume (cm^3/g)	Pore diameter (Å)
AL-1 FP	10	Irregular	605	0.23	26
XDP 3050	50	Irregular	287	1.69	229
XDP 3150	110	Irregular	320	1.70	200

2.2. Methods

2.2.1. Formulation methods

200 mg of Syloid® silica XDP 3050 was placed in a beaker whereupon 40 mL of deionised water was gradually added, followed by 200 mg of phenylbutazone to achieve a total drug and silica mass of 400 mg. Over a period of 60 min the solution was stirred and heated to a maximum of 90 °C, cooled to room temperature, vacuum filtered and dried overnight at 60 °C, and then sieved to remove agglomerates larger than 250 μm. This process was repeated in triplicate and then with the replacement of XDP 3050 with XDP 3150 and AL-1 FP to produce a total of three unique drug-Syloid® silica formulations. A series of variable ratios of drug: Syloid drug:Syloid® silica formulations were also formulated but based on dissolution profile data (not shown), no significant differences in release profiles were observed between the formulations; thus this paper only presents formulations at a 1:1 ratio. A final formulation was produced that involved phenylbutazone undergoing the formulation process (but without the presence of Syloid® silica) to determine if it was the processing that affected dissolution or the presence of each Syloid® silica itself. Water was used as a 'carrier' to disperse the drug within the mixture, rather than dissolving the drug with organic solvent, followed by heating to help achieve maximum dispersion within the mixture.

2.2.2. Characterisation methods

Powder X-ray diffraction (XRD) data were collected on a Bruker D_2-Phaser equipped with a Cu $K\alpha_1$ radiation source at 30 kV and 10 mA current. Particle size distribution of the formulated products was analysed using a Malvern Mastersizer 2000 (Worcestershire, UK) using 5–10 mg of powder per sample with one drop of surfactant (IGEPAL® CA-630) at a stirring speed of 2000 rpm. Triplicate data was subsequently analysed using Mastersizer 2000 software (V5.61). Drug loading was verified to be 100% in all formulated samples by UV analysis of the filtrates ($\lambda = 282$ nm) with no residual drug detected ($< 1\%$), thus confirming all of the drug remained within the formulation (rather than washed away with the filtrate during the formulation process). For stability confirmation the infrared spectrum for the pure samples and their formulations was recorded using a Nicolet-380 Fourier Transform Infrared spectrometer (FT-IR) with an ATR crystal. Powder samples were placed directly onto the diamond crystal and the anvil was lowered to ensure that sample was in full contact with the diamond. Each spectrum was obtained in the range of 500–4000 cm^{-1} with 2 cm^{-1} resolution. In this study, the morphology of the prepared samples was characterised using scanning electron microscopy (SEM) (JEOL JSM-6060LV, Japan) with gold-plating using a sputter coater (SC7620) prior to imaging.

2.2.3. In vitro phenylbutazone release

Dissolution profiles were determined using a USP Type II (paddle method) PharmaTest DT70 system, with manual sampling

for a period of 30 min. Formulated samples with a total drug content of 22.5 mg were placed in 900 mL of pH 7.0 phosphate buffer, stirred at 75 rpm and maintained at 37.0 ± 0.5 °C, maintaining sink conditions throughout the duration of the experiment. Filtered samples were removed every 5 min, replaced with phosphate buffer, and analysed using UV spectroscopy (Cary 60, Agilent) set at a wavelength (λ) of 282 nm with conversion to percentage drug release using a standard calibration plot. Samples were analysed in triplicate to determine mean drug release percentages and associated error limits.

3. Results and discussion

3.1. Characterisation of formulations

XRD patterns for samples of the three mesoporous silicas both with and without the presence of phenylbutazone are shown in Fig. 1. Previous XRD studies using naproxen noted that the diminishment of peak intensities confirmed that the drug had loaded into channels of a mesoporous material [31], resulting in an amorphous formulation with an absence of characteristic peaks [15]. A similar result was observed in this work whereby the purely crystalline phenylbutazone that could be seen in Fig. 1A (and after processing in Fig. 1B) was converted to the amorphous form following formulation with the three Syloid® silicas (Figs. 1C-E). As discussed earlier, from analysing the filtrates and confirming all of the drug had remained within the formulation, the absence of peaks cannot be explained by a reduced concentration of drug and can only be explained by a transformation to the amorphous form.

Particle size analysis confirmed that phenylbutazone (prior to formulation) exhibited an average particle sizes of 65–70 μm. The sizes of the three Syloid® silicas prior to formulation are presented in Table 1 and were confirmed in this study to have average values of 10, 50 and 110 μm for AL-1 FP, XDP 3050 and XDP 3150, respectively. These three Syloid® silicas display an interesting range of particle sizes prior to formulation. Yet their subsequent dissolution profiles may actually be more dependent upon their size after formulation (through the formation of aggregates); therefore, it is this parameter that is of interest in this work. Firstly, AL-1 FP displayed an increase in the average particle size and a slightly broader distribution of sizes with the majority of particles between 5 and 100 μm after formulation. Secondly, a similar result was seen for XDP 3050 with the majority of particles between 40 and 100 μm. An explanation for this increase in size and diversity of sizes for both Syloid® silicas is most likely a consequence of particle agglomeration as a result of drug incorporation and/or processing effects. Thirdly, Syloid® silica 3150 did not exhibit any significant increase in average particle size following formulation although there was an increase in the polydispersity of particle size. Again, this indicates agglomeration may have occurred to a limited extent but not to the same degree as that seen for the other Syloid® silicas.

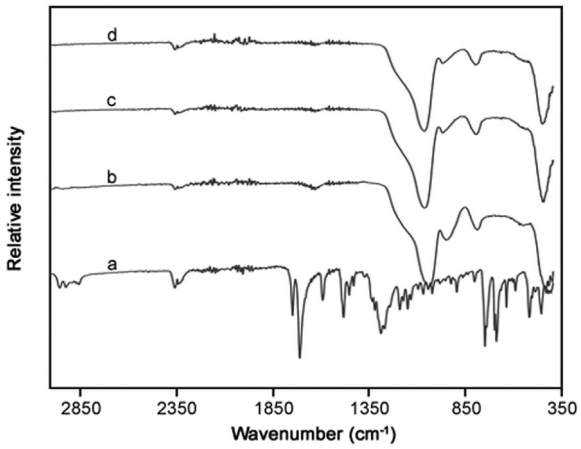

Fig. 2. FT-IR analysis of (a) phenylbutazone, (b) AL-1 FP, (c) XDP 3150, and (d) XDP 3050 silicas prior to formulation.

FT-IR spectroscopy was used to monitor the presence of phenylbutazone and determine interactions with the three silicas (Figs. 2 and 3). Analysis of spectra for phenylbutazone showed the expected absorption bands at wavenumbers (with corresponding functional groups) of 754 and 1483 cm^{-1} (C-H), 1270 cm^{-1} (C-N) and 1720 cm^{-1} (C=O). Analysis of the spectra for phenylbutazone subjected to the processing method did not reveal any changes in the specific absorption bands for the drug, suggesting a lack of degradation as a result of the formulation process. The three Syloid® silicas were analysed using FT-IR spectroscopy and all displayed the expected intense Si-O absorption band at 1060–1070 cm^{-1} [32]. For the three phenylbutazone-silica formulated products, the results indicated a significant disappearance of the drug, mainly displaying spectra corresponding to just each type of silica present. Furthermore, the spectra did not display any obvious additional peaks, thus indicating there had been no significant changes in the chemical structure or drug-silica interactions.

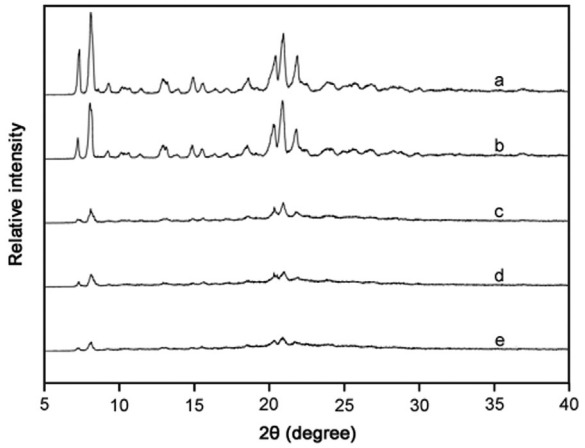

Fig. 1. XRD patterns for (a) phenylbutazone, (b) processed phenylbutazone, (c) phenylbutazone and AL-1 FP, (d) phenylbutazone and XDP 3150, and (e) phenylbutazone and XDP 3050.

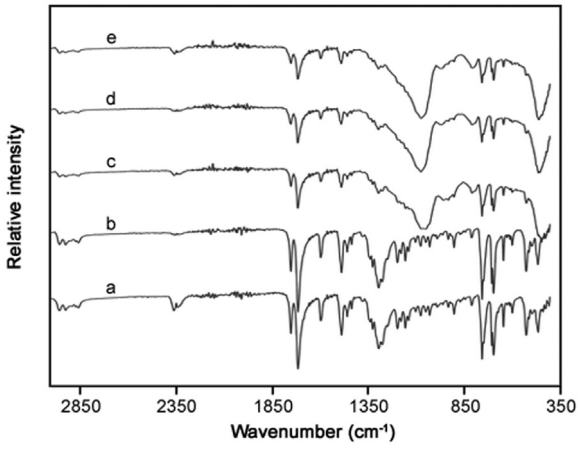

Fig. 3. FT-IR analysis of (a) phenylbutazone, (b) processed phenylbutazone, (c) phenylbutazone and AL-1 FP, (d) phenylbutazone and XDP 3150, and (e) phenylbutazone and XDP 3050 silicas after formulation.

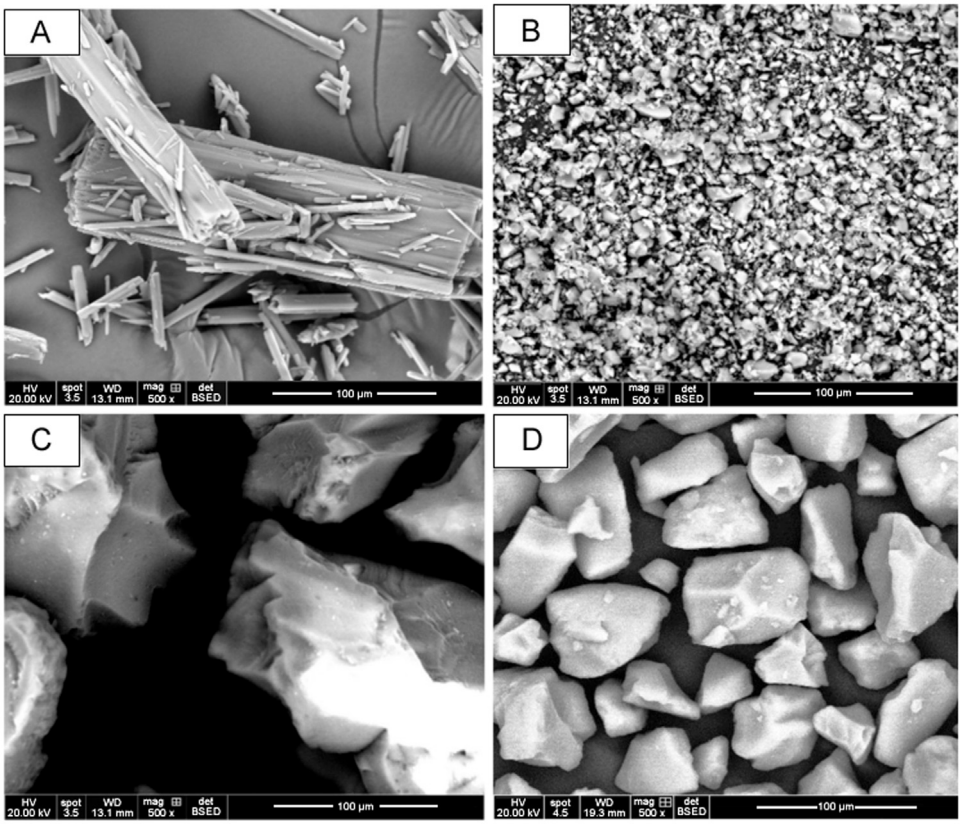

Fig. 4. Scanning electron micrographs for particles of (A) phenylbutazone, (B) AL-1 FP, (C) XDP 3150, and (D) XDP 3050 silicas prior to formulation.

Surface morphologies of the pure phenylbutazone and the three Syloid® silicas prior to formulation, processed phenylbutazone, and Syloid® silica-based formulations – XDP 3050, XDP 3150 and AL-1 FP are presented in Figs. 4 and 5. The drug's crystalline state, along with the disordered irregular shapes of AL-1 FP, XDP 3150, and XDP 3050 silicas was evident by SEM (Fig. 4). The SEM image confirmed the insignificant effect of processed phenylbutazone as the drug retained a crystalline structure. However, there was a uniform distribution of phenylbutazone on the surface of AL-1 FP due to a larger surface area, smaller pore volume and pore diameter. For Syloid® XDP 3150 and XDP 3050 based formulations, there was an even distribution of the former particles with phenylbutazone particles reduced in size while for the latter, more of the drug was confined in the pores and on the surface, visible in the SEM images (Fig. 5).

3.2. *In vitro phenylbutazone release*

Dissolution profiles of phenylbutazone loaded Syloid® silicas were investigated for a period of 30 min in pH 7.0 phosphate buffer. As can be seen in Fig. 6, pure phenylbutazone that had not undergone the formulation process exhibited 7.2% (± 1.4%) drug release after 5 min yet only increased to a maximum of 43.7% (± 2.3%) release after 30 min. For many drugs, this low percentage of drug release after this time would be deemed unsuitably low and may limit bioavailability. Through undertaking the formulation process with the drug alone, i.e. hydration, heating, filtering, drying then sieving, the percentage of drug release, or more accurately in this case, dissolution after 30 min was 43.8% (± 7.9%). Therefore, it has been confirmed that exposure of the drug to the formulation process did not affect the profile observed, i.e. hydrating through sieving did not enhance the effects observed for phenylbutazone. All three Syloid® silica based formulations exhibited a dramatic enhancement in percentage dissolution, confirming that the presence of Syloid® silica contributed to the increase. Firstly, XDP 3150 achieved a percentage release of 42.4% (± 1.9%) after only 5 min, i.e. almost equal to that observed for drug alone after twice as long. After a period of 30 min, this value had increased to 78.3% (± 2.2%), far higher than that seen for drug alone or drug that had undergone the formulation process. Secondly, Syloid® silicas AL-1 FP did not show such a promising percentage release after 5 min (30.2% (± 1.2%)) compared with XDP 3150, yet after a total of 30 min had exceeded the former Syloid® silica to reach a maximum percentage release of 86.0% (± 4.2%). Finally, XDP 3050 was found to be the most successful Syloid® silica for enhancing percentage release with an impressive 49.4% (± 0.8%) released after 5 min, i.e. greater than the total seen for pure drug after 30 min, increasing to a maximum of 99.6% (± 3.0%) release after 30 min.

When determining why all three Syloid® silicas enhanced the percentage of dissolution following a standard formulation method, it would appear that the transformation from the crystalline to amorphous form (as evidenced by XRD and dissolution profiles of processed samples) plays a key role. This has been the conclusion of other researchers, when investigating alternative mesoporous materials [31], and fits well with the results from this work. However, when considering why the three Syloid® silicas did not facilitate the same increase in percentage release, it is more appropriate to consider their relative physicochemical properties, specifically those identified in Table 1. For example, AL-1 FP and XDP 3050 pore sizes are very different, in that AL-1 FP has small mesopores, i.e. a smaller pore volume and diameter compared with XDP 3050. Based on the pattern of increasing percentage release, i.e. from XDP 3150 to AL-1 FP to XDP 3050, it would appear that two properties of the Syloid® silicas may play a key role in controlling the process, namely, surface area and/or

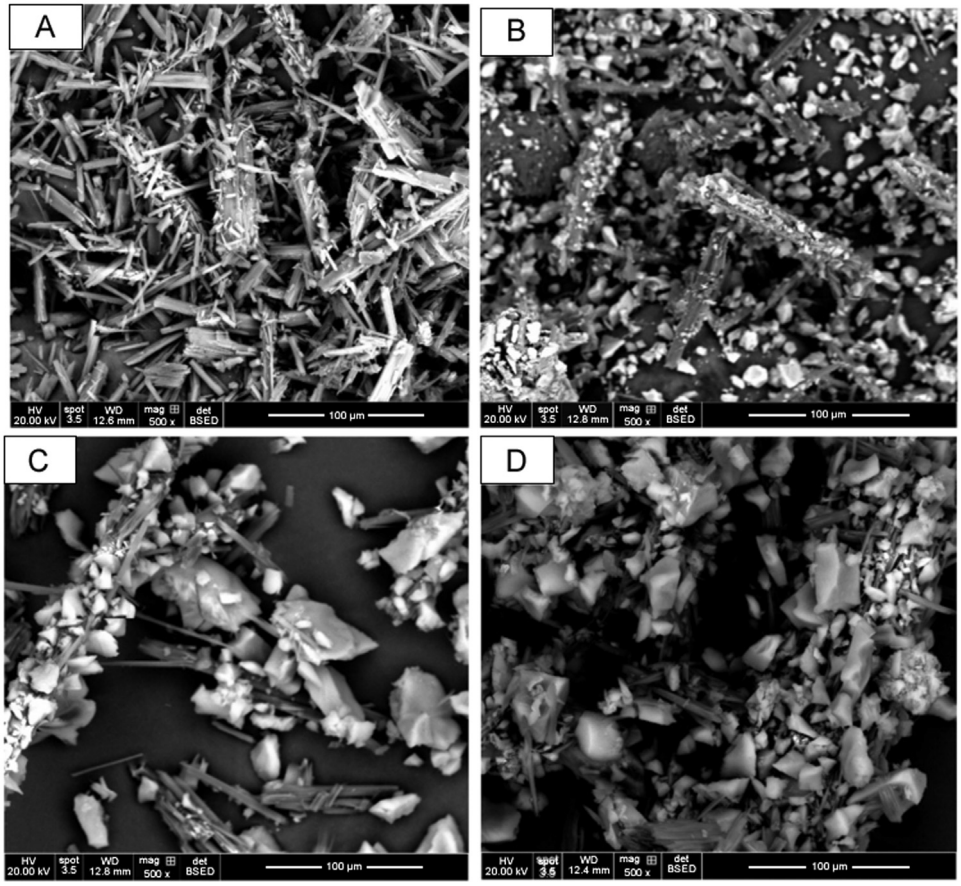

Fig. 5. Scanning electron microscope images (SEM) of (A) processed phenylbutazone, (B) phenylbutazone and AL-1 FP, (C) phenylbutazone and XDP 3150, and (D) phenylbutazone and XDP 3050 after formulations.

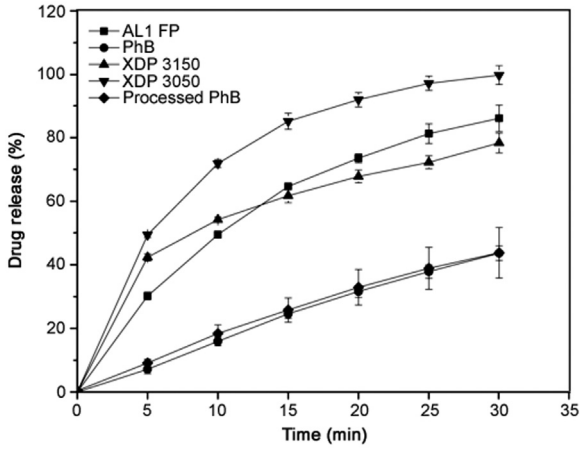

Fig. 6. Phenylbutazone release profiles for phenylbutazone (PhB), processed phenylbutazone, and Syloid® silica based formulations – XDP 3050, XDP 3150 and AL-1 FP. Each data point represents the mean of triplicate results (± SD).

pore diameter. Interestingly, pore volume does not appear to be an influential factor for the rate and extent of dissolution, yet pore diameter is. In this work it appears that a large pore diameter, with a small surface area, maximises the extent of dissolution, which again, fits well with the findings of other studies with mesoporous microspheres [30,33]. As a consequence of this, it is not only possible to dramatically enhance the rate and extent of dissolution, but also to vary the percentage depending upon the type of Syloid® silica used. Another potentially influential factor is the formation of aggregates which may affect the drug release profile through the creation of particle aggregation. If this is the case, then it can be proposed that there are two unique structures within the formulation: drug within pores and aggregates between particles which can both contribute to drug release.

4. Conclusions

In summary, it has been confirmed that it is possible to formulate Syloid® silica based formulations to enhance the dissolution of a poorly soluble drug, in this case, phenylbutazone. Characterisation data implies that this enhancement is a result of a change in crystallinity and the ability of the drug to enter pores within the Syloid® silica structure. All three Syloid® silicas analysed demonstrated a dramatic increase in percentage release with their final percentage values linked to the Syloid® silica pore diameter and/or surface area. This finding can be of benefit for not only phenylbutazone-based equine formulations but potentially a far wider range of compounds that exhibit poor aqueous solubility, which will help alleviate bioavailability issues. To ensure that long-term stability is not a limiting factor for formulation possibilities, it is the intended subject of future sample analysis, using techniques such as XRD and SEM.

Conflicts of interest

The authors declare that there are no conflicts of interest.

References

[1] Y. Choudhari, H. Hoefer, C. Libanati, et al., Mesoporous silica drug delivery systems. N. Shah, H. Sandhu, D.S. Choi, et al. (Eds.), Amorphous Solid Dispersions: Theory and Practice, Springer, New York, 2014:665–693.

[2] W. Xu, J. Riikonen, V.P. Lehto, Mesoporous systems for poorly soluble drugs, Int. J. Pharm. 453 (2012) 181–197.

[3] S.C. Shen, W.K. Ng, L.S.O. Chia, et al., Applications of mesoporous materials as excipients for innovative drug delivery and formulation, Curr. Pharm. Des. 19 (2013) 6270–6289.

[4] C.A. McCarthy, R.J. Ahern, R. Dontireddy, et al., Mesoporous silica formulation strategies for drug dissolution enhancement: a review, Expert Opin. Drug Deliv. 13 (2016) 93–108.

[5] S.H. Cheng, W.N. Liao, L.M. Chen, et al., pH-controllable release using functionalized mesoporous silica nanoparticles as an oral drug delivery system, J. Mater. Chem. 21 (2011) 7130–7137.

[6] Y. Hu, X. Dong, L. Ke, et al., Polysaccharides/mesoporous silica nanoparticles hybrid composite hydrogel beads for sustained drug delivery, J. Mater. Sci. 52 (2017) 3095–3109.

[7] H. Wen, Y. Qiu, Adsorption of small drug particles at the surface of large excipients, Pharm. Technol. Eur. 18 (2006) 39–44.

[8] A. Kiwilsza, A. Pajzderska, J. Mielcarek, et al., Dynamical properties of nimodipine molecules confined in SBA-15 matrix, Chem. Phys. 475 (2016) 126–130.

[9] N. Murillo-Cremaes, A.M. López-Periago, J. Saurina, et al., Nanostructured silica-based drug delivery vehicles for hydrophobic and moisture sensitive drugs, J. Supercrit. Fluids 73 (2013) 34–42.

[10] A. Patil, U.N. Chirmade, V. Trivedi, et al., Encapsulation of water insoluble drugs in mesoporous silica nanoparticles using supercritical carbon dioxide, J. Nanomed. Nanotechnol. 2 (2011) 111–119.

[11] R.J. Ahern, A.M. Crean, K.B. Ryan, The influence of supercritical carbon dioxide ($SC\text{-}CO_2$) processing conditions on drug loading and physicochemical properties, Int. J. Pharm. 439 (2012) 92–99.

[12] R.K. Kankala, Y.S. Zhang, S.B. Wang, et al., Supercritical fluid technology: an emphasis on drug delivery and related biomedical applications advanced healthcare, Materials 6 (2017) 1700433.

[13] Y. Choudhari, U. Reddy, F. Monsuur, et al., Comparative evaluation of porous silica based carriers for lipids and liquid drug formulations, Mesoporous Biomater. 1 (2014) 61–74.

[14] F. Monsuur, Y. Choudhari, U. Reddy, et al., Solvent free amorphisation for pediatric formulations (minitablets) using mesoporous silica, Int. J. Pharm. 511 (2016) 1135–1136.

[15] L.J. Waters, T. Hussain, G. Parkes, et al., Inclusion of fenofibrate in a series of mesoporous silicas using microwave irradiation, Eur. J. Pharm. Biopharm. 85 (2013) 936–941.

[16] C.A. McCarthy, W. Faisal, J.P. O'Shea, et al., In vitro dissolution models for the prediction of in vivo performance of an oral mesoporous silica formulation, J. Control. Release 250 (2017) 86–95.

[17] R.K. Kankala, C.G. Liu, A.Z. Chen, et al., Overcoming multidrug resistance through the synergistic effects of hierarchical pH-sensitive, ROS-generating nanoreactors, ACS Biomater. Sci. Eng. 3 (2017) 2431–2442.

[18] R.K. Kankala, Y. Kuthati, C.L. Liu, et al., Killing cancer cells by delivering a nanoreactor for inhibition of catalase and catalytically enhancing intracellular levels of ROS, RSC Adv. 5 (2015) 86072–86081.

[19] T. Limnell, H.A. Santos, E. Mäkilä, et al., Drug delivery formulations of ordered and nonordered mesoporous silica: comparison of three drug loading methods, J. Pharm. Sci. 100 (2011) 3294–3306.

[20] P. Kinnari, E. Mäkilä, T. Heikkilä, et al., Comparison of mesoporous silicon and non-ordered mesoporous silica materials as drug carriers for itraconazole, Int. J. Pharm. 414 (2011) 148–156.

[21] W. Xu, J. Riikonen, V.P. Lehto, Mesoporous systems for poorly soluble drugs, Int. J. Pharm. 453 (2013) 181–197.

[22] L.R. Soma, C.E. Uboh, G.M. Maylin, The use of phenylbutazone in the horse, J. Vet. Pharmacol. Ther. 35 (2012) 1–12.

[23] C. Castagnetti, J. Mariella, Anti-inflammatory drugs in equine neonatal medicine. Part I: nonsteroidal anti-inflammatory drugs, J. Equine Vet. Sci. 35 (2015) 475–480.

[24] L.C. Sanchez, S.A. Robertson, Pain control in horses: what do we really know? Equine Vet. J. 46 (2014) 517–523.

[25] J.C. De Grauw, J.P.A.M. van Loon, C.H.A. van de Lest, et al., In vivo effects of phenylbutazone on inflammation and cartilage-derived biomarkers in equine joints with acute synovitis, Vet. J. 201 (2014) 51–56.

[26] U. Domańska, A. Pobudkowska, A. Pelczarska, et al., Modelling, solubility and pKa of five sparingly soluble drugs, Int. J. Pharm. 403 (2011) 115–122.

[27] S. Khan, H. Batchelor, P. Hanson, et al., Physicochemical characterisation, drug polymer dissolution and in vitro evaluation of phenacetin and phenylbutazone solid dispersions with polyethylene glycol 8000, J. Pharm. Sci. 100 (2011) 4281–4294.

[28] M. Van Speybroeck, V. Barillaro, T.D. Thi, et al., Ordered mesoporous silica material SBA-15: a broad-spectrum formulation platform for poorly soluble drugs, J. Pharm. Sci. 98 (2009) 2648–2658.

[29] S.L. Longhofer, C.R. Reinemeyer, S.V. Radecki, Evaluation of the palatability of three nonsteroidal antiinflammatory top-dress formulations in horses, Vet. Ther. 9 (2008) 122–127.

[30] Y. Hu, J. Wang, Z. Zhi, et al., Facile synthesis of 3D cubic mesoporous silica microspheres with a controllable pore size and their application for improved delivery of a water-insoluble drug, J. Colloid Interface Sci. 363 (2011) 410–417.

[31] Z. Guo, X.M. Liu, L. Ma, et al., Effects of particle morphology, pore size and surface coating of mesoporous silica on Naproxen dissolution rate enhancement, Colloids Surf. B: Biointerfaces 101 (2013) 228–235.

[32] R. Al-Oweini, H. El-Rassy, Synthesis and characterization by FTIR spectroscopy of silica aerogels prepared using several Si(OR)4 and R″Si(OR′)3 precursors, J. Mol. Struct. 919 (2009) 140–145.

[33] A. Martín, R.A. García, D.S. Karaman, et al., Polyethyleneimine-functionalized large pore ordered silica materials for poorly water-soluble drug delivery, J. Mater. Sci. 49 (2014) 1437–1447.

Journal of Pharmaceutical Analysis 8 (2018) 187–193

Contents lists available at ScienceDirect

Journal of Pharmaceutical Analysis

journal homepage: www.elsevier.com/locate/jpa
www.sciencedirect.com

Original Research Article

Enrichment and immobilization of macromolecular analytes on a porous membrane utilizing permeation drag

Pedram Madadkar, Rahul Sadavarte, Raja Ghosh *

Department of Chemical Engineering, McMaster University, 1280 Main Street West, Hamilton, Ontario, Canada L8S 4L7

ARTICLE INFO

Article history:
Received 7 December 2017
Received in revised form
3 February 2018
Accepted 15 March 2018
Available online 16 March 2018

Keywords:
Macromolecule
Enrichment
Immobilization
Concentration polarization
Permeation drag
Immunoassay
Membrane
Ultrafiltration

ABSTRACT

Enrichment and immobilization of analytes by chemical bonding or physical adsorption is typically the first step in many commonly used analytical techniques. In this paper, we discuss a permeation drag based technique as an alternative approach for carrying out location-specific immobilization of macromolecular analytes. Fluorescein isothiocyanate (FITC) labeled macromolecules and their complexes were enriched near the surface of ultrafiltration membranes and detected by direct visual observation and fluorescence imaging. The level of macromolecule enrichment at the immobilization sites could be controlled by manipulating the filtration rate and thereby the magnitude of permeation drag. Higher enrichment as indicated by higher fluorescence intensity was observed at higher filtration rates. Also, larger macromolecules were more easily enriched. The feasibility of using this technique for detecting immunocomplexes was demonstrated by carrying out experiments with FITC labeled bovine serum albumin (FITC-BSA) and its corresponding antibody. This permeation drag based enrichment technique could potentially be developed further to suit a range of analytical applications involving more sophisticated detection methods.

1. Introduction

Attachment of biological macromolecules on diverse surfaces has direct implications on development of detection and analytical methods with application in bio-sensors and medical diagnosis [1,2]. Location-specific immobilization of analytes by chemical bond formation [3,4], or physical methods such as adsorption [5,6], is typically carried out as the first step in many analytical techniques such as immunoassays [7,8], surface plasmon resonance analysis [9], and Raman spectroscopy [10]. Once the molecules are immobilized at their desired locations, they are probed and analyzed using appropriate detection methods.

Permeation drag refers to the drag force exerted on solute molecules and particles towards the surface of a membrane by bulk medium during membrane filtration processes such as ultrafiltration and microfiltration [11–14]. Our proposition is that such permeation drag induced accumulation of macromolecules near the membrane surface of retaining ultrafiltration membranes could be utilized as an alternative physical approach for immobilizing macromolecular analytes. While various other techniques have been carried out to immobilize bio-macromolecules onto membranes [15,16], we demonstrate the feasibility of macromolecule immobilization by permeation drag. Ultrafiltration experiments were carried out using fluorescein isothiocyanate (FITC) labeled macromolecules. Location-specific immobilization was demonstrated by direct visual observation and fluorescent imaging. Film theory was used to explicate the permeation drag induced enrichment based on which the accumulation of retained macromolecules takes place within a stagnant film adjacent to the membrane surface. More or less corresponding to the hydrodynamic boundary layer, this is widely referred to as concentration polarization layer in membrane filtration processes. A large number of macromolecules are accumulated in a narrow region with two levels of concentration asymmetry: The concentration of the solutes is significantly higher in the polarized layer compared to the bulk solution; also, within the layer, the macromolecule concentration increases in an exponential manner from the bulk concentration (C_b) to the concentration at the membrane surface (C_w) [17]. If macromolecules are totally retained by a membrane, the two concentration terms are linked by the equation shown below:

$$C_w = C_b \exp(Q\delta/AD) \quad (1)$$

In this equation, Q represents the flow rate through the membrane having the area of A, δ represents the thickness of the concentration polarization layer, and D is the diffusivity of the solute. As a result, when $Q > 0$, C_w will be greater than C_b, and in a

Peer review under responsibility of Xi'an Jiaotong University.

* Corresponding author.
E-mail address: rghosh@mcmaster.ca (R. Ghosh).

https://doi.org/10.1016/j.jpha.2018.03.002

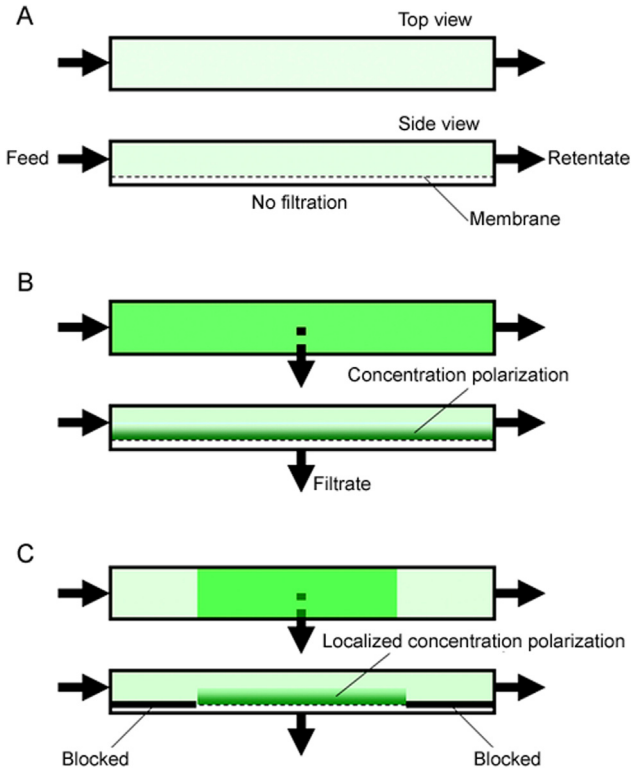

Fig. 1. Simplified top- and side-view representation of localized permeation drag induced immobilization taking place within a membrane module (A: no filtration; B: enrichment on entire membrane; C: localized enrichment).

typical ultrafiltration experiment, C_w could be larger by more than two orders of magnitude [13,18]. Clearly, concentration polarization caused by permeation drag could be utilized for quite significant enrichment of macromolecules on the surface of a membrane. Such enrichment would also be dynamic in nature, i.e. the accumulated layer of macromolecules would largely disappear if the filtration process is stopped. Eq. (1) suggests that the extent of such enrichment could be manipulated by adjusting the values of Q, δ, and D. While Q could be controlled by adjusting the transmembrane pressure, the value of δ depends on the flow behaviour adjacent to the membrane and D depends on the size of the macromolecule.

Fig. 1 shows a dilute solution of an FITC-labeled macromolecule flowing through a channel having an ultrafiltration membrane on one side. In the absence of permeation drag, i.e. when filtration rate is zero, concentration polarization does not occur (Fig. 1A). If filtrate was drawn through the membrane either using positive pressure or suction, the enriched layer of macromolecules adjacent to the membrane would be evident from the enhanced fluorescence intensity (Fig. 1B). Further, if a part of the membrane was blocked, concentration polarization would occur in a localized manner only in the non-blocked part (Fig. 1C). The enhanced fluorescence due to enrichment of macromolecules would now be easier to observe due to the contrast between regions with and without polarization. Based on Eq. (1), it may be predicted that higher enrichment would occur at higher filtration rates, and larger macromolecules and macromolecular complexes (which have lower diffusivity) would be easier to enrich. Accordingly, specific regions of rectangular flat sheet ultrafiltration membranes were blocked by applying polyurethane glue. Fluorescent patterns and features were generated on these membranes by localized concentration polarization of FITC-labeled dextran. The effect of filtration rate and molecular weight of macromolecules on intensity of fluorescence was examined.

The interactions between antigens and corresponding antibody molecules lead to the formation of macromolecular complexes called immunocomplexes, the ability to recognize which is widely exploited to carry out immunoassays [19,20]. Such immunocomplexes would be fairly easy to enrich as they are larger in size. The working principle of the localized concentration polarization based immunocomplex detection method is outlined in Fig. 2, which shows the polarization of a fluorescence-labeled antigen (Fig. 2A), the polarization of a mixture of the antigen and non-specific antibody (Fig. 2B), and the polarization of the immunocomplex (Fig. 2C). As indicated in the figure, the highest intensity could be expected in (Fig. 2C). The difference in intensity could therefore be utilized for immunocomplex detection. Proof-of-concept of such immunocomplex detection was obtained by using FITC-labeled bovine serum albumin (FITC-BSA) as model antigen and rabbit anti-BSA as corresponding antibody. The Effect of filtration rate, antigen concentration and antibody concentration on intensity was examined.

2. Experimental

2.1. Materials

FITC-dextran of different molecular weights (40 kDa, FD40S; 70 kDa, FD70S; 500 kDa, 46947; and 2000 kDa, FD2000S), FITC-BSA (A9771), anti-BSA (B1520), and whole antiserum polyclonal

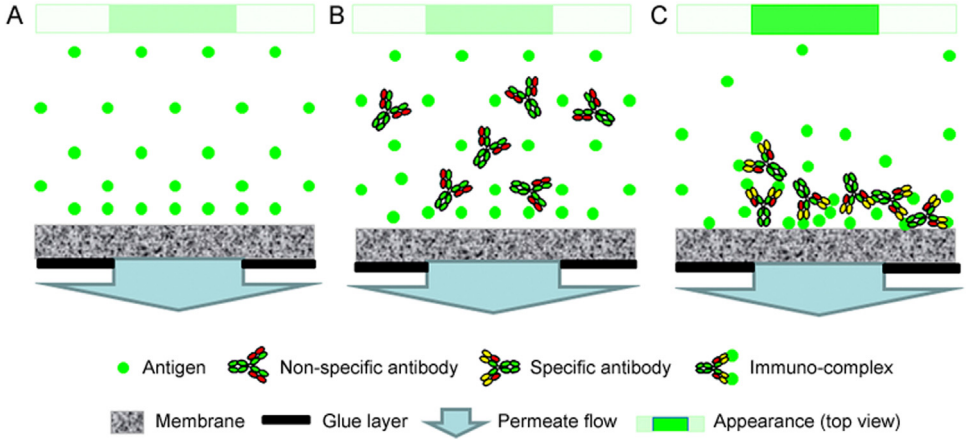

Fig. 2. Schematic diagram for immunocomplex detection by localized permeation drag induced immobilization explaining the basis for difference in fluorescent intensity (A: antigen only; B: antigen with non-specific antibody; C: antigen with specific antibody).

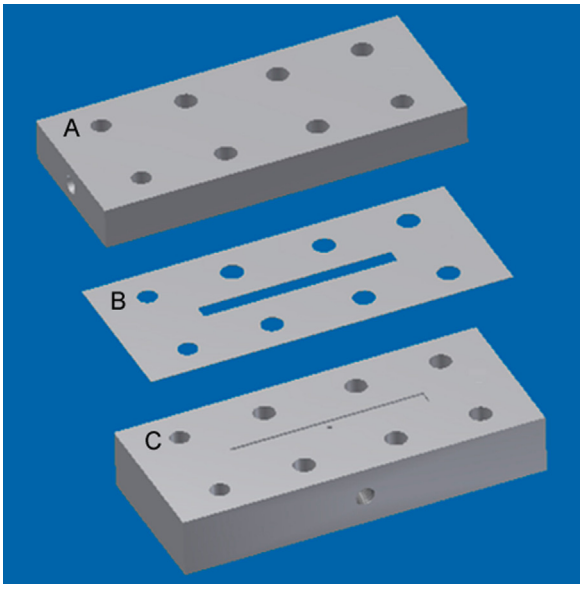

Fig. 3. Membrane module used for carrying out localized permeation drag induced immobilization experiments (A: top plate; B: spacer; C: bottom plate).

antibody raised in rabbit were purchased from Sigma-Aldrich Canada Ltd, Oakville, ON, Canada. Normal rabbit serum (PLN 5001) was purchased from Invitrogen (Life Technologies Inc.), Burlington, ON, Canada. Polyethersulfone ultrafiltration membranes (OMEGA 10 K, 10 kDa MWCO; OMEGA 30 K, 30 kDa MWCO) were purchased from Pall Life Sciences, Ann Arbor, MI, USA. Elmer's Ultimate Glue (polyurethane glue) was purchased from Elmer's Products Canada Corporation, Toronto, ON, Canada. High quality water (18.2 MΩ cm) was obtained from a Barnstead DiamondTM.

NANOpure water purification unit (Dubuque, IA, USA) was used to prepare feed solutions used in the ultrafiltration experiments.

2.2. Methods

Rectangular strips (74 mm × 12 mm) were cut out from the ultrafiltration membrane sheet. Specific regions of these were blocked by applying polyurethane glue on the filtrate side using a paint brush followed by curing at room temperature for 24 h. The membrane strips were housed within a tangential flow module (Fig. 3) which consisted of a membrane spacer (made from 0.2 mm thickness Teflon® sheet) placed between a Delrin® bottom plate and a transparent acrylic top plate. The rectangular slot within spacer served as the cross-flow channel (40 mm × 3 mm × 0.2 mm). The bottom plate was provided with a slot corresponding to the cross-flow channel within the spacer. This slot was fitted with a wire-mesh, flush with the top surface of the bottom plate.

The experimental set-up is shown in Fig. 4. The membrane module was placed inside a cardboard box, painted black on the inside to minimize reflection of light, and having dimensions of 20 cm × 15 cm × 5 cm. A Model ENF-260 °C UV lamp (Spectronic Corporation, Westbury, NY, USA) was attached with its window

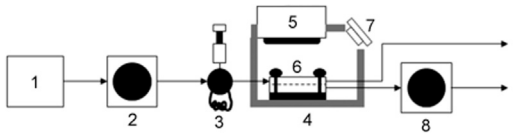

1 Buffer reservoir, 2 Cross-flow pump, 3 Sample injector, 4 Concentration polarization detector

5 UV lamp, 6 Membrane module, 7 Digital camera, 8 Filtrate pump

Fig. 4. Experimental set-up used for carrying out localized permeation drag induced immobilization experiments.

directly above the membrane module to illuminate the membrane surface with short wavelength ultraviolet light (254 nm). A digital camera (Sony Cyber-shot, Model DSC-WX7, Japan) was fixed within a slot in the box and was used to obtain photographs and video clips of the membrane surface during the experiments.

In the FITC-dextran experiments, the feed solutions were prepared by dissolving the appropriate FITC-dextran in water. All solutions used in the immunocomplex detection experiments were prepared in phosphate buffered saline (PBS, pH 7.4). The PBS buffer contained sodium chloride, potassium chloride, disodium hydrogen phosphate, and potassium dihydrogen phosphate with the concentrations of 8.0, 0.2, 1.42, and 0.2 g/L, respectively. Water or buffer was pumped from a reservoir to the membrane module using an MCP model C.P. 78002-00 peristaltic pump (Ismatec, Switzerland) while the filtrate was generated by suction using a HiLoad P-50 pump (GE Healthcare, Piscataway, NJ, USA). Sample loops having different volumes were used to inject the feed solutions into the membrane module.

Video clips were recorded in the MTS format and the extent of zooming was kept the same in all experiments. Snapshots were obtained from the video files using Windows Live Movie Maker and processed for fluorescent intensity analysis using Image J. The polarized membrane area within the spacer was selected and its average intensity was measured using Image J as "mean gray scale intensity" value. To avoid any experiment-to-experiment variation, the intensity was normalized by subtracting the base line intensity in each case, this being the intensity of the membrane before any fluorescent sample entered the module.

3. Results and discussion

Permeation drag induced enrichment and immobilization experiments were first carried out using an ultrafiltration membrane strip (10 kDa MWCO) with three parallel rectangular (3.5 mm × 1 mm) non-blocked areas (shaded in light grey in Fig. 5). The feed solution which consisted of 0.2 mg/mL 40 kDa FITC-dextran in water was injected into the membrane module at a flow rate of 0.3 mL/min using a 5 mL sample loop. In the absence of permeation drag, the intensity of green fluorescence on the membrane was more or less uniformly faint (Fig. 5A). The filtrate pump was switched on and the combined filtration rate through the three unblocked areas was maintained at 0.15 mL/min. The enhanced green fluorescence at the three unblocked locations was clearly distinguishable from the rest of the membrane (Fig. 5B). The filtration rate was increased to 0.25 mL/min and this resulted in a significant increase in the fluorescence intensity at these regions (Fig. 5C). These results are consistent with Eq. (1), which predicts that more macromolecules would accumulate near the membrane surface at higher filtration rates. The filtrate pump was then switched off and in less than 30 s, the fluorescent patterns completely disappeared and the non-blocked regions were no longer distinguishable from the rest of the membrane, clearly indicating that fouling was negligible. Similar experiments were carried out at cross-flow rates of 0.4 and 0.5 mL/min (data not shown). The fluorescence obtained at 0.4 mL/min was significantly fainter than that obtained at 0.3 mL/min while at 0.5 mL/min, the enrichment could not be observed.

The kinetics of the accumulation and dissipation of fluorescent-labeled analytes was studied using an ultrafiltration membrane strip similar to that used in the experiments discussed above. FITC-dextran solution (40 kDa, 0.2 mg/mL) was injected into the membrane module at a flow rate of 0.3 mL/min using a 5 mL sample loop. The filtrate pump was switched on and maintained at a rate of 0.2 mL/min. Fig. 6 shows the images obtained at different times during the accumulation of the dextran molecules through the

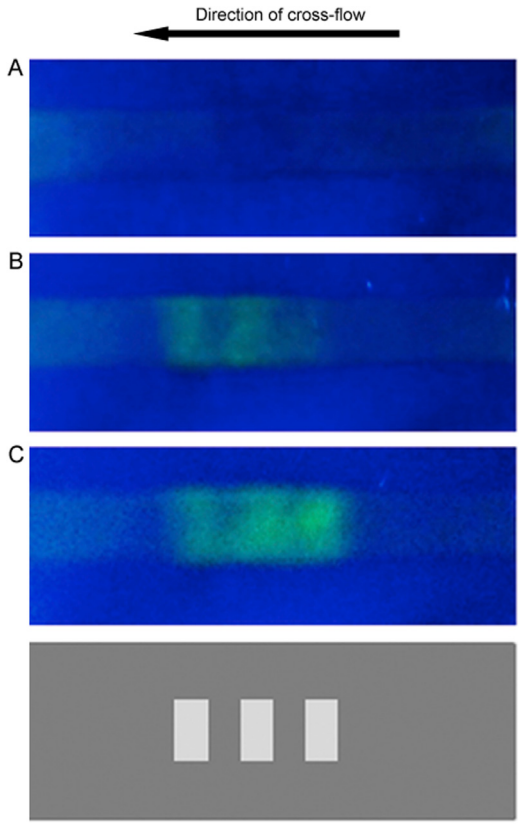

Fig. 5. Localized permeation drag induced immobilization of FITC-dextran (molecular weight: 40 kDa; feed concentration: 0.2 mg/mL; cross-flow rate: 0.3 mL/min; loop size: 5 mL; A: no filtration; B: 0.15 mL/min filtration rate; C: 0.25 mL/min filtration rate).

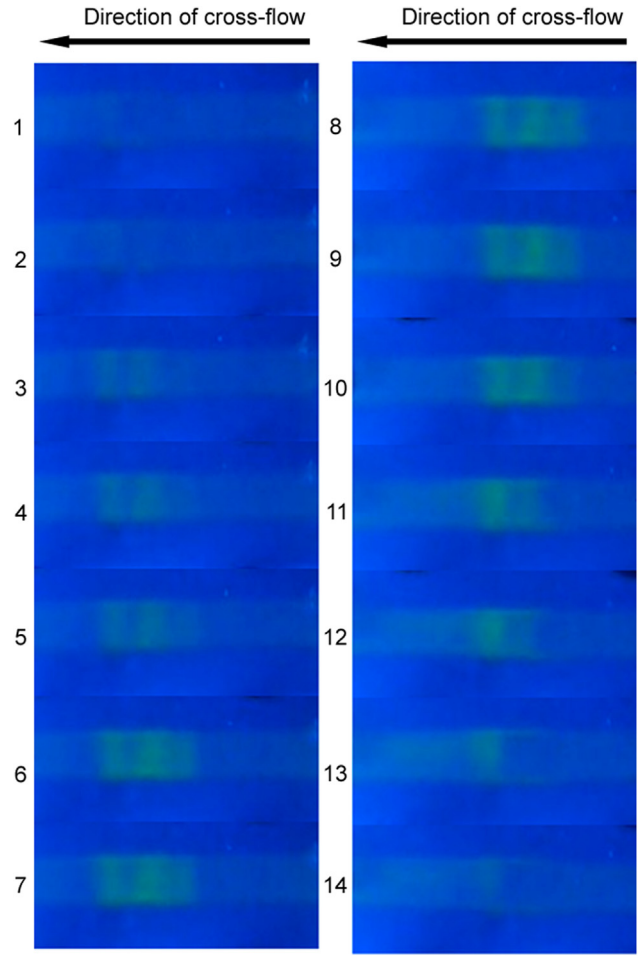

Fig. 6. The kinetics of the accumulation (slides 1–7) and dissipation (slides 8–14) of FITC-dextran (molecular weight: 40 kDa; feed concentration: 0.2 mg/mL; cross-flow rate: 0.3 mL/min; loop size: 5 mL; filtration rate: 0.2 mL/min).

formation of localized concentration polarization layer (frames 1–7). After about 8 s from start of filtration (frame 3), the three parallel bars corresponding to the non-blocked regions of the membrane could just about be distinguished. With time, the intensity increased until in about a minute (frame 7) and a steady state was reached. When the localized enrichment had fully developed, the filtrate pump was switched off to observe its dissipation. Frames 8–14 were obtained at different time during this phase of the experiment. The rate of dissipation of the immobilized analytes was significantly faster than its rate of accumulation. In a matter of 10 s or so (frame 14), the fluorescent features almost completely disappeared, from right to left, i.e. in the direction of cross-flow. During the dissipation phase, FITC-dextran released was clearly visible in the form of a fluorescent streak close to the outlet.

Fig. 7 shows the immobilization obtained with three different types of FITC-dextran (70 kDa, 500 kDa and 2000 kDa). The ultrafiltration membrane used in these experiments was of 30 kDa MWCO and the non-blocked area of the membrane had a dimension of 3 mm × 3 mm (shaded in light grey).

These experiments were carried out at a cross-flow rate of 0.21 mL/min and a filtration rate of 0.12 mL/min. The FITC- dextran feed solution (0.2 mg/mL) was injected into the module using a 5 mL sample loop. The lowest and highest intensities were observed with 70 kDa and 2000 kDa FITC-dextran, respectively. The intensity observed with the 500 kDa FITC-dextran was only slightly higher than that with 70 kDa dextran. These results are consistent with Eq. (1), which predicts that permeation drag would be more effective for larger macromolecules.

The immunocomplex detection experiments were carried out using 30 kDa MWCO ultrafiltration membranes having a non-blocked area of 40 mm × 1 mm (as shown in light grey shading in Fig. 8). Preliminary experiments showed that an elongated non-blocked area along the length of the cross-flow channel gave better immunocomplex immobilization than the smaller non-blocked areas used in the dextran experiments. Fig. 8 shows the results obtained with FITC-BSA (A), FITC-BSA–non-specific antibody mixture (B), FITC-BSA–anti-BSA mixture (C), and FITC-BSA – anti-BSA mixture with no filtration (D). These experiments were carried out at a cross-flow rate of 0.21 mL/min and a filtration rate of 0.14 mL/min. Samples were incubated at 37 °C for 75 min, equilibrated to room temperature, and a 100 microliter loop was used for injecting these into the membrane module. The FITC-BSA concentration used in these experiments was 0.2 mg/mL while the anti-BSA or non-specific antibody concentration was 0.5 mg/mL.

Although the intensity observed with FITC-BSA (Fig. 8A) and the mixture of FITC-BSA and non-specific antibody (Fig. 8B) were almost similar, a significantly higher fluorescent intensity was observed with the immunocomplex (Fig. 8C). However, in the absence of filtration, virtually no coloration was observed even with the immunocomplex (Fig. 8D), clearly highlighting the role of permeation drag in the technique. These results unambiguously demonstrate that the permeation drag induced immobilization could be used for immunocomplex detection. This technique could be developed further into immunoassay methods for detecting specific antigens or antibodies in samples.

Further experiments were carried out to examine the effects of variables such as filtration rate, antibody concentration and antigen concentration on immunocomplex detection. Fig. 9 shows the

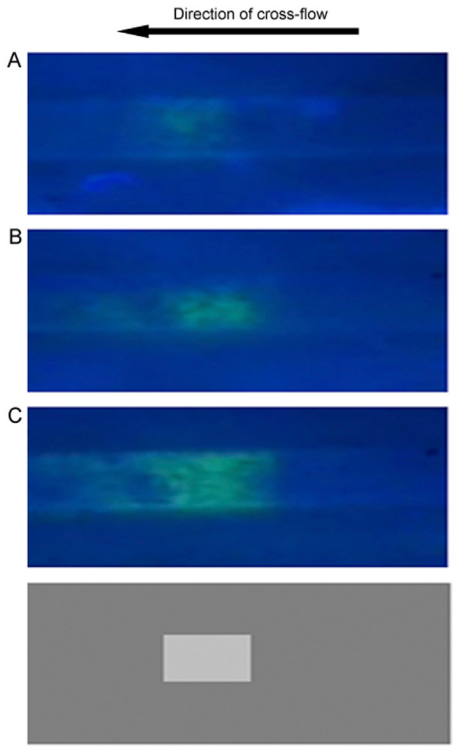

Fig. 7. Effect of molecular weight on intensity of permeation drag induced immobilization (cross-flow rate: 0.21 mL/min; filtration rate: 0.12 mL/min; FITC-dextran feed concentration: 0.2 mg/mL; loop size: 5 mL; A: 70 kDa; B: 500 kDa; 2000 kDa).

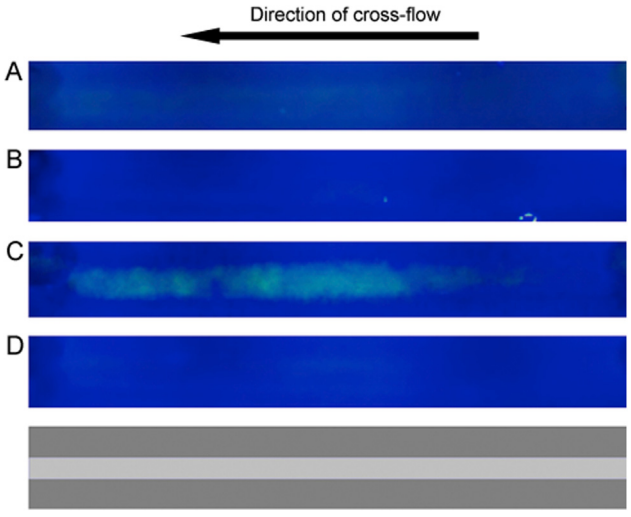

Fig. 8. Fluorescence intensity due to permeation drag induced immobilization of immunocomplex (A: FITC-BSA; B: FITC-BSA–non-specific antibody mixture; C: FITC-BSA–anti-BSA mixture; D: FITC-BSA–anti-BSA mixture without filtration; cross-flow rate: 0.21 mL/min; filtration rate: 0.14 mL/min; sample loop: 100 μL; FITC-BSA concentration: 0.2 mg/mL; non-specific antibody concentration: 0.5 mg/mL; anti-BSA concentration: 0.5 mg/mL).

fluorescent signal intensity (expressed in mean grey value) as function of time observed by injecting 100 μL of FITC-BSA (0.2 mg/mL) alone, and FITC-BSA–antibody mixture (0.2 mg/mL and 0.5 mg/mL) respectively at a cross-flow rate of 0.21 mL/min and a filtration rate of 0.18 mL/min. The fluorescence was significantly and consistently higher with the antigen-antibody complex than with this antigen alone. These results quite clearly validate the working hypothesis of our proposed immunocomplex

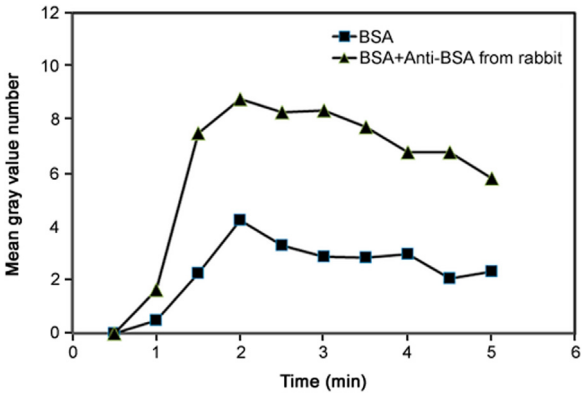

Fig. 9. Fluorescence intensity as function of time observed due to permeation drag induced immobilization of immunocomplex (cross-flow rate: 0.21 mL/min; filtration rate: 0.18 mL/min; sample loop: 100 μL; FITC-BSA concentration: 0.2 mg/mL; anti-BSA concentration: 0.5 mg/mL).

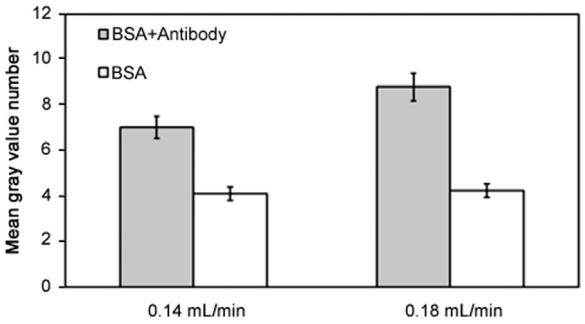

Fig. 10. Effect of filtration rate on fluorescence intensity due to permeation drag induced immobilization of immunocomplex (grey: immunocomplex experiment; white: control experiment; cross-flow rate: 0.21 mL/min; sample loop: 100 μL; FITC-BSA concentration: 0.2 mg/mL; anti-BSA concentration: 0.5 mg/mL).

detection method. In each of these experiments, the maximum fluorescence was observed around 2 min, after which there was a gradual decay in the fluorescence adjacent to the membrane. The variations and the overall decay observed between 2min and 5min are regarded to the effect of the cross flow and the pump induced pulsations on the polarized layer. All subsequently reported fluorescence data from immunocomplex experiment are based on the readings obtained 2 min after injection as peak signal intensity was observed at this time in all these experiments. When the filtration pump was stopped (data not shown in the figure), the fluorescence totally disappeared, indicating that fouling was negligible. Fig. 10 compares the fluorescence data obtained from experiments carried out at a cross flow rate of 0.21 mL/min and two different filtration rates of 0.14 and 0.18 mL/min, respectively. The amounts of FITC-BSA and FITC-BSA – antibody injected in these experiments were the same as that used in the experiment corresponding to Fig. 9. The intensity was found to be significantly higher at the higher filtration rate. This is consistent with the expectations based on Eq. (1) and the experimental results obtained with FITC-dextran immobilization by permeation drag.

Fig. 11 shows the results obtained from immunocomplex detection experiments carried out using different antibody concentration. The antigen, i.e. FITC-BSA concentration in these experiments, was kept fixed at 0.2 mg/mL while three different antibody concentrations (0.5, 0.75 and 5.0 mg/mL) were examined. The cross flow and filtration rates used in these experiments were 0.21 mL/min and 0.14 mL/min, respectively. The figure also shows representative snapshots for each experimental condition as well as control intensity data obtained using FITC-BSA alone. Intensity

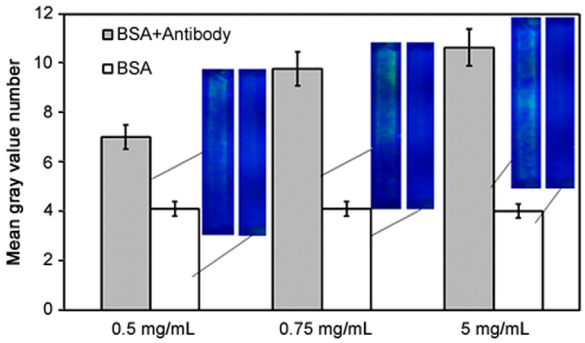

Fig. 11. Effect of anti-BSA concentration on fluorescence intensity due to permeation drag induced immobilization of immunocomplex (grey: immunocomplex experiment; white: control experiment; cross-flow rate: 0.21 mL/min; filtration rate: 0.14 mL/min; sample loop: 100 μL; FITC-BSA concentration: 0.2 mg/mL).

increased quite significantly when the antibody concentration was increased from 0.5 to 0.75 mg/mL. However, the increase in intensity was relatively modest when the antibody concentration was further increased quite significantly to 5 mg/mL.

While these results do suggest that this technique could be utilized for quantitative analysis of antibodies, the non-linear relationship between antibody concentration and intensity clearly indicates the complex nature of the interaction between antigens and antibodies. One IgG antibody molecule can in theory bind up to two antigen molecules. Moreover, large antigens like FITC-BSA have been shown to possess two of more antigenic determinants of the same or different types21. Therefore, different types of immunocomplexes consisting of different permutations and combinations of antigen and antibody, and indeed larger network-like structures could be produced when antigens and antibodies are mixed. Moreover, the proportion of the different types of immunocomplexes would also depend on the antigen-antibody ratio [21].

Fig. 12 shows the effect of FITC-BSA concentration on the intensity obtained by immunocomplex polarization. In these experiments, the antibody concentration was kept fixed at 0.75 mg/mL while two antigen concentrations (0.2 and 0.5 mg/mL) were examined. The remaining experimental conditions were the same as that described in the previous paragraph. Increase in antigen concentration resulted in significant increase in intensity, once again pointing towards the possibility of using such techniques for quantitative measurements.

The current study is primarily intended to show that dynamic and reversible, localized immobilization of large macromolecules and their complexes could be carried out adjacent to an ultrafiltration membrane by inducing permeation drag. In this study,

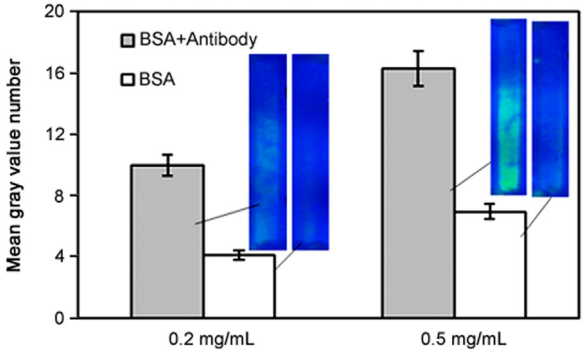

Fig. 12. Effect of FITC-BSA concentration on fluorescence intensity due to permeation drag induced immobilization of immunocomplex (grey: immunocomplex experiment; white: control experiment; cross-flow rate: 0.21 mL/min; filtration rate: 0.14 mL/min; sample loop: 100 μL; anti-BSA concentration: 0.75 mg/mL).

direct visual observation along with fluorescent imaging was utilized to detect FITC-labeled species. Such localized enrichment by ultrafiltration would seem to be a viable alternative to chemical and physical binding methods typically employed in analytical techniques such as immunoassays, surface plasmon resonance and Raman spectroscopy to develop different analytical methods. Unlike chemical and physical binding which require additional steps, reagents and specific solution conditions, localized concentration could be easily carried out at any solution condition. The fact that such localized permeation drag induced enrichment is reversible and can be rapidly dissipated simply by stopping filtration implies that sequential analysis of multiple samples within the same device would be possible. Very simple membrane blocking methods such as applying glue with the paint brush were employed in the current study. Using more sophisticated techniques such as lithography and microcontact printing, better defined patterns and features could be generated on the surface of a membrane, and thereby the reliability, precision and detection capabilities of the technique could be enhanced so that much lower concentrations could be tested. Furthermore, the speed and economy of the techniques could be improved by scaling it down to microfluidic level. Arrays of macromolecule-immobilized regions with varying degrees of enrichment could therefore be created adjacent to a membrane by independently manipulating the local filtration rates. Such capability would be useful for high throughput screening of drugs and other chemical substances, and for studying macromolecule-macromolecule interactions. As shown in Eq. (1), the diffusivity, which in turn is dependent on other properties such as hydrodynamic radius and molecular weight, would affect the extent of enrichment. Moreover, the rate of immobilization as well as the rate of dissipation would depend on these properties as well as on physicochemical parameters such as pH and salt concentration. The technique could therefore potentially be modified to study physical properties of macromolecules and fine particles.

4. Conclusions

The feasibility of carrying out dynamic enrichment of macromolecules and macromolecular complexes near the surface of a membrane was demonstrated by inducing permeation drag followed by direct visual observation and fluorescence imaging of immobilized FITC labeled macromolecules. The fluorescent intensity which is indicative of the extent of enrichment could be manipulated by changing the filtration rate. At the different test conditions examined in this study, macromolecule immobilization was found to be reversible. The rate of macromolecule accumulation when filtration was started was slower than the rate of dissipation when filtration was stopped. Larger macromolecules and macromolecular complexes showed greater fluorescent intensity, indicating that they were easy to enrich. Using this principle, an immunocomplex could be detected and distinguished from its constituent antigen and antibody molecules. Such capability for immunocomplex detection could be developed further into immunoassays for detecting specific antigens and antibodies. Intensity data obtained with different antigen and antibody concentrations clearly suggest that the technique could be suitable for quantitative analysis. Simulation of the permeation drag based enrichment can be carried out using COMSOL Multiphysics for any particular system, leading to enhanced adjustment of the parameters. Overall, localized permeation drag induced immobilization could be a viable alternative to localized immobilization of macromolecules by chemical bonding or physical adsorption, typically carried out as the first step in many commonly used analytical techniques.

Conflicts of interest

The authors declare that there are no conflicts of interest.

Acknowledgments

We thank the Natural Science and Engineering Research Council (NSERC) of Canada for funding this study, Paul Gatt (Chemical Engineering Department, McMaster University) for fabricating the membrane module, and Xiaojiao Shang and Si Pan (Chemical Engineering Department, McMaster University) for helping with photography involved in this study. R.G. holds the Canada Research Chair in Bioseparations Engineering.

References

[1] D. Samanta, A. Sarkar, Immobilization of bio-macromolecules on self-assembled monolayers: methods and sensor applications, Chem. Soc. Rev. 40 (2011) 2567–2592.
[2] D.S. Wilson, S. Nock, Recent developments in protein microarray technology, Angew. Chem. Int. Ed. 42 (2003) 494–500.
[3] D.J. O'Shannessy, M. Brigham-Burke, K. Peck, Immobilization chemistries suitable for use in the BIAcore surface plasmon resonance detector, Anal. Biochem. 205 (1992) 132–136.
[4] R.L. Rich, D.G. Myszka, Advances in surface plasmon resonance biosensor analysis, Curr. Opin. Biotechnol. 11 (2000) 54–61.
[5] J. Schartner, B. Mei, M. Ro, et al., Universal method for protein immobilization on chemically functionalized germanium investigated by ATR-FTIR difference spectroscopy., 135 (2013) 4097-4087.
[6] C.D.K. Sloan, M.T. Marty, S.G. Sligar, et al., Interfacing lipid bilayer nanodiscs and silicon photonic sensor arrays for multiplexed protein-lipid and protein-membrane protein interaction screening, Anal. Chem. 85 (2013) 2970–2976.
[7] A.H.C. Ng, U. Uddayasankar, A.R. Wheeler, Immunoassays in microfluidic systems, Anal. Bioanal. Chem. 397 (2010) 991–1007.
[8] A. Guo, H. Gu, J. Zhou, et al., Immunoaffinity enrichment and mass spectrometry analysis of protein methylation, Mol. Cell. Proteom. 13 (2014) 372–387.
[9] B.M. Gray, ELISA methodology for polysaccaride antigens: portein coupling of polysaccaries for adsorption to plastic tubes, J. Immunol. Methods 28 (1979) 187–192.
[10] X. Qian, A. Levenstein, J.E. Gagner, et al., Protein immobilization in hollow nanostructures and investigation of the adsorbed protein behavior, Langmuir 30 (2014) 1295–1303.
[11] J.E. Flynn, Solute Polarization and Cake Formation in Membrane Ultrafiltration: Causes, Consequences and Control Techniques, Plenum Press, New York 1970:47–97.
[12] A.A. Kozinski, E.N. Lightfoot, Protein ultrafiltration: a general example of boundary layer filtration, AIChE J. 18 (1972) 1030–1038.
[13] A.L. Zydney, A concentration polarization model for the filtrate flux in cross-flow microfiltration of particulate suspensions, Chem. Eng. Commun. 47 (1986) 1–20.
[14] G.Z. Ramon, E.M.V. Hoek, On the enhanced drag force induced by permeation through a filtration membrane, J. Membr. Sci. 392–393 (2012) 1–8.
[15] Q.T. Nguyen, K. Glinel, M. Pontié, et al., Immobilization of bio-macromolecules onto membranes via an adsorbed nanolayer: an insight into the mechanism, J. Membr. Sci. 232 (2004) 123–132.
[16] Q.T. Nguyen, Z. Ping, T. Nguyen, et al., Simple method for immobilization of bio-macromolecules onto membranes of different types, J. Membr. Sci. 213 (2003) 85–95.
[17] R. van Reis, E.M. Goodrich, C.L. Yson, et al., Constant C_{wall} ultrafiltration process control, J. Membr. Sci. 130 (1997) 123–140.
[18] H.B. Winzeler, G. Belfortb, Enhanced performance for pressure-driven membrane processes: the argument for fluid instabilities, J. Membr. Sci. 80 (1993) 35–47.
[19] D.C. Culle, R.G.W. Brown, C.R. Lowe, Detection of immune-complex formation via surface plasmon resonance on gold-coated giffraction gratings, Biosensors 3 (1987) 211–225.
[20] J.H. Han, H.J. Kim, L. Sudheendra, et al., Photonic crystal lab-on-a-chip for detecting staphylococcal enterotoxin B at low attomolar concentration, Anal. Chem. 85 (2013) 3104–3109.
[21] N.H. Chiem, D.J. Harrison, Monoclonal antibody binding affinity determined by microchip based capillary elecrphoresis, Electrophoresis 19 (1998) 3040–3044.

Journal of Pharmaceutical Analysis 8 (2018) 194–201

Contents lists available at ScienceDirect

Journal of Pharmaceutical Analysis

journal homepage: www.elsevier.com/locate/jpa
www.sciencedirect.com

Original Research Article

Physics, chemistry, and Hirshfeld surface analyses of gamma-irradiated thalidomide to evaluate behavior under sterilization doses

Valner A.F.S.N. Mussel [a], Max P. Ferreira [b], Maria B.F. Marques [a], Maria I. Yoshida [a], Mariana R. Almeida [a], Bernardo L. Rodrigues [a], Wagner N. Mussel [a,*]

[a] Departamento de Química, ICEx, Universidade Federal de Minas Gerais - UFMG, Av. Antônio Carlos 6627, 31270-901 Belo Horizonte, MG, Brazil
[b] CNEN-CDTN, Comissão Nacional de Energia Nuclear - Centro de Desenvolvimento da Tecnologia Nuclear, Av. Antônio Carlos, 6627 Belo Horizonte, MG, Brazil

ARTICLE INFO

Article history:
Received 9 June 2017
Received in revised form
24 January 2018
Accepted 25 January 2018
Available online 24 May 2018

Keywords:
Thalidomide
Thermal stability
Polymorphs
Gamma irradiation
Hirshfeld

ABSTRACT

Thalidomide was indicated as a sedative and antiemetic and prescribed for pregnant women. Its tragic teratogenic effects culminated in withdrawal from the market. Since the discovery of its anti-angiogenic and anti-inflammatory actions, thalidomide has been used in the treatment of leprosy and multiple myeloma, which justify studies of its stability. We investigated the effects of irradiation of thalidomide up to 100 kGy (fourfold the usual sterilizing dose for pharmaceutics). The β polymorph of thalidomide was obtained in an isothermal experiment at 270 °C. All samples underwent gamma irradiation for specific times. At different doses, decomposition of the pharmaceutical was not observed up to 100 kGy. The observed effect was angle turning between the phthalimide and glutarimide rings modulated by repulsion towards the carbonyl group, leading to a stable energetic configuration, as measured by the equilibrium in the torsion angle after irradiation. The thalidomide molecule has a center of symmetry, so a full turn starting from 57.3° will lead to an identical molecule. Further irradiation will start the process again. Samples irradiated at 30 and 100 kGy have more compact unit cells and a lower volume, which leads to an increase in the intermolecular hydrogen interaction within the unit cell, resulting in higher thermal stability for polymorph α.

1. Introduction

To ensure adequate conditions of use, sterility is a crucial attribute to any pharmaceutical material, main component, excipient, or formulation. In general, sterilized materials should have microbial survivor probability of $< 10^{-6}$. This criterion is the basis of the sterility assurance level.

There are several sterilization procedures, and each has advantages and disadvantages [1,2]. There is no suitable procedure for general use. Physical removal of microorganisms by membrane filtration does not require heat. Dry heat or even moist heat promotes microbiological reduction at high temperature, but results in considerable degradation of temperature-sensitive materials or devices. Sterilization using ethylene oxide is highly effective but can leave a toxic residue in porous materials such as implants. Electron-beam radiation can be used to prevent temperature effects and toxic residues in the final material, but is limited by poor penetration in bulky materials.

Gamma irradiation has advantages over other conventional sterilization methods in solids: high penetration, uniform efficacy, low isothermal stability, and absence of toxic residues. The main advantage is that irradiation can be used as the final sterilization procedure in starting materials and final products. In this way, the usual 25kGy dose can ensure sterilized pharmaceutical materials [2,3]. Due to the potential sensitivity of pharmaceuticals, validation procedures with lower doses are usually accepted as long as reliable and adequate reduction of the biologic burden can be ensured. In this way, the risk of undesired effects over pharmaceuticals, formulations, or devices submitted to the sterilization process is minimized [4].

Thalidomide ((RS)-2-(2,6-dioxopiperidin-3-il)-1H-isoindol-1,3 (2H)-dione) was synthesized by Chemie Grünenthal in West Germany in 1954. It was introduced to the West German market in 1956 as an antiemetic for pregnant women. In the 1960s, the teratogenic effects of this drug were recognized. Fetal malformation due to the S-isomer of thalidomide resulted in restricted use of thalidomide and increased surveillance by regulatory agencies [5].

Since then, thalidomide has been recognized as having anti-angiogenic and anti-inflammatory properties. It has been used to treat leprosy and multiple myeloma. Hence, stability studies of thalidomide under radioactive stress aimed at sterilization of the drug are warranted [5].

Peer review under responsibility of Xi'an Jiaotong University.
* Corresponding author.
E-mail address: wdmussel@ufmg.br (W.N. Mussel).

https://doi.org/10.1016/j.jpha.2018.01.005
2095-1779/

2. Materials and methods

A sample of thalidomide from a validated production batch was obtained during the shelf-life of this pharmaceutical. All analyses were conducted within the validity period of the batch.

2.1. Powder X-ray diffraction (PXRD)

PXRD data were collected in an XRD-7000 diffractometer (Shimadzu, Kyoto, Japan) at room temperature under 40 kV, 30 mA, using CuK_α ($\lambda = 1.54056$ Å) equipped with polycapillary focusing optics under parallel geometry coupled with a graphite monochromator. The sample was spun at 60 rpm, and scanned over an angular range of 4–60° (2θ) with a step size of 0.01° (2θ) and a time constant of 2s/step. All fitting procedures were obtained using FullProf Suite [6,7]. Crystalexplorer v 17 was used to calculate the Hirshfeld surface [8].

2.2. Single-crystal X-ray diffraction (SCXRD)

SCXRD data were collected in a Gemini A Ultra X-ray Diffraction system (Agilent Technologies, Santa Clara, CA, USA) at room temperature using a MoK_α ($\lambda = 0.71073$ Å) tube as the X-ray source, equipped with a graphite monochromator and a charge-coupled device plate detector. Data collection and refinement details are given in Table 1.

2.3. Thermogravimetric analysis (TGA) and differential thermal analysis (DTA)

TGA and DTA experiments were carried out on a DTG60H system (Shimadzu) in a dynamic N_2 atmosphere (50 mL/min) using alumina pans containing ≈2.0 mg of sample. Experiments were conducted at a heating rate of 10 °C/min from 25 °C to 400 °C.

2.4. Differential scanning calorimetry (DSC)

DSC experiments were undertaken on a DSC60 system (Shimadzu). The equipment cell was calibrated with indium (melting point, 156.6 °C; heat of fusion, $\Delta H_{fus} = 28.54$ J/g) and lead (melting point, 327.5 °C). Aluminum pans containing ≈1 mg of sample were used under a dynamic N_2 atmosphere (50 mL/min) and a heating rate of 10 °C/min from 25 °C to 300 °C. Thalidomide can exist as two polymorphs, α and β, and the latter shows different thermal behavior. Therefore, an isothermal experiment was carried out at 270 °C to obtain a pure material for comparison, as needed.

Table 1
Single crystal refinement data for polymorph α, space group, Hall symbol, lattice parameters *a*, *b* and *c* (Å), ß angle (θ), volume, number of formulae unit per unit cell, X-ray density, wavelength, experimental angular range (θ), crystal absorption coefficient, crystal shape and dimensions, number of reflections considered for cell parameters calculation, and independent reflections used for single crystal fitting.

Crystal data	Values
$C_{13}H_{10}N_2O_4$	Thalidomide
Space group	Monoclinic *P*21/*n*
Hall symbol	-P 2yn
a ± σ (Å)	8.2440 ± 0.0007
b ± σ (Å)	10.0899 ± 0.0009
c ± σ (Å)	14.8991 ± 0.0001
β ± σ (degrees)	102.636 ± 0.008
Volume ($Å^3$)	1209.31 ± 0.02
Z	4
X-ray density (Dx)	1.418 mg/m^3
Wavelength (Mo/Kα)	0.71073 Å
Experimental angular range (θ)	3.2–26.8°
Crystal absorption coefficient (μ)	0.11 mm^{-1}
Crystal shape and dimensions	Prism, 0.24 mm × 0.24 mm × 0.80 mm
Number of reflections considered for cell parameters calculation	1449
Independent reflections used for single crystal fitting	2884

2.5. Ultraviolet spectroscopy

Ultraviolet spectroscopy was undertaken at 200–400 nm for thalidomide at 10 μg/mL in ethanol on a spectrophotometer (1800; Shimadzu). Origin v9.1 was used to adjust data.

2.6. Raman spectroscopy

Raman spectroscopy of solid thalidomide was done on a confocal micro-Raman spectrometer (Senterra; Bruker, Billerica, MA, USA) with an excitation laser set at 785 nm. The measurement conditions were as follows: integration time of 5 s; spectral resolution of 3–5 cm^{-1}; and spectral range of 2000–100 cm^{-1}. The laser was focused with a 4× dry objective lens, with the laser power set to 25 mW. Origin v9.1 was used to adjust data.

2.7. Gamma irradiation

Experiments involving gamma irradiation were done at Comissão Nacional de Energia Nuclear-Centro de Desenvolvimento da Tecnologia Nuclear (Belo Horizonte, MG, Brasil). The radiation system (IR-214; MDS Nordion, Ottawa, Canada) was equipped with a dry cobalt-60 source. The source had a maximum activity of 2200 TBq (60,000 Ci). The specific irradiation times were calculated, and then all samples were exposed to doses of 2, 5, 10, 15, 25, 30 or 100 kGy.

2.8. Attenuated total reflection Fourier transformed infrared spectroscopy (ATR-FTIR)

FTIR analysis was performed at room temperature on a Spectrum 1000 spectrophotometer (PerkinElmer, United States) equipped with an attenuated total reflectance (ATR) accessory. The sample was pressed into a zinc selenide crystal, and 32 scans were averaged. For single FTIR without ATR, the samples were measured in KBr pressed pellets in the wavenumber range between 400 and 3400 cm^{-1} at room temperature, with a resolution of 4 cm^{-1}.

2.9. Statistical analyses

Data are the mean ± standard deviation. All fitting procedures took into account three independent measurements with statistical analyses conducted using Origin v9.1.

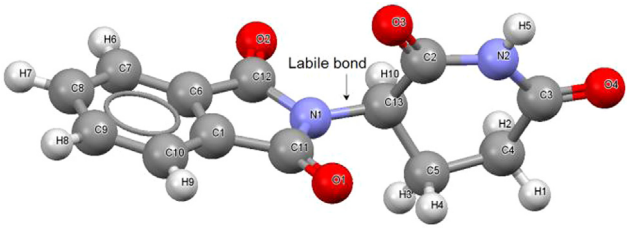

Fig. 1. Thalidomide molecule showing the labile bond between phthalimide and glutarimide rings.

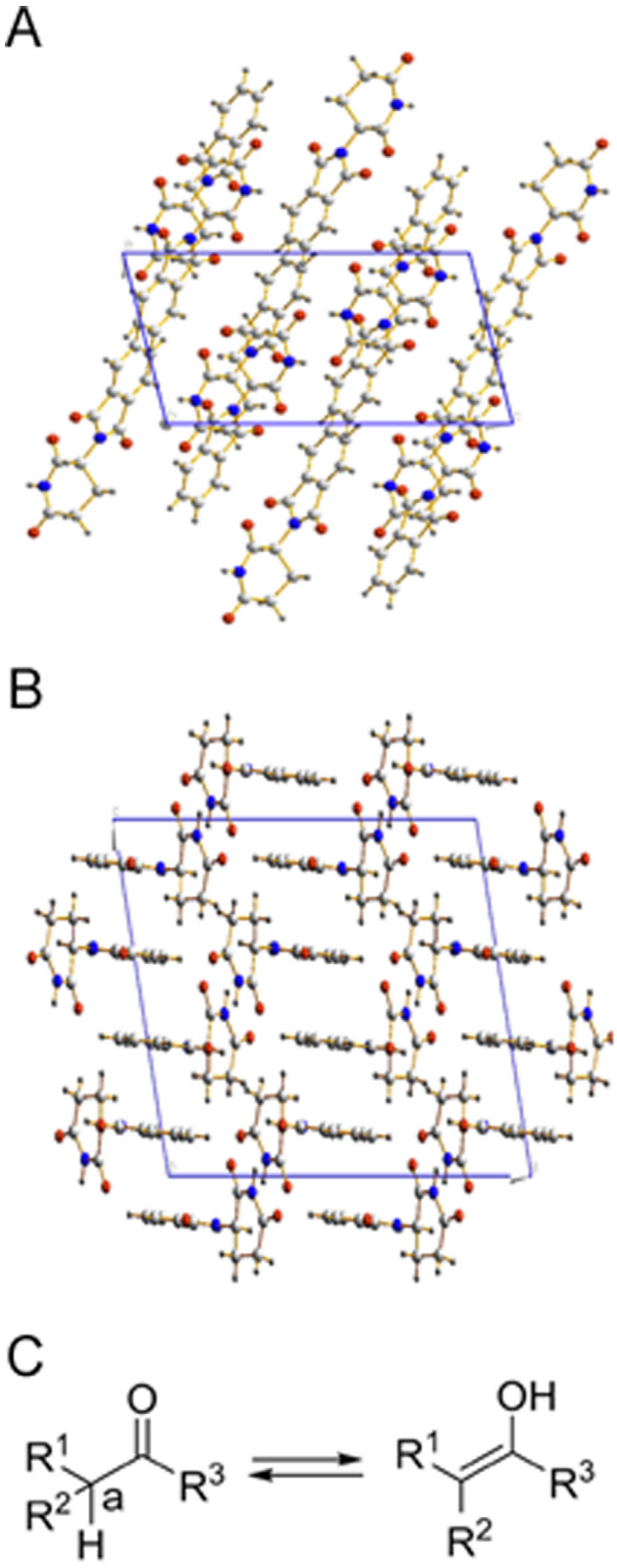

Fig. 2. The crystal structure of the polymorphs α (A) (a = 8.233(1) Å, b = 10.070(2) Å, c = 14.865(2) Å, α = γ = 90.0° and β = 102.53(2)°, monoclinic, P 21/n, Z = 4) and β (B) (a = 20.679(5) Å, b = 8.042(2) Å, c = 14.162(5) Å, α = γ = 90.0° and β = 102.86(3)°, monoclinic, C 2/c, Z = 8), and (C) keto-enol tautomerization.

3. Results and discussion

The thalidomide molecule has a labile bond that can be turned around from phthalimide and glutarimide rings (Fig. 1).

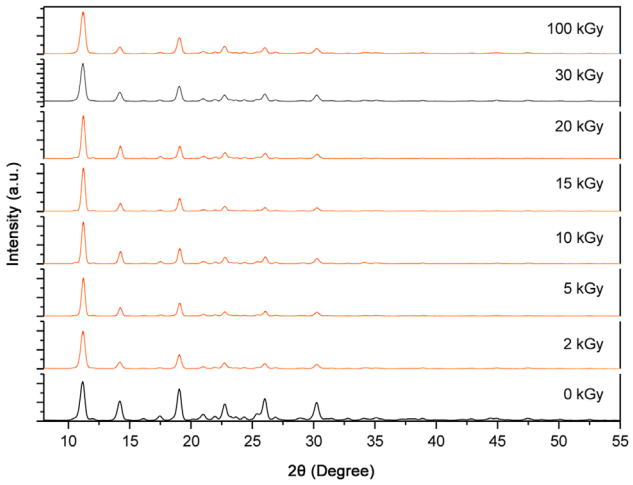

Fig. 3. Powder X-ray diffraction experiments for irradiated thalidomide samples for 0, 2, 5, 10, 15, 20, 30 and 100 kGy. All samples were irradiated under the same conditions, only different times.

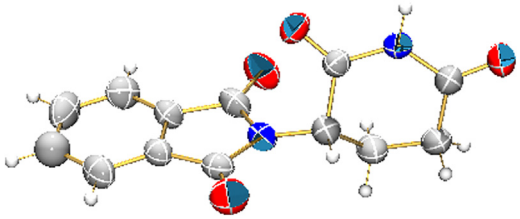

Fig. 4. Crystal projection of the asymmetric unit. Carbon (grey), oxygen (red) and nitrogen (blue) atoms. ORTEP plotted ellipsoids with 50% probability.

In the thalidomide chemical structure, the chiral center has a neighboring ketone that may undergo to the enol form, then re-forming it when switching back to the keto form. Even with uptaking of the correct R-thalidomide, a keto-enol tautomerization happened inside the human body, it would racemase into a mixture of R,S-thalidomide and the corresponding enol forms. The S-thalidomide causes the birth defects (Fig. 2).

The intensity of a diffracted peak of a certain reflection (*hkl*) plane for a given chemical structure is a direct contribution of the structural factor, which in turn corresponds to the number of electrons diffracting the X-ray beam on that plane. If any plane in the structure reduces its number of electrons, a direct effect of that condition will be a decrease in the intensity of that specific plane, and the resulting system will be a plane with lower electron density. In the solid state, the atoms in a structure are much less labile than in solubilized material because of numerous mutual interactions (e.g., Van der Waals forces and/or hydrogen bonding). The fitting procedure was designed to allow the torsion angle between phthalimide and glutarimide rings to vary freely within the extraction and adjustment of the intensities in the diffraction.

The thalidomide structure $C_{13}H_{10}N_2O_4$ space group $P21/n$ has a torsion angle of 57.28° (2θ). This structure was taken as a reference, with all procedures starting from the same template molecule, by varying the fitting sequence as follows: (i) parameterization of the background with five polynomial terms; (ii) U, V and W (FWHM) of the pseudo-Voight function; (iii) profile parameters NA and NB of the pseudo-Voight function; (iv) asymmetry factors P1, P2, P3 and P4 of the Berar–Baldinozzi asymmetric correction; (v) a and b beyond the beta angle of the crystal lattice; (vi) torsion angles N1-C11-C13-C2 with the initial

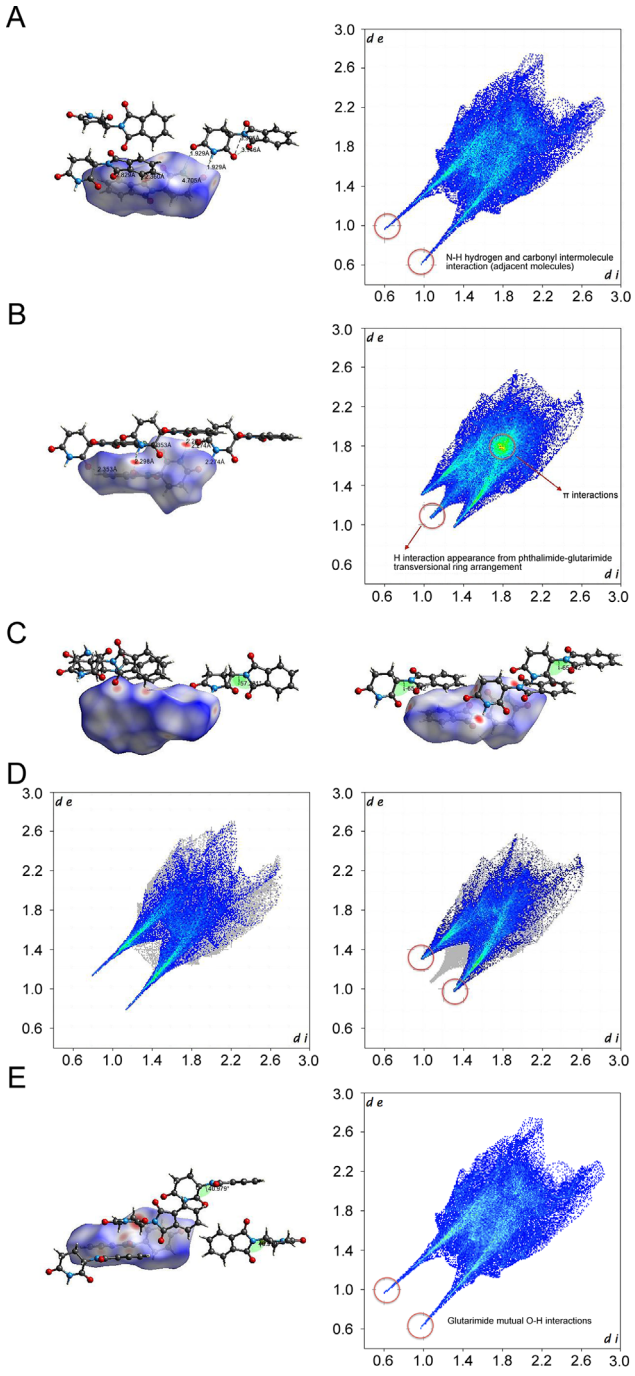

Fig. 5. Hirshfeld surface analysis and corresponding overall fingerprints for polymorphs α and β (A and B, respectively), the torsion angles (C), the fingerprint O-O interactions (π- π respectively) (D). The 2 kGy irradiated α polymorph with respectively torsion angle and overall fingerprint (E).

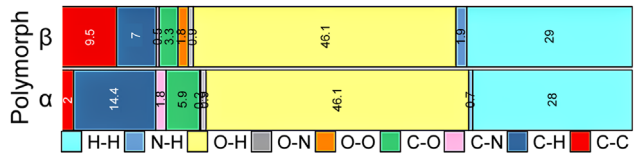

Fig. 6. Hirshfeld surface analysis and overall contributions for all atoms pairs in polymorphs α and β.

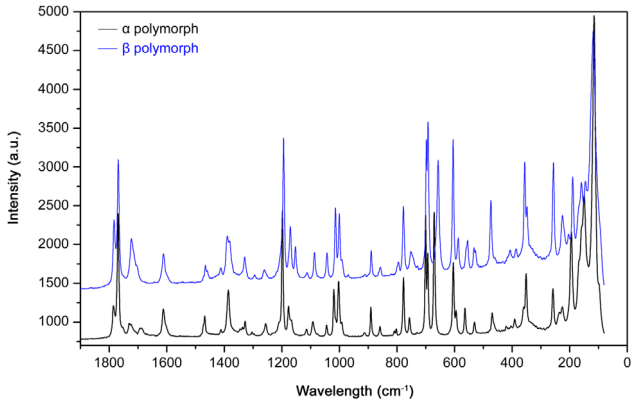

Fig. 7. Raman experimental spectra of polymorphs α and β evidencing the spectra differences.

value set to 57.28° (2θ); (vii) isotropic thermal parameter functions for all atoms. Fig. 3 shows the experimental XRD pattern for all doses.

SCXRD was carried out on a recrystallized sample from an original polymorph α sample by solvent evaporation. To 20 mL of a methanol: water (5:3) solution was added 25 mg of polymorph α, which resulted in a supersaturated solution. Non-solubilized crystals were filtered out, and the solution was allowed to stand to recrystallize over 23 days. The crystal data, collection, and details of structure refinement of polymorph α are summarized in Table 1. Refinement was carried out in the absence of anomalous scattering. Changes in illuminated volume were kept to a minimum, and were taken into account [9–14] using multi-scan inter-frame scaling. Hydrogen atoms were geometrically fixed to their bonded atoms, with their thermal isotropic term, $U_{iso}(H)$ in the range 1.2–1.5 times U_{eq} of the parent atom, after which the positions were refined with adequate constraints. Fig. 4 shows the asymmetric unit as an Ortep plot for the determination of crystal structure, as well as the unit cell ellipsoids with 50% probability.

Hirschfeld surface analyses can provide a deep understanding of certain characteristics based on electron distribution, π interactions, and the contributions of pairs of atoms. Polymorphs α and β showed substantial differences for each fingerprint (Figs. 5A and B). Polymorph β showed a relatively large π interaction on the phthalimide ring. This was a direct evaluation of close contact and the internal distribution of the β cell lattice (Fig. 5B). A large

Table 2
Torsion angle (degrees θ), lattice parameters (Å), β (degrees θ) and Rp goodness of fitting parameter (%).

Dose (kGy)	Torsion angle (degrees θ)	$a \pm \sigma$ (Å)	$b \pm \sigma$ (Å)	$c \pm \sigma$ (Å)	β ± σ (degrees θ)	Rp (%)
0	57.3 ± 0.1	8.233 ± 0.001	10.070 ± 0.002	14.865 ± 0.002	102.53 ± 0.02	*
2	40.1 ± 0.2	8.154 ± 0.004	9.950 ± 0.004	14.714 ± 0.005	102.68 ± 0.02	0.1215
5	41.0 ± 0.1	8.168 ± 0.002	9.976 ± 0.003	14.769 ± 0.004	102.79 ± 0.02	0.1351
10	47.4 ± 0.1	8.251 ± 0.002	10.063 ± 0.002	14.892 ± 0.003	102.86 ± 0.02	0.1020
15	45.0 ± 0.2	8.171 ± 0.001	9.975 ± 0.002	14.754 ± 0.003	102.82 ± 0.02	0.0919
20	47.0 ± 0.1	8.143 ± 0.003	9.943 ± 0.003	14.708 ± 0.004	102.68 ± 0.02	0.1048
30	44.4 ± 0.5	8.204 ± 0.004	9.957 ± 0.004	14.825 ± 0.006	102.79 ± 0.03	0.1400
100	40.2 ± 0.1	8.146 ± 0.004	9.944 ± 0.004	14.717 ± 0.005	102.70 ± 0.02	0.1380

Table 3
Experimental and calculated Raman's observed peak, fully assigned for α polymorph.

Experimental (cm^{-1})	Calculated (cm^{-1})	Observed structure assignments
1785	1896	Symmetrical stretching C═O
1769	1882	Symmetrical stretching C═O
1754	1854	Symmetrical stretching C═O
	1839	Asymmetric stretching C═O
1730	1722	Ring stretch
1688	1686	Ring stretch
	1496	Symmetrical deformation CH_2
	1493	Ring stretch C-C
1468	1466	Ring symmetrical stretching C-N-C
	1449	Ring symmetrical stretching C-N-C
	1424	Ring symmetrical stretching C-N-C, CH
1412	1417	Ring symmetrical stretching C-N-C, C-H
1386	1402	Ring deformation, asymmetrical stretching C-N-C, C-H
1327	1315	Asymmetrical stretching C-N-C, deformation C-H
1256	1235	Ring strain C-N
1210	1214	Strain C-C
1198	1193	Ring deformation, stretching C-C═O
1176	1178	Ring deformation, stretching CH_2-CH_2-CH
1166	1167	Ring deformation, stretching CH_2-CH_2-CH
	1155	Asymmetric stretching CH_2
1114	1127	Ring stretching CH, CH_2
1092	1070	Asymmetric deformation CH_2 stretching CH_2-C═O
1045	1040	Ring stretching, C-N-R_2
1019	1010	Ring stretching, asymmetric stretching CH
1003	986	Ring stretching, symmetric stretching CH
	955	Symmetric deformation CH_2, CH_2-C═O
	935	Ring asymmetric stretching CH
913	911	Deformation CH_2, CH
891	919	Ring symmetric stretching CH
859	848	Ring deformation, ring symmetric stretching CH
809	804	Ring deformation, ring asymmetric stretching CH
802	799	Asymmetric ring deformation
	756	Symmetric stretching C-N-C
757	729	Ring stretching, asymmetric stretching CH_2
701	697	Out of plane ring deformation
693	694	Ring deformation CH, CH_2
671	670	Ring symmetric stretching CH
	665	Ring deformation CH, CH_2
604	641	Ring deformation, stretching CH, CH_2
595	585	Ring deformation CH, CH_2
564	551	Ring symmetric stretching CH, ring deformation
	541	Ring out of plane deformation
531	529	Ring out of plane deformation
	506	Ring stretching CH, CH_2
	495	Ring asymmetric deformation CH
469	472	Deformation C-C═O
404	408	Out of plane deformation C-N-C, deformation CH_2
391	365	Out of plane deformation C-N-C
360	359	Deformation CH_2
351	344	Asymmetric deformation C═O, CH_2
258	262	Asymmetric deformation CH_2
236	243	Out of plane ring deformation
225	240	Out of plane ring deformation
	222	Ring deformation
194	205	Asymmetric deformation CH_2

distance of approximately 1.1 Å from the inside surface (*di*) interaction on polymorph β was related to the appearance of hydrogen-atom interaction from the phthalimide–glutarimide transversional ring arrangement within the unit cell (Figs. 5B and C). The two

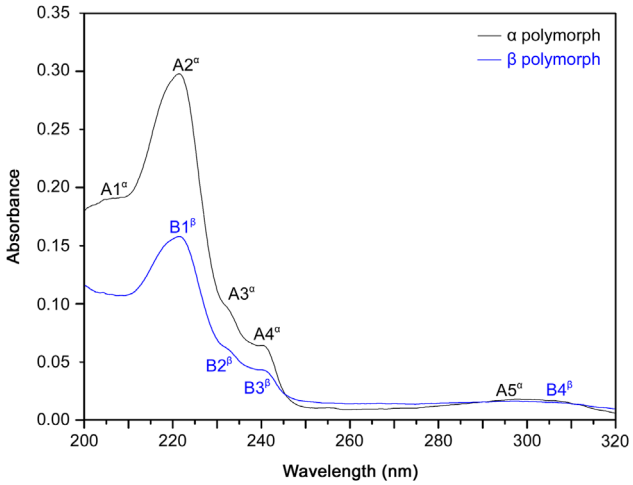

Fig. 8. UV experimental spectra for α and β polymorphs.

interactions at about 1.0 and 1.3 Å (Fig. 5B) from the inside surface (*di*) were due to the glutarimide–glutarimide nitrogen-hydrogen and carbonyl group of two close molecules within the unit cell. The overall O-H interactions showed shorter distances from the inside surface (*di*) of about 1.0 and 1.3 Å for α and β, respectively, and showed a more compact unit cell for polymorph β (Fig. 5D). For polymorph α irradiated at 2 kGy, the two adjacent glutarimide rings within the unit cell were responsible for the mutual O-H interactions leading to hydrogen-bond formation and/or the possibility of a tautomeric pair structure (Fig. 5E). Fig. 6 shows the individual contribution from each atom pair to the overall probability of interaction over the thalidomide molecule [15–17].

Raman spectroscopy was undertaken for both polymorphic forms of thalidomide. Theoretical calculations were carried out to increase understanding of the observed vibrational modes. Theoretical calculations were done using the structures of each polymorph published by the Cambridge Crystallographic Data Center (Cambridge, UK) using Spartan v14. Fig. 7 shows the experimental Raman spectra for polymorphs α and β.

Table 2 shows the experimental and theoretical bands (as assigned) for each mode of polymorph α. For symmetric stretching of the carbonyl group, centered at 1785 and 1769 cm^{-1}, no equivalent vibrational modes, when compared with polymorph β, were identified.

Asymmetric stretching of the carbonyl group was identified at 1754 cm^{-1}. Vibrational modes appeared at two carbonyl groups for polymorph α whereas, in polymorph β, such modes were related primarily only to one carbonyl group. The stretching region of the CH_2-CH bond in the glutarimide ring showed peaks at 1166 and 1176 cm^{-1}, and showed a substantial difference for the ratio and axial offset for the two polymorphs. Peaks on the spectrum for polymorph α at 701 and 693 cm^{-1} were assigned to the vibrational modes corresponding to ring deformations outside the plane. Peaks at 604 and 595 cm^{-1} were assigned to the ring deformation and stretching of the CH group and CH bonds. For deformation out of the plane, peaks at 404, 391, 236 and 225 cm^{-1} were observed. For crystalline structures in different polymorphs, the vibrational modes in the low vibrational frequency region ($< 200\ cm^{-1}$) are attributed to vibrations of the crystal lattice, and that region can be regarded as a "second fingerprint" of the Raman spectrum for each substance (Table 3) [18,19]. Comparison of these data suggested that differences in the spectra of polymorphs α and β were due to compression of their molecules and the way they were interacting in their crystal lattices; these effects influenced

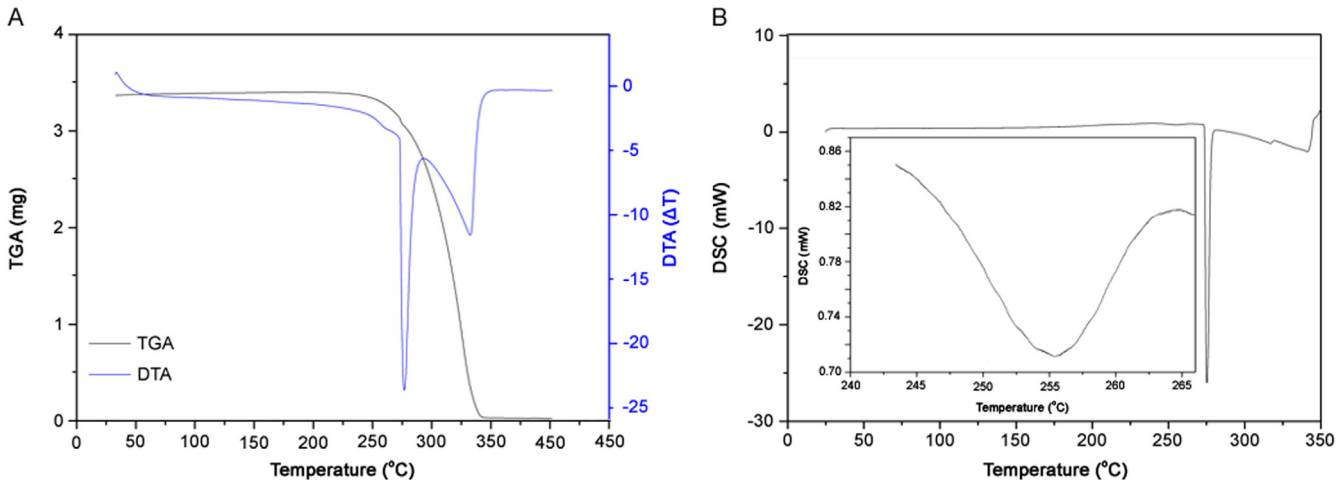

Fig. 9. (A) TGA/DTA simultaneous curve of α polymorph form; (B) DSC curve of α polymorph form, with inset zoom of the endothermic peak.

their vibrational modes directly. Transformation between thalidomide polymorphs was achieved by providing adequate energy for the crystalline lattice with the aim of reorganization. This procedure was accompanied by TGA, DTA and DSC.

In simultaneous TGA/DTA, mass loss was observed only once at an onset temperature of 264 °C, suggesting that the material was anhydrous and pure. The DTA curve revealed two endothermic peaks corresponding to fusion of polymorphs α and β, respectively. The DSC curve showed two endothermic events at onset temperatures of 245 °C and 274 °C. Fig. 8 shows the UV spectra for polymorphs α and β. We observed five bands for polymorph α (A1, A2, A3, A4 and A5) and four bands for polymorph β (B1, B2, B3 and B4). The A1 band at 207 nm is related to the n → π* transitions in aromatic compounds. The A2 and B1 bands at 221 nm and 222 nm, respectively, are related to π* conjugated systems, showing aromatic compounds to have chromophore substitution. The A3 and B2 bands at 232 nm and 233 nm, respectively, are related to tautomers generated by the working pH of the solution. The A4 and B3 bands at 240 nm and 241 nm, respectively, are the characteristic bands of thalidomide. The A5 and B4 bands both at 300 nm are related to groups with a low-energy configuration state, just like the carbonyl groups in thalidomide. For better visualization of the first endothermic peak, enlargement of this region in the curve is shown (Fig. 9). This event was identified as a crystalline transition between the two polymorphs of thalidomide.

The second endothermic event corresponded to decomposition of the formed material, with this being only the β form in the case of total conversion and a mixture of α and β in the case of partial conversion [19]. To confirm these occurrences, an isotherm at 270 °C using the material for further powder XRD was undertaken (Fig. 10). Comparison of the diffractograms and interplanar distances enabled us to confirm and identify the material as polymorph β.

We wished to visualize possible changes in thermal behavior of the material after irradiation. Hence, DSC was done with samples receiving doses of 2, 5, 30 or 100 kGy. In the DSC curve of the samples irradiated with 2 and 5 kGy, a single endothermic peak with an onset temperature of 275 °C was noted for both samples. This finding suggested total conversion of the α form into the β form during heating, so this peak was designated as the fusion follow by decomposition of polymorph β (Fig. 11). The DSC curves of samples irradiated with 30 and 100 kGy revealed two endothermic peaks with onset temperatures of 272 °C and 275 °C for samples irradiated with 30 kGy and at 272 °C and 274 °C for samples irradiated with 100 kGy (Fig. 12).

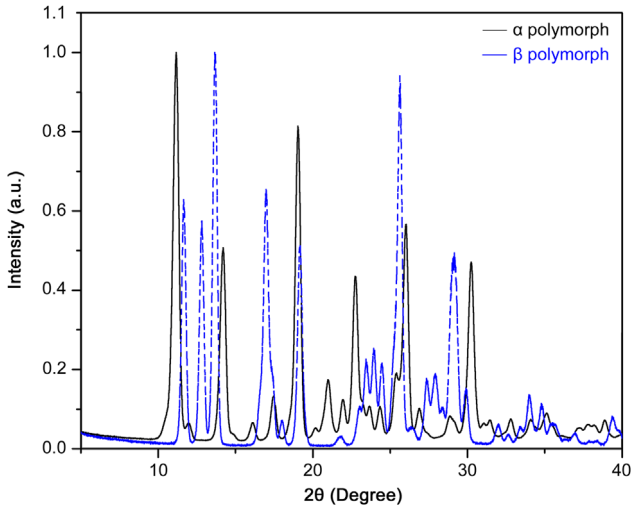

Fig. 10. Comparative diffractogram between α and β polymorphs.

We designated the first peak as the fusion of polymorph α and the second peak as the fusion of polymorph β for both curves. Different from the report by Reepmeyer and colleagues [14], the DSC curve in our study was carried out at a heating rate of 10 °C/min, but we observed values very close to those reported by Reepmeyer and colleagues. We propose that after irradiation with doses of 30 and 100 kGy, polymorph α acquired higher thermal stability in relation to polymorphic transformation. Therefore, the fusion and decomposition temperature of α form was visualized in DSC curves instead of its crystalline transformation, as shown in the physicochemical characterization of the material. The irradiated sample had a more compact unit cell, so there was an increase in hydrogen-atom interactions within the unit cell, resulting in an increase in thermal stability of polymorph α.

4. Conclusion

The observed turning around phthalimide and glutarimide rings already occurs at low radiation values (e.g., 2 kGy). Eventually, the absorbed energy will overcome the repulsive force due to the proximity of the carboxyl group and produce a full turn. With a continuous supply of energy, the system rotates completely at

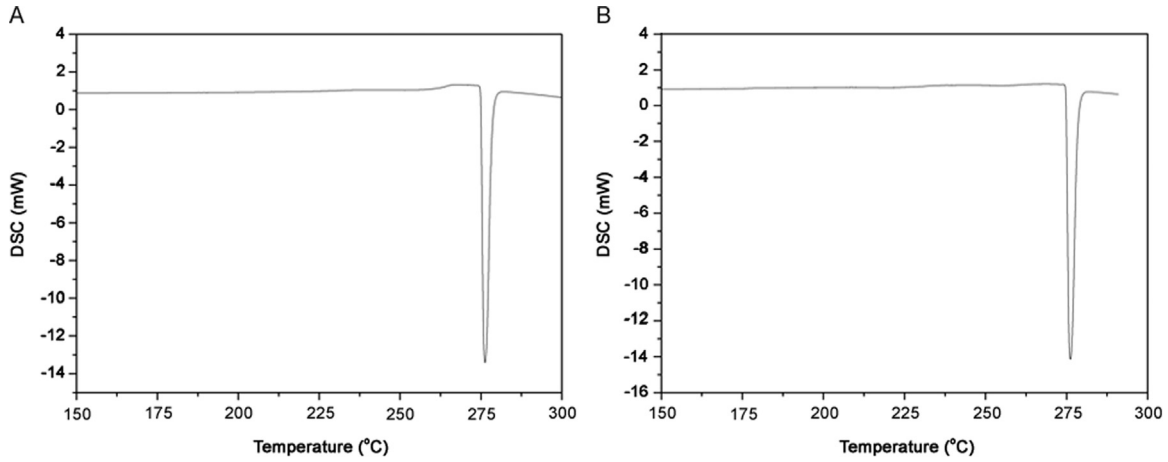

Fig. 11. DSC curves of α polymorph form after (A) 2 kGy dose and (B) 5 kGy dose.

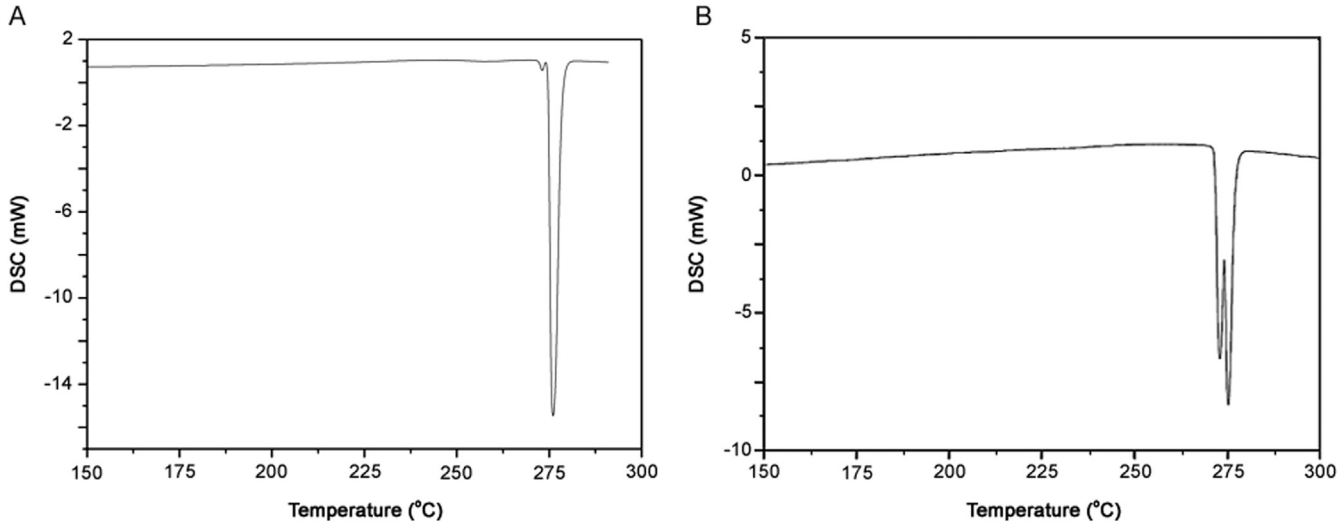

Fig. 12. DSC curves of α polymorph form after (A) 30 kGy dose and (B) 100 kGy dose.

higher doses of 15, 20, 30 and 100 kGy. With higher doses, the full turning effect is reached, allowing the network to relax its tension. The thalidomide molecule has a center of symmetry. Therefore, one full turn of phthalimide and glutarimide rings between each other, starting from 57.3 °, will lead to the same molecule, with stabilization of the final angle based on the total amount of absorbed energy. After a full turn, the process starts again. Irradiated samples at 30 and 100 kGy had more compact unit cells and a lower volume, so there was an increase in the intermolecular interaction between hydrogen atoms within the unit cell, which resulted in higher thermal stability for polymorph α. At 30 and 100 kGy, each melting point could be seen separately, which was a different situation compared with that of the non-irradiated sample. A fourfold increase in the usual dose used in pharmaceuticals is employed for gamma-ray sterilization. Thalidomide molecules can release excess energy by turning the bond between phthalimide and glutarimide rings. Hence, gamma-ray sterilization of pure thalidomide before use in fixed-dose pharmaceutical formulations is possible.

Conflicts of interest

The authors declare that there are no conflicts of interest.

Acknowledgments

The authors would like to thank the CNEN-CDTN (Comissão Nacional de Energia Nuclear – Centro de Desenvolvimento da Tecnologia Nuclear) LIG (Laboratório de Irradiação Gama) facility for the assistance, and Fundação de Amparo à Pesquisa do Estado de Minas Gerais (FAPEMIG) (APQ-02087-14), Conselho Nacional de Desenvolvimento Científico e Tecnológico (CNPq) (245914/2012), Coordenação de Aperfeiçoamento de Pessoal de Nível Superior (CAPES) (PNPD-N-1648694 - scholarship Nº 2016752283) and Pró-Reitoria de Pesquisa/UFMG for financial support.

References

[1] Health Products and Food Branch Inspectorate: Process Validation: Terminal Sterilization Processes for Pharmaceutical Products, Supersedes: GUI-0007, GUI-0009 and GUI-0010, (GUIDE-0074), OTTAWA, Ontario, Canada, 2006.
[2] EN ISO 13408-1:2008(en), Aseptic processing of health care products—Part 1: General requirements, compilation prepared by Online Browsing Platform (OBP), 2008, 〈https://www.iso.org/obp/ui/#iso:std:iso:13408:-1:ed-2:v1:en〉.
[3] AAMI/ISO 11137-2:2013, Sterilization of health care products - Radiation - Part 2: Establishing the sterilization dose (revision of 11137-2: 2012), ISBN(s): 1570205027, 2013.
[4] J. Agalloco, USP Microbiology & Sterility Assurance, Expert Committee USP: Activities Impacting Sterilization & Sterility Assurance, USP 35 1211, revision 2008.

[5] F. Hasanain, K. Guenther, W.M. Mullett, et al., Gamma sterilization of pharmaceuticals - a review of the irradiation of excipients, active pharmaceutical ingredients and final drug product formulations, J. Pharm. Sci. Technol. 68 (2014) 113–137.
[6] T. Roisnel, J. Rodriguez-Carvajal, WinPLOTR: a Windows tool for powder diffraction patterns analysis Materials Science Forum, Proceedings of the Seventh European Powder Diffraction Conference, EPDIC 7, 2000:118–123.
[7] J. Rodriguez-Carvajal, T. Roisnel, FullProf. 98 and WinPLOTR: new windows 95/NT applications for diffraction. Commission for powder, Int. Union Crystallogr. Newsl. 20 (1998) 35.
[8] M.J. Turner, J.J. McKinnon, S.K. Wolff, et al., CrystalExplorer17, University of Western, Australia, 2017 ⟨http://crystalexplorer.scb.uwa.edu.au⟩.
[9] C.H. Görbitz, What is the best crystal size for collection of X-ray data? Refinement of the structure of glycyl-L-serine based on data from a very large crystal, Acta Cryst. B55 (1999) 1090–1098.
[10] R.I. Cooper, A.L. Thompson, D.J. Watkin, CRYSTALS enhancements: dealing with hydrogen atoms in refinement, J. Appl. Cryst. 43 (2010) 1100–1107.
[11] G.M. Sheldrick, A short history of SHELX, Acta Cryst. A64 (2008) 112–122.
[12] P.W. Betteridge, J.R. Carruthers, R.I. Cooper, et al., CRYSTALS Version 12: software for guided crystal structure analysis, J. Appl. Cryst. 36 (2003) 1487.
[13] D.J. Watkin, C.K. Prout, J.R. Carruthers, et al., Crystals Issue 10, Chemical CrystallographyLaboratory, Oxford, UK, 1996.
[14] J.C. Reepmeyer, M.O. Rhodes, D.C. Cox, et al., Characterization and crystal structure of two polymorphic forms of racemic thalidomide, J. Chem. Soc. Perkin Trans. 2 (9) (1994) 2063–2067.
[15] M.A. Spackman, D. Jayatilaka, Hirshfeld surface analysis, CrystEngComm 11 (2009) 19–32.
[16] M.A. Spackman, J.J. McKinnon, Fingerprinting intermolecular interactions in molecular crystals, CrystEngComm 4 (2002) 378–392.
[17] M.J. Turner, J.J. McKinnon, D. Jayatilaka, et al., Visualisation and characterisation of voids in crystalline materials, CrystEngComm 13 (2011) 1804–1813.
[18] P.J. Larking, M. Dabros, B. Sarsfield, et al., Polymorph characterization of active pharmaceutical ingredients (APIs) using low-frequency Raman spectroscopy, Appl. Spectrosc. 68 (7) (2014) 758–776.
[19] E.P.J. Parrot, B.M. Fischer, L.F. Fladden, et al., Terahertz spectroscopy of crystalline and non-crystalline solids, Terahertz spectroscopy and imaging Springer Series in Optical Sciences book series (SSOS), 171, 2012:191–227.

Journal of Pharmaceutical Analysis 8 (2018) 202–207

Contents lists available at ScienceDirect

Journal of Pharmaceutical Analysis

journal homepage: www.elsevier.com/locate/jpa
www.sciencedirect.com

Short Communication

Sensitive and rapid determination of amantadine without derivatization in human plasma by LC–MS/MS for a bioequivalence study

Abhaysingh Bhadoriya [a], Shivprakash Rathnam [a], Bhavesh Dasandi [a], Dharmesh Parmar [a], Mallika Sanyal [b], Pranav S. Shrivastav [c,*]

[a] Bioanalytical Department, Synchron Research Services Pvt. Ltd, 5th Floor, The Chambers, Sarkhej-Gandhinagar Highway, Bodakdev, Ahmedabad 380054, India
[b] Department of Chemistry, St. Xavier's College, Navrangpura, Ahmedabad 380009, India
[c] Department of Chemistry, School of Sciences, Gujarat University, Ahmedabad 380009, India

ARTICLE INFO

Article history:
Received 3 June 2017
Received in revised form
11 September 2017
Accepted 24 October 2017
Available online 21 February 2018

Keywords:
Amantadine
Amantadine-d6
LC–ESI-MS/MS
Sensitive
Bioequivalence study
Human plasma

ABSTRACT

A highly sensitive, rapid and rugged liquid chromatography-tandem mass spectrometry (LC-ESI-MS/MS) method was developed for reliable estimation of amantadine (AMD), an antiviral drug in human plasma. The analyte and internal standard (IS), amantadine-d6 (AMD-d6), were extracted from 200 μL plasma by solid phase extraction on Phenomenex Strata-X-C 33 μ cartridges. Chromatography was performed on Synergi™ Hydro-RP C_{18} (150 mm × 4.6 mm, 4 μm) analytical column using a mixture of acetonitrile and 10 mM ammonium formate, pH 3.0 (80:20, v/v) as the mobile phase. Detection and quantitation was done by multiple reaction monitoring in the positive ionization mode for AMD (*m/z* 152.1 → 135.1) and IS (*m/z* 158.0 → 141.1) on a triple quadrupole mass spectrometer. The assay was linear in the concentration range of 0.50–500 ng/mL with correlation coefficient (r^2) ≥ 0.9969. The limit of detection of the method was 0.18 ng/mL. The intra-batch and inter-batch precisions were ≤ 5.42% and the accuracy varied from 98.47% to 105.72%. The extraction recovery of amantadine was precise and quantitative in the range of 97.89%–100.28%. IS-normalized matrix factors for amantadine varied from 0.981 to 1.012. The stability of AMD in whole blood and plasma was evaluated under different conditions. The developed method was successfully applied for a bioequivalence study with 100 mg of AMD in 32 healthy volunteers. The reproducibility of the assay was determined by reanalysis of 134 subject samples.

1. Introduction

Amantadine (AMD) is an antiviral drug having a tricyclic aliphatic ring system with a primary amino group. It is clinically used in the treatment of influenza A, Parkinsonism, hepatitis C, multiple sclerosis and drug-induced extrapyramidal reactions [1,2]. The exact mechanism of action in the central nervous system is not clearly understood, but evidence suggests that AMD enhances release and reuptake balance of dopamine through antagonism of the N-methyl-D-aspartate receptor [2]. This helps to reduce the symptoms of Parkinsonism [3] and multiple sclerosis [4]. AMD has been extensively used in the poultry industry, particularly in chicken farming due to its antiviral properties for the treatment of influenza [5].

After oral administration, AMD gets rapidly absorbed from the gastrointestinal tract and is excreted unchanged up to 90% of the dose in the urine [6]. A sizeable amount of AMD is bound to red blood cells and about 67% to plasma proteins. The peak plasma concentration of AMD reaches in 1–4 h after ingestion. It has a large apparent volume of distribution (about 5–10 L/kg), signifying extensive tissue binding. AMD is metabolized to a small extent, mainly by N-acetylation, and has an elimination half-life of about 15 h [7].

Literature of the last two decades reveals several analytical methods for the determination of AMD in animal tissues [8–14], biological fluids like plasma [15–23] and urine [22,23] and also in processed food samples [14]. These methods have utilized different analytical techniques like spectrophotometry [19], capillary electrophoresis [15], immunochromatography [13], micellar electrokinetic chromatography [21], ion mobility spectrometry [22], gas chromatography with flame ionization detector [23], high performance liquid chromatography (HPLC) with ultraviolet [18] and fluorescence detection [16], liquid chromatography-tandem

Peer review under responsibility of Xi'an Jiaotong University.
* Correspondence author.
E-mail address: pranav_shrivastav@yahoo.com (P.S. Shrivastav).

https://doi.org/10.1016/j.jpha.2017.10.003

Table 1
Comparative assessment of chromatographic methods developed for analysis of amantadine in plasma and urine (1997–2017).

Sr. no.	Detection technique	Extraction procedure	Sample volume	Linear range (ng/mL)	Retention time; run time	Application	Ref.
1[a]	HPLC-fluorescence	LLE under alkaline conditions followed by derivatization	50 μL rat plasma	40–2000	12.6 min; 24.0 min	Pharmacokinetic studies of amantadine in 8 Wistar rats	[16]
2	LC–MS	LLE under alkaline conditions	200 μL human plasma	3.9–1000	1.9 min; 4.0 min	Bioequivalence study with 100 mg amantadine in 20 healthy volunteers	[17]
3[b]	HPLC–UV	LLE under alkaline conditions followed by derivatization	200 μL rat plasma	50–5000	12.5 min; 30 min	Pharmacokinetic studies of amantadine in 6 Sprague-Dawley male rats	[18]
4[c]	LC–MS/MS	PP with methanol	200 μL human plasma	20–2000	3.2 min; 7.0 min	Pharmacokinetic studies of amantadine in 8 healthy volunteers	[20]
5	GC-FID	Derivatization followed by DLLME	1000 μL human plasma and urine	14–5000 in plasma and 8.7–5000 in urine	19.6 min; 22.0 min	Pharmacokinetic studies with 100 mg amantadine in 4 healthy volunteers	[23]
6	LC–MS/MS	SPE under alkaline conditions	200 μL human plasma	0.50–500	1.80 min; 2.50 min	Bioequivalence study with 100 mg oral dose of amantadine in 32 healthy subjects	PM

HPLC: High-performance liquid chromatography-ultraviolet; LC-MS/MS: Liquid chromatography-tandem mass spectrometry; GC-FID: Gas chromatography-flame ionization detection; LLE: Liquid–liquid extraction; PP: Protein precipitation; DLLME: Dispersive liquid-liquid microextraction; SPE: Solid phase extraction; PM: Present method.

[a] Together with rimantadine.
[b] Together with rimantadine and memantine.
[c] Along with paracetamol, caffeine, chlorpheniramine maleate.

mass spectrometry (LC–MS/MS) [14,17,20], ultra performance liquid chromatography-tandem mass spectrometry (UPLC–MS/MS) [9–12] and ultra high performance liquid chromatography coupled to high resolution LTQ orbitrap mass spectrometry [8]. However, as AMD does not possess any chromophoric group, a majority of these methods require prior derivatization for sample preparation which is tedious, cumbersome and time consuming. Only three methods have analyzed AMD without derivatization in human plasma with a sensitivity of 3.9 ng/mL [17] and 20 ng/mL [20,22] respectively. Moreover, the chromatographic analysis time was $\geq$ 3.5 min in these methods. A detailed summary of chromatographic methods developed for analysis of AMD in plasma samples is given in Table 1. As low concentration of AMD is expected in plasma, it is essential to develop highly sensitive and selective bioanalytical methods especially for pharmacokinetic applications. The developed method is characterized by high sensitivity, selectivity and short analysis time. The method consists of a straightforward solid phase extraction (SPE) procedure without derivatization using 200 μL of plasma samples. The chromatographic turnaround time is only 2.5 min and thus can be useful for routine sample analysis where a large number of samples need to be analyzed in a short time. The method was successfully applied for a bioequivalence study in healthy Indian subjects and the reproducibility in the measurement of subject samples was demonstrated through incurred sample reanalysis (ISR).

2. Experimental

2.1. Chemicals and materials

Reference standards of AMD (purity 99.59%) and AMD-d6 (purity 99.99%) used as internal standard (IS) were obtained from Vivan Life Sciences (P) Ltd. (Mumbai, India). HPLC grade methanol, and analytical reagent grade ammonium formate, formic acid and sodium hydroxide (NaOH) were obtained from Merck Specialties Pvt. Ltd. (Mumbai, India). Strata-X-C 33 μ (30 mg, 1 mL) reversed-phase extraction cartridges were obtained from Phenomenex India (Hyderabad, India). Water used in the entire analysis was prepared using Milli-Q water purification system from Millipore (Bangalore, India). Blank human plasma in K_3EDTA was obtained from Supratech Micropath (Ahmedabad, India) and was stored at −70 °C until use.

2.2. Instruments and conditions

A Shimadzu Nexera X2 UHPLC equipped with Shimadzu LCMS-8040 triple quadrupole mass spectrometer (MS) detector (Shimadzu Corporation, Kyoto, Japan) was used. AMD and AMD-d6 were analyzed on Phenomenex Synergi™ Hydro-RP C_{18} (150 mm × 4.6 mm, 4 μm) analytical column using an isocratic mobile phase consisting of acetonitrile and 10 mM ammonium formate, pH 3.0 adjusted with 0.1% formic acid (80:20, v/v) and delivered at a flow rate of 0.8 mL/min. The column oven temperature and autosampler temperature were maintained at 40 °C and 5 °C, respectively. The injection volume was kept at 10 μL. An electrospray ionization (ESI) source operating in the positive ionization mode was used for multiple reaction monitoring (MRM) LC–MS/MS analysis. The MS conditions optimized for quantification of AMD are summarized in Table S1. Data processing was done using Shimadzu Lab Solution software.

2.3. Preparation of stock solutions, calibration standards and quality control samples

A stock solution of AMD (1000 μg/mL) was prepared by dissolving requisite amount in methanol. Working solutions were prepared by diluting the stock solution with methanol. The stock and working solutions were stored at 2–8 °C. Stock solution (100 μg/mL) of AMD-d6 was prepared by dissolving 1.0 mg in 10.0 mL of methanol. Its working solution (100 ng/mL) was prepared by appropriate dilution of the stock solution in methanol. Calibration standards (CSs) and quality control (QC) samples were prepared by spiking blank plasma with working solutions. The concentration of CSs in the range of 0.50–500 ng/mL and QC samples prepared at five levels (0.05, 1.50, 30.0, 200 and 400 ng/mL) are given in Table 2. All the samples prepared in plasma were kept at −70 °C until use.

2.4. Sample extraction procedure

To an aliquot of 200 μL of spiked plasma/subject samples, 50 μL of AMD-d6 working solution was added and vortexed for 10 s. The solutions were made alkaline by adding 100 μL of 0.1 M NaOH and briefly vortexed. Samples were then loaded on Strata-X-C 33 μ extraction cartridges which were conditioned with 1.0 mL methanol, followed by 1.0 mL water. Washing of samples was done

Table 2
Method performance and linearity parameters for amantadine.

Assay performance		Linearity assessment	
System suitability[a]:		Linearity range (ng/mL)	0.50–500
Precision (% CV)	0.25/ 0.64 for retention time/area response	Calibration standards (ng/mL)	0.05, 1.00, 2.00, 4.00, 10.0, 20.0, 50.0, 100, 250 and 500
Accuracy (%)	97.40–102.53	Quality control samples (ng/mL)	0.50, 1.50, 30.0, 200 and 400
System performance:		Weighting factor	$1/x^2$
Signal-to-noise (S/N) ratio	$\geq$ 18	Mean regression line ($y = mx + c$)	$y = (0.0245 \pm 0.0005)\,x + (0.0107 \pm 0.0009)$
Autosampler carryover[b]:		Correlation coefficient (r^2)	$\geq$ 0.9969
Blank plasma area response	$\leq$ 8.419 ($\leq$ 0.15% of LLOQ area response)	Precision (% CV)	0.32–1.53
Method ruggedness[c]:		Accuracy (% change)	96.3–104.9
Precision (% CV)	2.71–7.40		
Accuracy (%)	93.85–104.15		
Dilution integrity[d]:			
Precision (% CV)	0.24–1.12		
Accuracy (%)	97.8–104.6		
LLOQ and LOD (S/N ratio)	0.50 ng/mL ($\geq$ 18) and 0.18 ng/mL ($\geq$ 10)		

[a] Six consecutive injections of aqueous standard mixture of amantadine (400 ng/mL) and amantadine-d6 (100 ng/mL).
[b] Injection sequence: extracted blank plasma → LLOQ sample → extracted blank plasma → ULOQ sample → extracted blank plasma → ULOQ sample → extracted blank plasma.
[c] One QC batch analyzed on two Synergi Hydro-RP 80 Å (150 mm × 4.6 mm, 4 μm) C_{18} columns with different batch numbers, while the second batch analyzed by different analysts.
[d] Blank human plasma spiked with 1/5th and 1/10th dilution of the stock solution prepared at 1000 ng/mL for amantadine.

with 2 × 1.0 mL water, followed by drying of cartridges for 2.0 min by applying nitrogen (1.72×10^5 Pa) at 2.4 L/min flow rate. The elution of AMD and AMD-d6 was done using 500 μL of mobile phase solution into pre-labeled vials, and 10 μL was used for injection in the chromatographic system.

2.5. Validation procedures

The method validation was performed as per the USFDA guidelines [24] and was similar to our previous work [25]. The detailed procedures and their acceptance criteria are summarized in Supplementary material.

2.6. Pharmacokinetic application and method reproducibility

The developed method was used to analyze AMD plasma concentration after oral administration of single dose of a test (100 mg of amantadine hydrochloride capsules from an Indian Pharmaceutical Company) and a reference (100 mg of amantadine hydrochloride capsules from Sandoz Pharmaceuticals Inc., Princeton, NJ, USA) formulation to 32 healthy Indian subjects under fasting. The study was conducted as per International Conference on Harmonization, E6 Good Clinical Practice Guidelines [26]. The experimental details for the study are given in Supplementary material. The pharmacokinetic parameters of AMD were estimated by non-compartmental analysis using WinNonlin® software version 5.3 (Certara, Princeton, NJ 08540, USA). Method reproducibility was ascertained through ISR using 134 subject samples having concentration near the C_{max} and the elimination phase in the pharmacokinetic profile of the drug and its metabolites. According to the acceptance criterion, at least two-thirds of the original and repeat results should be within 20% of each other [27].

3. Results and discussion

3.1. LC–MS/MS method development

Till date there are only two chromatographic methods based on mass spectrometric detection to analyze AMD in human plasma without prior derivatization [17,20]. Feng et al. [20] determined AMD together with some common medications like paracetamol, caffeine and chlorpheniramine maleate using protein precipitation (PP) for a pharmacokinetic study. However, the recovery was very low (~52%) and the sensitivity of the method was 20 ng/mL for AMD. A much improved LC–MS procedure was reported by Wang and co-workers [17] with a linear concentration range of 3.9–4000 ng/mL using liquid-liquid extraction (LLE). The chromatographic analysis time was 4.0 min under isocratic elution, while both the methods used a general internal standard for area ratio measurements. Thus, based on the outcome of these reports we developed a highly sensitive, selective, rapid and robust method using UHPLC–MS/MS instrumentation and SPE for sample processing employing a deuterated IS, which can give a good measure of control for extraction and ionization variability.

As both AMD and AMD-d6 have a primary amino group, mass spectrometry was performed in the positive ionization mode using ESI. Under the optimized mass spectrometric conditions, intense protonated molecular ions $[M+H]^+$ were obtained at *m/z* 152.1 and 158.0 for AMD and AMD-d6, respectively in the full-scan mode (Q1). The product ion spectrum (Q3) provided highest signals at *m/z* 135.1 and 141.1 for AMD and AMD-d6, respectively (Fig. S1). These stable product ions were obtained by the elimination of amino groups from their precursor ions. In the present work, sample cleanup was initiated on two SPE cartridges, namely, Strata-X-C and Oasis HLB, for quantitative and precise extraction recovery with minimal matrix interference. Initial trials with PP using acetonitrile and methanol yielded poor recovery of AMD with considerable matrix interference (42%–59%), while LLE with ethyl acetate, *n*-hexane, methyl *tert*-butyl ether and dichloromethane alone and in combination afforded somewhat higher recovery (~72%) but was inconsistent at lower concentrations (0.05 and 1.50 ng/mL). With SPE under neutral conditions it was difficult to completely retain AMD (p*Ka* 9.0) [10] and AMD-d6 during the washing step on both the cartridges. Although the recovery obtained was precise at all QC levels, there was a loss of about 15%–18%. Thus, the solutions were made alkaline prior to loading, which led to considerable improvement in recovery (>87%). Both the cartridges provided quantitative recovery, but Strata-X-C specifically used for weakly basic compounds (p*Ka* 8–10) gave higher recoveries compared to Oasis HLB, and hence was used in the present work.

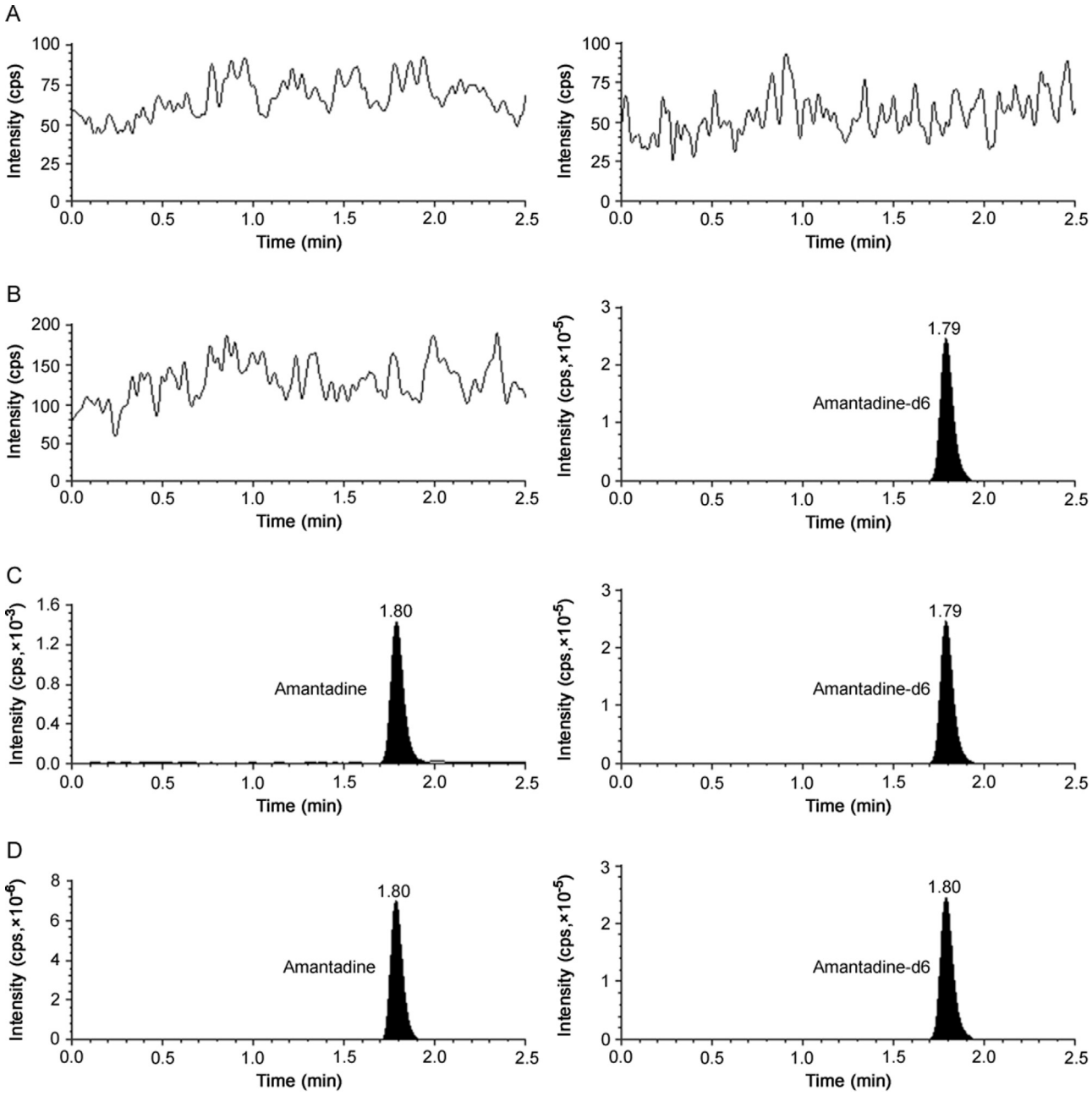

Fig. 1. Representative chromatograms of (A) double blank plasma (without amantadine and amantadine-d6), (B) blank plasma spiked with amantadine-d6 (100 ng/mL), (C) amantadine (0.50 ng/mL) and amantadine-d6 (100 ng/mL) and (D) real subject sample at C_{max} after oral administration of 100 mg dose of amantadine.

Different reversed-phase columns were assessed for a reliable and reproducible analysis of AMD. Columns tested included Kromasil C_{18} (150 mm × 4.6 mm, 3.5 μm), Hypurity C_{18} (100 mm × 4.6 mm, 5 μm), Zorbax Eclipse XDB C_{18} (150 mm × 4.6 mm, 5 μm) and Synergi Hydro-RP C_{18} (150 mm × 4.6 mm, 4 μm). Various mobile phase combinations (50:50, 60:40, 70:30 and 80:20, v/v) of acetonitrile/methanol and 5–20 mM ammonium formate at different pH (2.5–6.5) were tried during development stage. Better results were obtained with lower pH values, which correlated with the capacity factor (*K*). With increase in pH values (4.5–6.5), the *K* values were in the range of 0.4–0.6, possibly due to the formation of unionized species which had little retention. A similar trend was observed when the concentration of ammonium formate was increased from 5.0 to 20 mM. Further the impact of mobile composition showed considerable reduction in analyte response when the aqueous proportion was greater than 30%. Acetonitrile was selected ahead of methanol as it provided much better peak shape. Under the optimized mobile phase conditions of acetonitrile and 10 mM ammonium formate (pH 3.0), AMD was not adequately retained on Kromasil C_{18} and Hypurity C_{18} columns, while the response and peak shape were not acceptable on Zorbax Eclipse XDB C_{18}. As a result, Synergi Hydro-RP C_{18} column which provided adequate retention, sufficient response and good peak shape was employed for further study. Additionally, use of deuterated IS helped to ensure acceptable method performance based on similar extraction recovery, chromatographic retention time and ionization response in ESI-MS/MS. The retention time for AMD and AMD-d6 was 1.80 and 1.79 min, respectively, in a total run time of 2.5 min (Fig. 1). The reinjection reproducibility (% CV) in the measurement of retention time was ≤ 1.2%.

The developed method was more sensitive by about 8 [17] and 40 [20] times compared to existing LC–MS methods in human

Table 3
Extraction recovery and matrix factor for amantadine from human plasma.

Quality control level (ng/mL)	Mean area response (n = 6)			Recovery (%)		Matrix factor		
	A (post-extraction spiking)	B (pre-extraction spiking)	C (neat samples in mobile phase)	Analyte (B/A)	IS	Analyte (B/A)	IS	IS-normalized (Analyte/IS)
400	4490400	4502973	4424039	100.28	98.95	1.015	1.013	1.002
200	2276200	2276427	2334564	100.01	99.68	0.975	0.979	0.995
30.0	334780	327716	340223	97.89	97.75	0.984	1.003	0.981
1.50	16839	16704	16623	99.20	98.63	1.013	1.000	1.012

IS: internal standard.

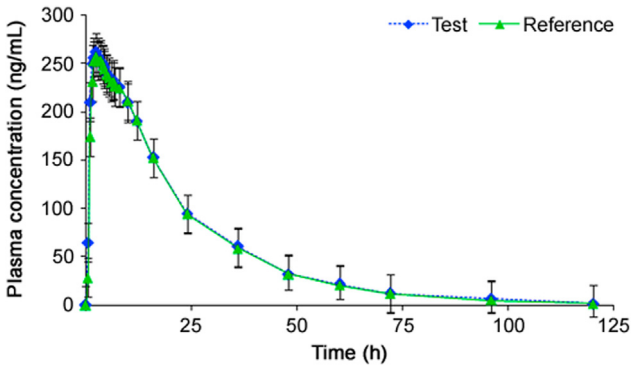

Fig. 2. Mean plasma concentration-time profile of amantadine after oral administration of 100 mg (test and reference) capsule formulation to 32 healthy Indian subjects.

plasma. Moreover, the analysis time was 1.5 times less than the method reported by Wang et al. [17], which can be of advantage when large numbers of samples are to be analyzed, especially in a clinical setting. A comparative assessment of all chromatographic methods developed in the last two decades in plasma and urine is presented in Table 1.

3.2. Assay validation results

The results for system suitability, autosampler and column carryover, ruggedness and dilution integrity suggest acceptable assay performance as evident from the data presented in Table 2. The selectivity of the method is evident from the chromatograms of double blank plasma, plasma spiked with AMD-d6, AMD at 0.50 ng/mL concentration and real subject sample at C_{max} in Fig. 1. No interference due to endogenous components was observed at the retention time of AMD and AMD-d6. Furthermore, none of the commonly used medications by human volunteers interfered at their retention times. The calibration curves showed good linearity over the established concentration range of 0.50–500 ng/mL ($r^2 \geq 0.9969$) for AMD. The mean values for slope, intercept, accuracy and precision data in the measurement of calibrator concentrations are shown in Table 2. The intra-batch precision (% CV) ranged from 0.56% to 5.42% and the accuracy was within 98.47%–105.72% for AMD. Similarly for inter-batch experiments, the precision varied from 1.27% to 4.23% and the accuracy was within 98.86%–105.21% (Table S2).

The mean extraction recovery and IS-normalized matrix factors (MFs) for AMD are presented in Table 3. Highly precise extraction recovery in the range of 97.89%–100.28% was obtained across QC levels. The mean recovery of AMD-d6 was 98.75%. As presence of unmonitored, co-eluting compounds from the matrix can directly impact the overall performance of a validated method, it is necessary to evaluate MFs to assess the matrix effect. The IS-normalized MFs ranged from 0.981 to 1.012. Matrix effect was also checked in lipemic and haemolysed plasma samples together with normal K_3EDTA plasma. This was determined by examining the precision (% CV) values of the slopes of the calibrations curves prepared from eight different plasma lots, which included six K_3EDTA, one lipemic and one haemolysed plasma samples. The % CV of the slopes of calibration lines for relative matrix effect in eight different plasma lots was 1.52%, which is within the acceptance criteria of 3%–4%.

Stock solutions kept for short-term and long-term stability as well as spiked plasma solutions showed no evidence of degradation under all studied conditions. Samples for short-term stability remained stable up to 8 h, while the stock solutions of AMD and AMD-d6 were stable for minimum of 18 days at refrigerated temperature of 5 °C. As a substantial amount of AMD is bound to red blood cells, whole blood stability of AMD was also evaluated by spiking blood samples (500 μL) with AMD at 0.15 and 400 ng/mL concentrations for 2.0 h. The detailed results for stability studies are presented in Table S3.

3.3. Application to a bioequivalence study and ISR results

To the best of our knowledge there have been no reports on the pharmacokinetics of AMD in Indian subjects. Thus, the developed

Table 4
Mean pharmacokinetic (± SD) parameters, comparison of treatment ratios and 90% CIs of natural log (Ln)-transformed parameters following oral administration of 100 mg of amantadine tablet formulation in 32 healthy Indian subjects under fasting.

Parameter	Test	Reference	Ratio (test/ reference, %)	90% CI (Lower–Upper)	Power	Intra subject variation (% CV)
C_{max} (ng/mL)	285.06 ± 32.16	281.58 ± 36.64	101.23	96.14–107.23	0.9997	7.53
AUC $_{0\text{–}12\ h}$ (h · ng/mL)	6372.25 ± 1047.69	6222.41 ± 987.12	102.41	97.48–107.95	0.9998	8.09
AUC $_{0\text{-}inf}$ (h · ng/mL)	6704.26 ± 1216.10	6563.53 ± 1008.22	102.63	97.27–108.42	0.9992	8.33
T_{max} (h)	2.51 ± 0.53	2.73 ± 0.46	–	–	–	–
$t_{1/2}$ (h)	14.21 ± 3.60	14.06 ± 3.56	–	–	–	–
K_{el} (1/h)	0.05 ± 0.01	0.05 ± 0.01	–	–	–	–

SD: standard deviation CI: confidence interval; CV: coefficient of variation; C_{max}: maximum plasma concentration; $AUC_{0\text{–}120\ h}$: area under the plasma concentration-time curve from 0 h to 120 h; $AUC_{0\text{-}inf}$: area under the plasma concentration-time curve from zero hour to infinity; T_{max}: time point of maximum plasma concentration; $t_{1/2}$: half life of drug elimination during the terminal phase; K_{el}: elimination rate constant.

method was applied to determine plasma AMD concentration in 32 healthy Indian subjects after oral administration of 100 mg AMD capsules under fasting. The mean plasma concentration–time profiles obtained for the test and reference formulations are shown in Fig. 2. Table 4 summarizes mean values of pharmacokinetic parameters for both the formulations. Comparison of the results obtained with a similar study using 100 mg dose of AMD in 20 Chinese subjects [17] showed no significant change in T_{max} and $t_{1/2}$ values. However, the C_{max} values obtained in the present study were lower, while AUC values were somewhat higher than their results. Nevertheless, the ratios of mean log-transformed parameters, C_{max}, $AUC_{0-120\ h}$ and $AUC_{0\text{-}inf}$ and their 90% confidence intervals ranged from 101.23% to 102.63% and 96.14% to 108.42% for AMD, respectively, which is within the acceptance criterion of 80%–125%. These results confirm the bioequivalence of the test formulation with the reference product in terms of rate and extent of absorption. Furthermore, the assay reproducibility test performed with 134 incurred samples showed % change within $\pm$ 12% of the initial results, which confirms the reproducibility of the newly developed method.

4. Conclusions

The proposed LC–MS/MS assay for the quantitation of AMD in human plasma was developed and fully validated as per current regulatory guidelines. This method can be useful for the analysis of large numbers of samples as it uses a simple extraction procedure without derivatization, requires low sample volume, is highly selective, and has a short assay time. Further, the method shows excellent accuracy and precision, reproducible recoveries and minimal matrix effects. In addition, the method was successfully applied to determine plasma AMD concentration in a bioequivalence study with healthy Indian subjects for the first time.

Conflicts of interest

The authors declare that there are no conflicts of interest.

Acknowledgments

The authors wish to thank the management of Synchron Research Services Pvt. Ltd, Ahmedabad to carrying out this research.

Appendix A. Supplementary material

Supplementary data associated with this article can be found in the online version at doi:10.1016/j.jpha.2017.10.003.

References

[1] I.T. Prudhomme, O. Zoueva, J.M. Weber, Amantadine susceptibility in influenza A virus isolates: determination methods and lack of resistance in a Canadian sample, 1991–94, Clin. Diagn. Virol. 8 (1997) 41–51.
[2] W. Xu, N. Wei, Y. Xu, et al., Does amantadine induce acute psychosis? A case report and literature review, Neuropsychiatr. Dis. Treat. 12 (2016) 781–783.
[3] J. Romrell, H.H. Fernandez, M.S. Okun, Rationale for current therapies in Parkinson's disease, Expert Opin. Pharmacother. 4 (2003) 1747–1761.
[4] L.B. Krupp, Fatigue in multiple sclerosis: definition, pathophysiology and treatment, CNS Drugs 17 (2003) 225–234.
[5] D. Cyranoski, China's chicken farmers under fire for antiviral abuse, Nature 435 (2005) (1009-1009).
[6] J.M. Meythaler, R.C. Brunner, A. Johnson, et al., Amantadine to improve neurorecovery in traumatic brain injury-associated diffuse axonal injury: a pilot double-blind randomized trial, J. Head Trauma Rehabil. 17 (2002) 300–313.
[7] SYMMETREL® (Amantadine Hydrochloride), Prescribing Information, NOVARTIS Pharm aceuticals Australia Pty Limited, 54 Waterloo Road, North Ryde, NSW, Australia, 2014. ⟨http://www.guildlink.com.au/gc/ws/nv/pi.cfm?product=nvpsymor11014⟩. (Accessed March 2017).
[8] H. Yan, X. Liu, F. Cui, et al., Determination of amantadine and rimantadine in chicken muscle by QuEChERS pretreatment method and UHPLC coupled with LTQ Orbitrap mass spectrometry, J. Chromatogr. B 938 (2013) 8–13.
[9] Y.L. Wu, R.X. Chen, Y. Xue, et al., Simultaneous determination of amantadine, rimantadine and memantine in chicken muscle using multi-walled carbon nanotubes as a reversed-dispersive solid phase extraction sorbent, J. Chromatogr. B 965 (2014) 197–205.
[10] Z.C. Liu, F. Yang, M. Yao, et al., Simultaneous determination of antiviral drugs in chicken tissues by ultra high performance liquid chromatography with tandem mass spectrometry, J. Sep. Sci. 38 (2015) 1784–1793.
[11] P. Mu, N. Xu, T. Chai, et al., Simultaneous determination of 14 antiviral drugs and relevant metabolites in chicken muscle by UPLC–MS/MS after QuEChERS preparation, J. Chromatogr. B 1023–1024 (2016) 17–23.
[12] Q. Zhang, C. Xiao, W. Wang, et al., Chromatography column comparison and rapid pretreatment for the simultaneous analysis of amantadine, rimantadine, acyclovir, ribavirin and moroxydine in chicken muscle by ultra high performance liquid chromatography and tandem mass spectrometry, J. Sep. Sci. 39 (2016) 3998–4010.
[13] S. Wu, F. Zhu, L. Hu, et al., Development of a competitive immunochromatographic assay for the sensitive detection of amantadine in chicken muscle, Food Chem. 232 (2017) 770–776.
[14] Y. Tsuruoka, T. Nakajima, M. Kanda, et al., Simultaneous determination of amantadine, rimantadine, and memantine in processed products, chicken tissues, and eggs by liquid chromatography with tandem mass spectrometry, J. Chromatogr. B 1044 (2017) 142–148.
[15] S. Nagaraj, S.V. Rahavendran, H.T. Karnes, Visible diode laser induced fluorescence detection for capillary electrophoretic analysis of amantadine in human plasma following precolumn derivatization with Cy5.29.OSu[1], J. Pharm. Biomed. Anal. 18 (1998) 411–420.
[16] Y. Higashi, I. Uemori, Y. Fujii, Simultaneous determination of amantadine and rimantadine by HPLC in rat plasma with pre-column derivatization and fluorescence detection for pharmacokinetic studies, Biomed. Chromatogr. 19 (2005) 655–662.
[17] P. Wang, Y.Z. Liang, B.M. Chen, et al., Quantitative determination of amantadine in human plasma by liquid chromatography–mass spectrometry and the application in a bioequivalence study, J. Pharm. Biomed. Anal. 43 (2007) 1519–1525.
[18] C. Shuangjin, F. Fang, L. Han, et al., New method for high-performance liquid chromatographic determination of amantadine and its analogues in rat plasma, J. Pharm. Biomed. Anal. 44 (2007) 1100–1105.
[19] A.M. Mahmoud, N.Y. Khalil, I.A. Darwish, Selective spectrophotometric and spectrofluorometric methods for the determination of amantadine hydrochloride in capsules and plasma via derivatization with 1,2-naphthoquinone-4-sulphonate, Int. J. Anal. Chem. (2009) 1–8 (Article ID 810104).
[20] S. Feng, Y. Tian, Z. Zhang, et al., Rapid simultaneous determination of paracetamol, amantadine hydrochloride, caffeine and chlorpheniramine maleate in human plasma by liquid chromatography/tandem mass spectrometry, Arzneimittelforschung 59 (2009) 86–95.
[21] H.H. Yeh, Y.H. Yang, S.H. Chen, Simultaneous determination of memantine and amantadine in human plasma as fluorescein derivatives by micellar electrokinetic chromatography with laser-induced fluorescence detection and its clinical application, Electrophoresis 31 (2010) 1903–1911.
[22] M. Saraji, T. Khayamian, S. Mirmahdieh, et al., Analysis of amantadine in biological fluids using hollow fiber-based liquid–liquid–liquid microextraction followed by corona discharge ion mobility spectrometry, J. Chromatogr. B 879 (2011) 3065–3070.
[23] M.A. Farajzadeh, N. Nouri, A.A.A. Nabil, Determination of amantadine in biological fluids using simultaneous derivatization and dispersive liquid–liquid microextraction followed by gas chromatography-flame ionization detection, J. Chromatogr. B 940 (2013) 142–149.
[24] Guidance for Industry, Bioanalytical Method Validation, US Department of Health and Human Services, Food and Drug Administration Centre for Drug Evaluation and Research (CDER), Centre for Veterinary Medicine (CVM), May 2001.
[25] P. Sharma, P.A. Shah, M. Sanyal, et al., Challenges in optimizing sample preparation and LC-MS/MS conditions for the analysis of carglumic acid, an N-acetyl glutamate derivative in human plasma, Drug Test. Anal. 7 (2015) 763–772.
[26] Guidance for Industry: ICH E6 Good Clinical Practice, U.S. Department of Health and Human Services, Food and Drug Administration, Centre for Drug Evaluation and Research (CDER), Centre for Biologics Evaluation and Research (CBER), 1996.
[27] M. Yadav, P.S. Shrivastav, Incurred sample reanalysis: a decisive tool in bioanalytical research, Bioanalysis 3 (2011) 1007–1024.